DEVELOPMENT OF LOCALLY AVAILABLE SANDWICH COMPOSITE FOR SUSTAINABLE LIGHTWEIGHT STRUCTURES

By

Areej Thabit Al malkawi

A DISSERTATION

Submitted to
Michigan State University
in partial fulfillment of the requirements
for the degree of

Civil Engineering—Doctor of Philosophy

2020

ABSTRACT

DEVELOPMENT OF LOCALLY AVAILABLE SANDWICH COMPOSITE
FOR SUSTAINABLE LIGHTWEIGHT STRUCTURES

By

Areej Thabit Al malkawi

Aerated slurry-infiltrated chicken mesh was evaluated as a lightweight and structurally resilient material for building construction. Aerated slurry with relatively low structural qualities was shown to perform favorably when used as a matrix with chicken mesh reinforcement in structural applications. The high specific surface area of chicken mesh and the close spacing of its wires (when used at 2-4% volume fraction) effectively enhance the mechanical performance and dimensional stability of the aerated slurry. The chicken mesh structural behavior also benefits significantly from embedment in the aerated slurry, which mitigates the reorientation tendency of the chicken mesh wires under tension. This effect enables mobilization of the tensile load-carrying capacity of the wires in chicken mesh at structurally viable deformations.

A comprehensive experimental program was undertaken at materials and structures levels in order to develop aerated slurry-infiltrated chicken mesh materials and structural systems with a desired balance of strength, ductility and hysteretic energy dissipation capacity. The bulk density of the aerated slurry and the chicken mesh volume fraction were some key variables in the design of the new (composite) building material. With proper selection of these variables, the synergistic actions of the aerated slurry and the chicken mesh in the context of the composite material were confirmed. Empirical models were developed for the mechanical performance of this composite material. In the future, the structural performance of this

composite material may be verified by constructing a full-scale building system and conducting shaking table tests.

To my father Dr. Thabit Malkawi – to whom I promised to dedicate my doctorate journey before he left this world

ACKNOWLEDGEMENTS

Venture this PhD has been a truly life-changing milestone for me and it would not have been possible to go through without the support and guidance that I received from many people.

I would like to express sincere gratitude for Dr. Katy Colbry, I appreciate all her contributions of time, support, and funding to make my Ph.D. experience positive and productive. I gratefully acknowledge the members of my Ph.D. committee Dr. Thomas Voice, Dr. Neeraj Buch, Dr. Thomas Wolff, for their time and valuable feedback on this dissertation.

I greatly appreciate the support received from Office for International Students and Scholars (OISS). I am especially grateful for Brooke Stokdyk , Ismail Adawe for all support in numerous ways during various stages of my PhD.

I would also like to say a heartfelt " I love you" for my daughter Sophia , her existence in my life made me stronger, better and more fulfilled than I could have ever expected.

TABLE OF CONTENTS

LIST OF TABLES

LIST OF FIGURES

CHAPTER 1: INTRODUCTION

1.1 General

The goal of this research is to develop building structural materials and systems that can make effective use of locally available materials and construction resources. Aerated concrete with bulk densities less than 1 g/cm^3 is generally viewed as a non-structural material that offers thermal insulation qualities. The research described here found that a reinforcement system with high specific surface area, close spacing, and desired mechanical bonding with matrix would enable use of aerated concrete in structural applications. Chicken mesh (poultry netting) was used in this investigation as a commonly available reinforcement that meets the requirements for transforming aerated concrete into a structural material. Viable volume (and area) fractions of chicken mesh for structural applications produce a high degree of congestion with the formwork. Therefore, an aerated slurry of high flowability was used to thoroughly infiltrate the congested reinforcement system, facilitating thorough consolidation and desired interfacial interactions. The mesh behaves as a homogeneous reinforcement to produce lightweight cementitious composites with a desired balance of strength-to-weight ratio, ductility and toughness (Wafa and Fukuzawa 2010). Ferrocement, a cementitious mortar with wire mesh reinforcement, provided the inspiration for development of aerated slurry-infiltrated chicken mesh (Naaman 2000).

1.2 Summary of Research

This thesis is divided into nine chapters, with Chapters 2 through 8 each containing a stand-alone paper previously published in peer-reviewed, reputable, high-impact-factor journals. Chapter 9 summarizes highlights of this work and briefly discusses potential applications. For convenience, the references have been consolidated at the end of each chapter. The abstracts for each of these papers are included below to summarize the work described in each chapter.

1.2.1 Physio-Microstructural Properties of Aerated Cement Slurry for Lightweight Structures

"Cementitious composites, including ferrocement and continuous fiber reinforced cement, are increasingly considered for building construction and repair. One alternative in processing of these composites is to infiltrate the reinforcement (continuous fibers or chicken mesh) with a flowable cementitious slurry. The relatively high density of cementitious binders, when compared with polymeric binders, are a setback in efforts to introduce cementitious composites as lower-cost, fire-resistant, and durable alternatives to polymer composites. Aeration of the slurry is an effective means of reducing the density of cementitious composites. This approach, however, compromises the mechanical properties of cementitious binders. An experimental program was undertaken in order to assess the potential for production of aerated slurry with a desired balance of density, mechanical performance, and barrier qualities. The potential for nondestructive monitoring of strength development in aerated cementitious slurry was also investigated. This research produced aerated slurries with densities as low as 0.9 g/cm^3 with viable mechanical and barrier qualities for production of composites. The microstructure of these composites was also investigated" Almalkawi, Salem et al. (2018).

1.2.2 Mechanical Properties of Aerated Slurry-Infiltrated Chicken Mesh

"Aerated slurry-infiltrated chicken mesh was evaluated as a ductile and lightweight material for building construction. The compressive strength of the aerated slurry, and the tensile, compressive and flexural behavior of the aerated slurry-infiltrated chicken mesh were evaluated. Aerated slurry provided a relatively low compressive strength, which did not suit load-bearing applications. Aerated slurry infiltrated chicken mesh, on the other hand, provided desired mechanical properties, including significantly improved compressive strength, for load-bearing applications. The system exhibited a ductile failure mode which can be attributed to the high specific surface area and the desired mechanical interlocking of the chicken mesh reinforcement. The effects of aeration on the system behavior were evaluated. A theoretical model was developed for evaluating the mechanical behavior of aerated slurry infiltrated chicken mesh. Aerated slurry-infiltrated chicken mesh offers a desired combination of light weight and mechanical characteristics for use as a building construction material" (Almalkawi, Hong et al. 2018).

1.2.3 Behavior of a Lightweight Frame Made with Aerated Slurry-Infiltrated Chicken Mesh Under Cyclic Lateral Loading

"Aerated slurry-infiltrated chicken mesh is a ductile and light-weight material for seismic-resistant building construction. An aerated slurry-infiltrated chicken mesh frame was subjected to cyclic lateral loading in order to assess its load-bearing capacity, ductility and hysteretic energy dissipation capacity. The frame exhibited a ductile failure mode compatible with its strong column-weak beam design. It also exhibited a desirable hysteretic energy dissipation capacity. Comparisons were made between the performance characteristics of this frame versus those of

structural systems of similar geometric attributes made primarily of wood-based sheets. Semi-empirical models were developed for prediction of the structural behavior of aerated slurry-infiltrated chicken mesh. The structural performance of the frame made with aerated slurry-infiltrated chicken mesh under cyclic lateral loads was compared against those of lateral load-resisting systems of comparable geometric attributes comprising primarily of OSB and hardwood sheets" (Almalkawi, Hong et al. 2018).

1.2.4 Evaluation of the Energy-Efficiency of an Aerated Slurry-Infiltrated Mesh Building System with Biomass-Based Insulation

"Experimental investigations and numerical analyses were conducted on the thermal attributes of a building system made with locally available structural and insulation materials. The structural material, which also offers some insulation qualities, is referred to as aerated slurry-infiltrated mesh. The insulation materials used in this building are based on biomass; the alternatives considered here include ground wood, shredded straw, and cellulose. Thermal conductivity tests were performed on aerated slurries of different bulk densities, and on the biomass-based insulation materials, some of which were prepared with different bulk densities. The competitive merits of the biomass-based indigenous insulation materials were assessed. The correlations between bulk density and thermal conductivity were evaluated and rationalized based on the prevalent mechanisms of heat transfer in different materials. The effects of temperature on the thermal conductivity of different biomass-based indigenous insulation materials were investigated. For wall insulation, a cost analysis was conducted in order to select the optimum insulation level. The thermal mass of the aerated slurry-infiltrated mesh building

system was found to favor its energy-efficiency when compared with a similar wood building" (Almalkawi, Soroushian et al. 2019).

1.2.5 Aerated Cement Slurry and Controlling Fungal Growth of Low-Cost Biomass-Based Insulation Materials

"Biomass ash-based insulation in the form of wood chips or ground wood offers desired thermal insulation qualities complemented with low cost, ready availability, and favorable ecological features. There are, however, concerns with the resistance to fire, moisture and fungus growth of such insulation. The work reported herein focuses on improvement of the resistance to fungus growth of low-cost biomass-based insulation comprising largely of wood chips or ground wood which offer desired thermal insulation qualities. "When exposed to a humid environment, however, fungal growth on wood and straw is an important consideration. An experimental investigation was conducted in order to evaluate the effectiveness of a simple treatment in mitigating fungal growth on wood- and straw-based insulation. This treatment involved blending of wood chips or particles, or shredded straw, with an aerated slurry that offers the potential to mitigate fungal growth on biomass by a combination of physical and chemical effects without imposing a weight penalty. Experimental results verified the effectiveness of this treatment in controlling fungal growth on wood and straw subjected to different moisture conditions" (Almalkawi, Soroushian , 2019) .

1.2.6 One-Part Alkali Activated Cement Based Volcanic Pumice

A hydraulic cement was developed using abundant natural materials and simple processing methods that relied upon a combination of heating at moderately elevated temperatures and milling. The resulting cement produced viable qualities for use in structural applications. “Pumice, a volcanic tuff, was used as aluminosilicate precursor in production of one-part alkali activated cement. Depending on their cooling rate and aging processes, volcanic tuffs exhibit different degrees of reactivity. The pumice used in this project was subjected to heat treatment followed by mechanochemical processing, together with different naturally occurring sources of alkali or alkaline earth metal cations, into hydraulic (one-part alkali activated) cements. The resultant hydraulic cements were evaluated based on their strength development characteristics via hydration reactions. The particle size distribution and heat of hydration of cement particles, and the chemical composition, mineralogy, bond structure, thermal attributes and morphology of cement particles and hydrated cement paste were also investigated. The results indicated that some of the simple formulations and processing conditions developed in the project produce hydraulic cements with viable structures and strength development qualities” (Almalkawi, Hamadna et al. 2017).

1.2.7 Potential of Using Industrial Wastes For Production Of Geopolymer Binder As Green Construction Materials

“Rice husk ash, Municipal Solid Incineration Ash and coal fly ash was served as aluminosilicate precursor in synthesis of one-part alkali activated geopolymer binder. These by-products industrial wastes were subjected to physio-chemical processing of materials (mechanochemical synthesis) together with different naturally originated sources of alkaline

earth metal cations into one-part alkali activated (geopolymer) binder binders. The binder of hydraulic binders was assessed based on their strength development attributes and morphology with respect to silica content, diffusion of Calcium ions and compositions of Alkali activator. The particle size distribution, the chemical composition, mineralogy, bond environment, of binder particles and effective immobilization of heavy metals of hydrated binder pastes were also inspected. The results highlighted that the ternary blend of combustion ashes to produce hydraulic binders with strength development qualities and safe disposal as material for building construction" (Almalkawi, Balchandra et al. 2019).

CHAPTER 2: PHYSIO-MICROSTRUCTURAL PROPERTIES OF AERATED CEMENT SLURRY FOR LIGHTWEIGHT STRUCTURES

This chapter was first published as “Physio-Microstructural Properties of Aerated Cement Slurry for Lightweight Structures” by Areej T. Almalkawi, Talal Salem, Sameer Hamadna, Darsanasiri, Parviz Soroushian, Anagi Balchandra and Ghassan Al-Chaar in Materials 2018, 11, 597.

2.1 Introduction

Continuous fiber reinforced cement composites and ferrocement are examples of composites used in building construction and repair applications (Prota, Nanni et al. 2004, Bianchi, Arboleda et al. 2013, Nelson, Fam et al. 2014, Donnini, y Basalo et al. 2017). When compared with polymer composites, cementitious composites offer improved fire and moisture resistance, and economics. The density of cementitious matrices, however, is higher than that of polymeric matrices.

One approach to production of cementitious composites involves infiltration of the reinforcement system with a cementitious slurry. Aeration of the slurry offers the opportunity to reduce the density of cementitious matrices. While aeration tends to compromise the strength of cementitious materials, the aerated matrices may still be able to meet the demands on their mechanical performance in the context of composites with relatively high-volume fractions of continuous reinforcement with high specific surface area. These demands are different from those placed on concrete in conventional reinforced concrete structures. The combination of aeration and reinforcement of high specific surface area and close spacing could also provide

desired workability attributes (e.g., ease of screw application and cutting) that would make some wood construction techniques applicable to the material.

Efforts to reduce the density of slurry need to address (besides mechanical performance and interactions with different reinforcement systems such as wire mesh reinforcement) two aspects of the slurry behavior that are of practical significance in this application: (i) sorptivity for protecting the insulation and the interior of the building against moisture transport; and (ii) thermal conductivity for adding value towards enhancing the energy-efficiency of the building.

The synergy between fibers and organic polymers has been key to the emergence of composites as widely used structural materials. In this synergistic action, fibers account for the distinctly high strength and modulus of composites. Organic polymers, on the other hand, provide for stress transfer to fibers, and stress redistribution among fibers upon early rupture of some statistically weaker ones (Mallick 2007). These contributions of the polymer matrix rely heavily upon their strain capacity and desired adhesion to fibers. Given the brittle nature of polymer matrices such as epoxy; it is their relatively low elastic modulus that is responsible for their elongation capacity. The polymer matrix also contributes barrier qualities to composites. The generally open molecular structures of both organic polymers and fibers are responsible for the relatively low density of composites that benefits their 'specific' strength and modulus. Weight saving has been a vital consideration in transition from metals to composites in aerospace and other applications (Mallick 2007).

The work reported herein focuses on development of an inorganic matrix with reduced density and elastic modulus that suits utilization as matrix in continuous fiber reinforced composites that have similarities to ferrocement products. The matrix developed here is an

aerated slurry that offers desired rheological attributes for infiltrating fabric and mesh reinforcement systems. Aerated cementitious materials (e.g., aerated concrete) have been developed mostly to provide thermal insulation qualities (Al-Jabri, Hago et al. 2005, Ng and Low 2010, Alengaram, Al Muhit et al. 2013). This work focused on development of aerated slurries with a relatively low density and modulus and viable strength for use as matrix in structural composites as investigated in our previous studies (Almalkawi, Hamadna et al. 2017, Almalkawi, Hong et al. 2018, Almalkawi, Hong et al. 2018). This aerated slurry-infiltrated mesh is developed as a construction material that offers qualities intermediate between wood and concrete. It is intended to provide a desired balance of relatively low density, ductility, toughness, strength, workability, moisture and fire resistance, and durability under weathering exposure.

2.2 Materials and Methods

The aerated slurry was prepared by mixing the foaming agent (saponin). Saponins are natural surfactants found abundantly in various plant species. More specifically, they are amphipathic glycosides comprising one or more hydrophilic glycoside moieties combined with a lipophilic triterpene derivative (Hostettmann and Marston 1995). Figure 1. shows a saponin molecule obtained from the residues of sisal defibering. It has been used in formulation of detergents (Ribeiro, Barreto et al. 2013).

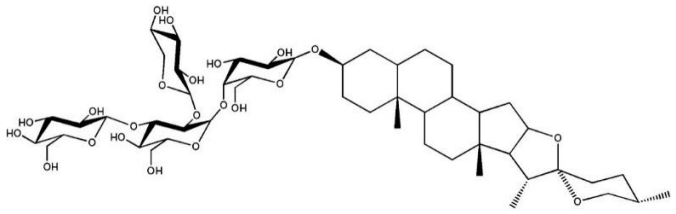

Figure 1. Saponin molecule extracted from sisal waste. (Ribeiro, Barreto et al. 2015).

Aeration of cementitious materials can be accomplished via stabilization of entrapped air using surfactants (Nambiar and Ramamurthy 2007, Ramamurthy, Nambiar et al. 2009, Zhang, Provis et al. 2014), or by the addition of fine powder that generates gas by undergoing chemical reactions with cementitious materials. Aerated concrete has been produced with a wide range of densities (300 to 1800 kg/m^3). The focus of this work is on achieving densities below 1,000 kg/m^3 that are generally viewed as insulating materials.(Uysal, Demirboğa et al. 2004, Jones and McCarthy 2005) Saponin (a hydrolyzed protein extracted from plants) (Fenwick and Oakenfull 1983, Osbourn 1996, Shimoyamada, Ikedo et al. 1998) was used in this work as a surfactant for production of aerated slurry. Saponin was mixed with the mixing water of slurry, and agitated to form foam, which was then mixed with Portland cement type 1 to produce the aerated slurry. As a surfactant, saponin lowers the surface tension of water.

Surfactants are molecules with polar and nonpolar ends that attach to water and air, respectively. The orientation of surfactant molecules in bulk solution is random. Those occurring at the air/liquid interfaces or adsorbed on cement particles, however, have preferred orientations that tend to minimize the unfavorable interactions between the liquid phase and different molecular sections of the surfactant. shows the alignment of a monolayer of surfactant molecules at the interface between air and surrounding liquid phase. The hydrophobic tails of surfactant molecules stick out of the solution to reduce the distortion of water molecules, and

thus lower the overall free energy of the system (Du and Folliard 2005, Murray 2007). The mutual repulsion between the hydrophilic heads of surfactant molecules reduces the attraction of the bulk liquid phase, producing a lower surface tension. Because of the electrostatic component of the repulsion force of ionic surfactants, their effectiveness to reduce surface tension is more significant than that provided by nonionic surfactants (Rosen and Kunjappu 2012). The nature and concentration of surfactants determine the physical and chemical properties of the air bubble/liquid interfaces, including surface tension (equals to free surface energy) and stability. The electrostatic and steric repulsions between surfactants help stabilize the air bubbles formed within the liquid (Binks 2002, Maldonado-Valderrama, Martín-Molina et al. 2007). The hydrophilic ends of the surfactant molecules are also electrostatically attracted to cement particles, that is also a factor in stabilizing the air bubbles within cement paste (Figure 2.).

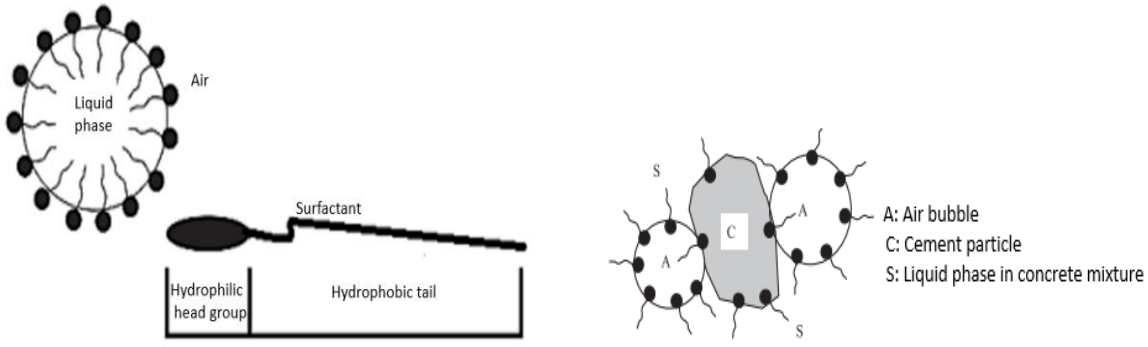

Figure 2. Interaction between air bubbles and cement particles. (Du and Folliard 2005)**.**

Figure 3. Foam generation in water via high-speed mixing.

Saponin and water were mixed at 1200 rpm rotational speed, using a craftsman® mixing blade attached to a drill (**Figure 3**.), to produce foamed water. The foamed mixing water was then added to cement at water/cement ratio of 0.45 to 0.6. Mixing was accomplished in a mortar mixer for 2 minutes. The water/cement ratio of different aerated slurries was adjusted in order to produce a desired fresh mix rheology for infiltrating multiple layers of chicken mesh. The required fresh mix rheology could be defined by a viscosity of about 1900 cP and a yield strength of about 70. The resulting aerated slurry was placed in 50 mm cube molds and kept in sealed condition at room temperature for 24 hours. The cube specimens were then demolded and cured at 95±5% relative humidity and room temperature for 7 days. The aerated slurry mixes proportions considered in this experimental program are introduced in **Table 1**. For the non-aerated slurry (with 0% saponin content), water/cement ratio was between (0.45-0.55)

Table 1. The aerated slurry mixes proportions considered in this investigation.

Mix	Saponin dosage (by weight of cement)	Water/Cement Ratio
1	0.005%	0.45
2	0.01%	
3	0.02%	
4	0.005%	0.50
5	0.01%	
6	0.02%	
7	0.005%	0.55
8	0.01%	
9	0.015%	
10	0.02%	
11	0.025%	
12	0.03%	
13	0.02%	0.6
14	0.025%	

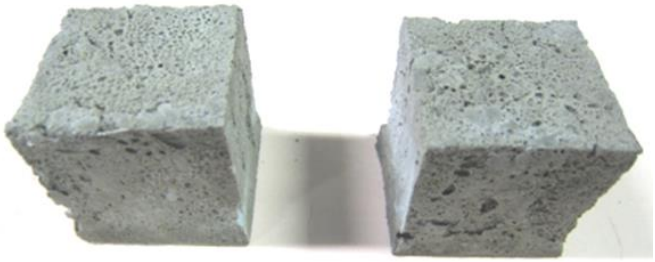

Figure 4. Aerated slurry specimens.

Figure 4. shows examples of the aerated slurry cube specimens, that were tested in compression for measurement of the compressive strength of aerated slurry (at 7 days of age). The density of aerated slurry was measured by dividing the air-dried weight to the volume of these specimens.

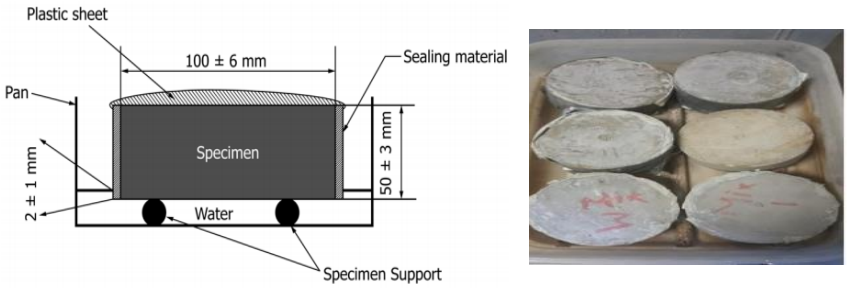

(a) Schematics (b) Picture of multiple specimens during the test

Figure 5. Sorptivity test setup.

The aerated slurry would be the primary protection of the building interior and also the indigenous insulation to be used within the structural panels against weathering effects. Moisture would be transported through the aerated slurry skins (with chicken mesh reinforcement) via capillary sorption. An experimental study was thus undertaken in order to measure the effects of aeration on the capillary sorptivity of the slurry. Sorptivity tests were performed per ASTM C1585; the specimens used for this purpose were cylinders of 100 mm diameter and 50 mm thickness. A schematic of the test setup is shown in **Figure 5a**., and a picture of multiple specimens during sorptivity testing is shown in **Figure 5b**. The specimens were demolded after 24 hours of storage in sealed condition and were cured at room temperature until the test age. This test method involves exposure of one flat surface of specimen to water, which the remaining surfaces sealed against moisture loss. Mass gain over time is recorded as a measure of moisture sorption. Sorptivity is expressed in terms of the sorption rate of moisture into the aerated slurry. This test was continued for 2 days in order to gain further insight into schematic time-history of capillary sorption (Hall and Yau 1987, Dias 1993).The ultrasound pulse velocity (UPV) of aerated slurry was measured nondestructively using a portable equipment (manufactured by PUNDIT). The UPV test setup is shown in **Figure 6**. In this test, an ultrasonic

pulse is generated and transmitted to the surface of concrete through the transmitter transducer. The time taken by the pulse to travel through the aerated slurry, t_{us}, is measured by the receiver transducer on the opposite side. The 54 kHz transducers were positioned at the center of each opposing face. The propagation time of the ultrasonic waves transmitted through the 150 mm long cylindrical specimens was measured with accuracy up to 0.1 s. A thin couplant (solid blue Vaseline) was used at the interface between transducers and the aerated slurry specimen surfaces to ensure good contact. The pulse travel time (t) from the front side to the rear side was automatically recorded. The ultrasound pulse velocity was measured approximately 50 hours after mixing of the aerated slurry (Liu, Zhang et al. 2011, Zhang, Zhang et al. 2012, Wei, Yunsheng et al. 2014). The specimens used for performance of the ultrasound pulse velocity were prepared from aerated slurry mixes of similar proportions as those used for other experiments; the mixes used for preparation of the ultrasound pulse velocity specimens, however, were not the same as those used for preparation of the specimens used in other tests. All specimens were cured at room temperature and 95±5% relative humidity.

Figure 6. Ultrasound pulse velocity test setup.

The thermal conductivity of aerated slurry test was measured at 7 days of age in accordance to ASTM C177. Aerated slurry cement specimens were oven dried for 24 h at a

temperature of 105±5°C. **Figure 7.** shows the thermal conductivity testing configuration and test setup. The specimen was placed between hot and cold plates with 40◦C and 18◦C, respectively, to simulate outdoor and indoor temperatures. Temperatures on the hot and the cold plates as well as the heat flow were recorded versus time over 24 hours. The results, after the process reached equilibrium, were used to calculate the thermal conductivity of aerated slurry.

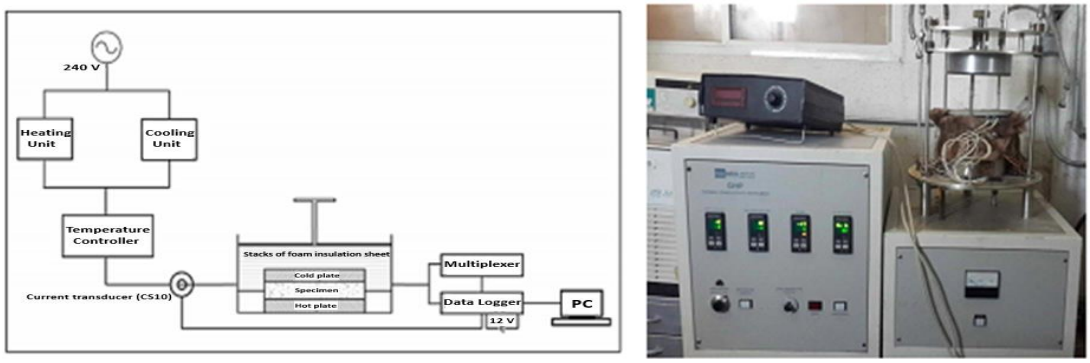

Figure 7. Thermal conductivity testing diagram and test setup.

Furthermore, an aerated slurry samples were subjected to SEM observation to evaluate microstructural features. SEM observations were carried out on JCM-5000 NeoScope™ at an accelerating voltage of 10-15 kV using a secondary electron (SE) detector. The investigations were conducted on fracture surfaces of the paste of the samples after 28 days. Samples were sputtered with gold before the SEM measurements.

2.3 Experimental Results and Discussion

2.3.1 Compressive strength

Table 2. presents the measured values of 7-day compressive strength and density for the aerated slurry mix designs introduced earlier in **Table 1**. Lower values of density tend to correspond with lower values of compressive strength. This is both because of the rise in air content and also the increase in water/cement ratio for achieving viable fresh mix rheology. Mix 13 with density of 0.9 g/cm^3 and 5.4 MPa compressive strength at 7 days provides a viable balance of density and strength for the targeted ferro-cement application. This paper strongly emphasize the density of aerated slurry in order to enhance the efficiency of seismic design (Guo, Juan et al. 2011, Ohsaki, Miyamura et al. 2016) and also enable manual installation of the building structure.

Table 2. Mix designs and performance characteristics of the aerated slurry.

Mix	7-Day compressive strength, MPa	Density, g/cm^3
1	10.7	1.9
2	8.2	1.5
3	6.3	1.4
4	14.1	1.2
5	10.5	1.81
6	9.2	1.3
7	13.3	1.6
8	11.1	1.7
9	9.4	1.3
10	6.4	1.17
11	2.4	0.65
12	1.2	0.8
13	5.4	0.9
14	7.1	1.12

2.3.2 Sorptivity

The sorptivity test results are presented in **Figure 9.** as the capillary rise of moisture versus time for aerated slurries prepared with different dosages of the foaming agent (saponin), with water/cement ratio of 0.55. The two higher dosages of foaming agent (0.015% and 0.02%) are

observed to produce lower sorption rates and capacities. This is a positive trend, indicating that lowering the density of the slurry via aeration would actually improve its barrier qualities for protecting the building interior as well as the natural insulation against weathering effects.

The initial sorption rate (S_i) is the slope of the sorption curve shown in **Figure 8.** up to 6 hours; the secondary sorption rate is the slope of the curve after 1 day. Both these calculations are made using a linear regression analysis (ASTM C1585):

$$I = S_i \times \sqrt{t} + b$$

The resulting values of initial and secondary sorption rate are presented in **Table 3**. together with the corresponding values of the aerated slurry density. These results confirm that lowering the density of aerated slurry from 1.7 to 1.17-1.3 g/cm^3 leads to a significant drop in the initial and secondary sorption rates of the slurry. This can be explained by the fact that aeration introduces isolated air bubbles into the slurry, which disrupt the continuity of capillary pores through which sorption occurs (Prim and Wittmann 1983, Tada and Nakano 1983, Goual, De Barquin et al. 2000, Giannakou and Jones 2002, Madjoudj, Quenendec et al. 2002, Nambiar and Ramamurthy 2007). An overall sorptivity value is also presented in **Table 3**. which is the slope of a regression line fit into the whole data points (using the above equation). The overall sorptivity values further confirms the drop in sorption rate with reduction of the density of aerated slurry.

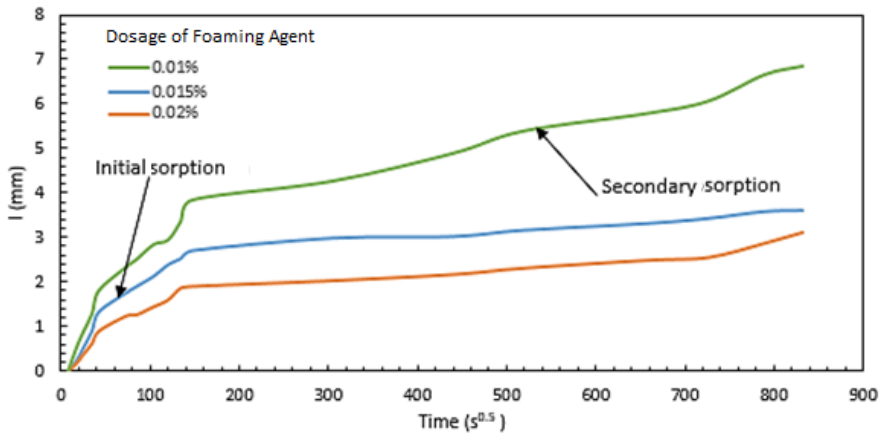

Figure 8. Capillary sorption of aerated slurries versus the square root of time.

Table 3. Sorption rates and densities of slurries prepared with different dosages of the foaming agent.

Dosage of foaming agent %	**0.01%**	**0.015%**	**0.02%**
Initial sorption rate, mm/√s	0.0242	0.0188	0.0132
Secondary sorption rate, mm/√s	0.0044	0.0013	0.0019
R^2 (Regression value)	0.951	0.950	0.958
Density, g/cm^3	1.7	1.3	1.17
Sorptivity, mm/min$^{0.5}$	0.75	0.5	0.34

In order to confirm the finding that aeration actually reduces the sorption rate and extent of slurry (i.e., enhances its barrier qualities), tests were also performed on a slurry without any aeration. The sorption test data presented in **Figure 9.** Sorptivity of non-aerated versus aerated slurries. confirm that aeration reduces the rate and extent of moisture sorption into the slurry. As schematically depicted in **Figure 10.** introduction of isolated air bubble forces tortuous sorption paths through capillary pores, which reduce the sorption rate of the slurry. The experience with entrained air bubbles indicates that individual air bubbles remain largely empty of water even under long-term exposure to moist conditions. This phenomenon as well as the reduction in the rate of moisture sorption explain the drop in the extent of moisture sorption with introduction of individual air bubbles via aeration of slurry.

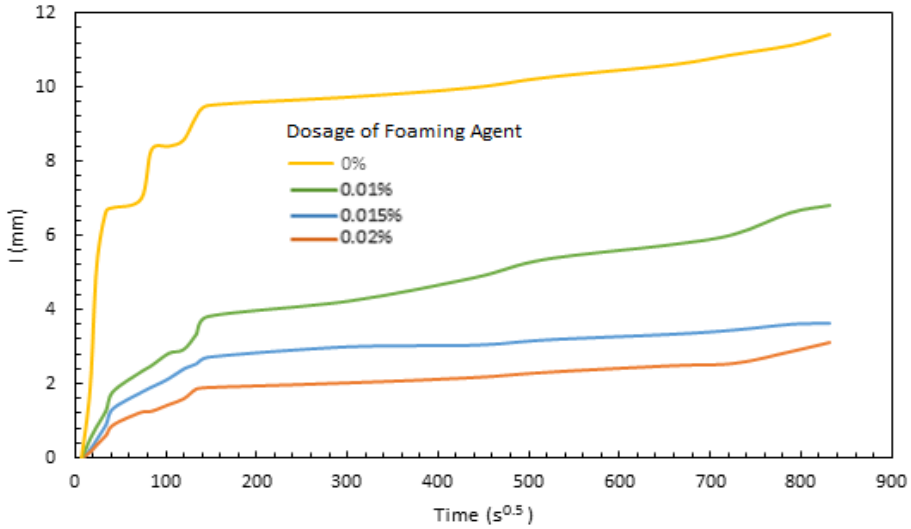

Figure 9. Sorptivity of non-aerated versus aerated slurries.

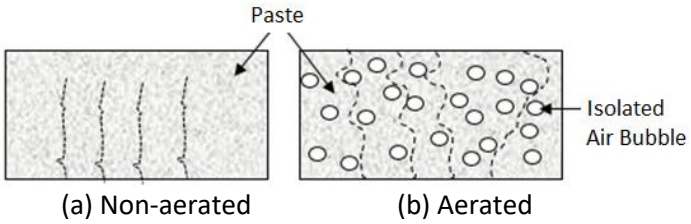

Figure 10. Sorption paths into non-aerated and aerated slurries.

2.3.3 Optic Microscope

Optic microscope images were obtained from sections of aerated slurries prepared with different dosages of the foaming agent in order to understand the morphology of air bubbles and explain their effects on compressive strength. **Figures 11a.** and **11b**. show microscopic images of slurries prepared with 0.005% and 0.02% concentrations of the foaming agent, respectively. A rise in the foaming agent dosage is observed to increase the size (as well as the volume fraction) of air bubble. It should be noted that smaller and regularly formed air bubbles produce higher compressive strengths than coarser and irregularly formed air bubbles (Just and Middendorf 2009). Mechanical properties are strongly influenced by the distribution of pores within the hardened aerated slurry (Olorunsogo and Wainwright 1998, Kearsley and Wainwright 2002). The

spherical and distributed nature of foams in **Figure 11b.** with higher air content led to a viable level of compressive strength which was not lower than that provided by the aerated slurry shown in **Figure 11b**. with lower content of irregularly shaped air bubbles. This observation confirms that microstructural properties are primary factors influencing the material properties of aerated slurry (Dhir and Henderson 1999). An example optic microscope image of an exterior surface of an aerated slurry of higher compressive strength is shown in **Figure 12.**, where finer and more uniformly dispersed air bubbles can be observed.

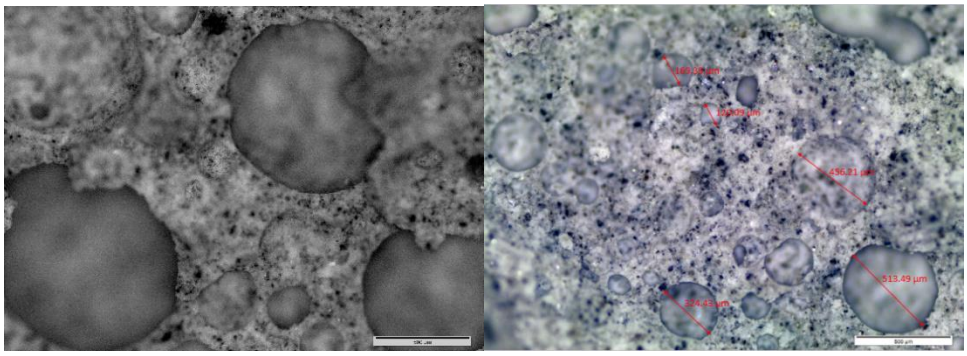

(a) 0.005% foaming agent (b) 0.02% foaming agent

Figure 11. Optical microscope images of sections of aerated slurries with different dosages of the foaming agent (saponin).

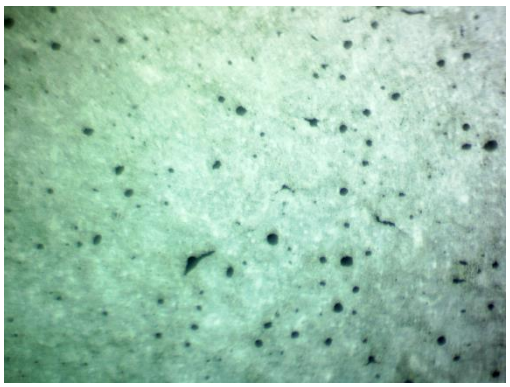

Figure 12. Optical microscope images of sections of aerated slurries with different dosages of the foaming agent (saponin).

2.3.4 SEM Observations

The spherical geometry of air voids is an important factor influencing the structural and functional properties of aerated binders (Valore 1954, Prim and Wittmann 1983). In addition, the voids should be distributed evenly in the mass to produce homogenous binders of improved performance. Larger voids (macro-pores) would lower the density of aerated slurry but could compromise its mechanical performance. Depending on the type and dosage of the foaming agent, aerated cement slurries may incorporate both micro- and macro-pores (Sugama, Brothers et al. 2005). Macro-pores could be formed as a result of the merger of micro-pores. This is because expansion of the matrix upon micro-pore formation generates pressure at the interfaces between micro-pores(Alexanderson 1979). **Figure 13a.** shows an SEM image of an aerated slurry after hydration.

Aside from the gel pores (<10 nm) and capillary pores (10 nm to 10 μm), hollow shell pores have been proposed as a third category of intrinsic pores in bulk of hydration products (Sugama, Brothers et al. 2005). Hollow shells have range in size from 1 to around 20 μm, about the size of smaller cement grains, embedded in cement gel and channeled to the outside through capillary and gel pores.

An ideal microstructure of aerated cement minimizes the extent of water transport by uniformly distributing the discrete micro-size pores generated by the foaming agent within the cement slurry. The coalescence of many irregular-shaped pores, however, may create a disturbed microstructure, triggering a high degree of water mobility. In order to verify this, two fractured samples of aerated slurries with 0.75 and 1.3 g/cm^3 bulk densities were examined using a scanning electron microscope (**Figure 13b**. and **Figure 13c.**, respectively). The image on the right,

for the slurry with 1.3 g/cm^3 bulk density, shows a microstructure of uniformly distributed disjunctive pores. In contrast, a different microstructure was observed for the aerated slurry with 0.75 g/cm^3 bulk density (left) where an anomalous coalescence developed, yielding a channeled pore structure. This structure allows water to pervade easily through the aerated slurry. A possible explanation for the formation of such an anomalous pore structure is the inclusion of tremendous numbers of air bubble cells using an excess amount of foaming agent, which promotes the coalescence of air bubbles as a result of the collapse of the slurry walls separating these bubbles.

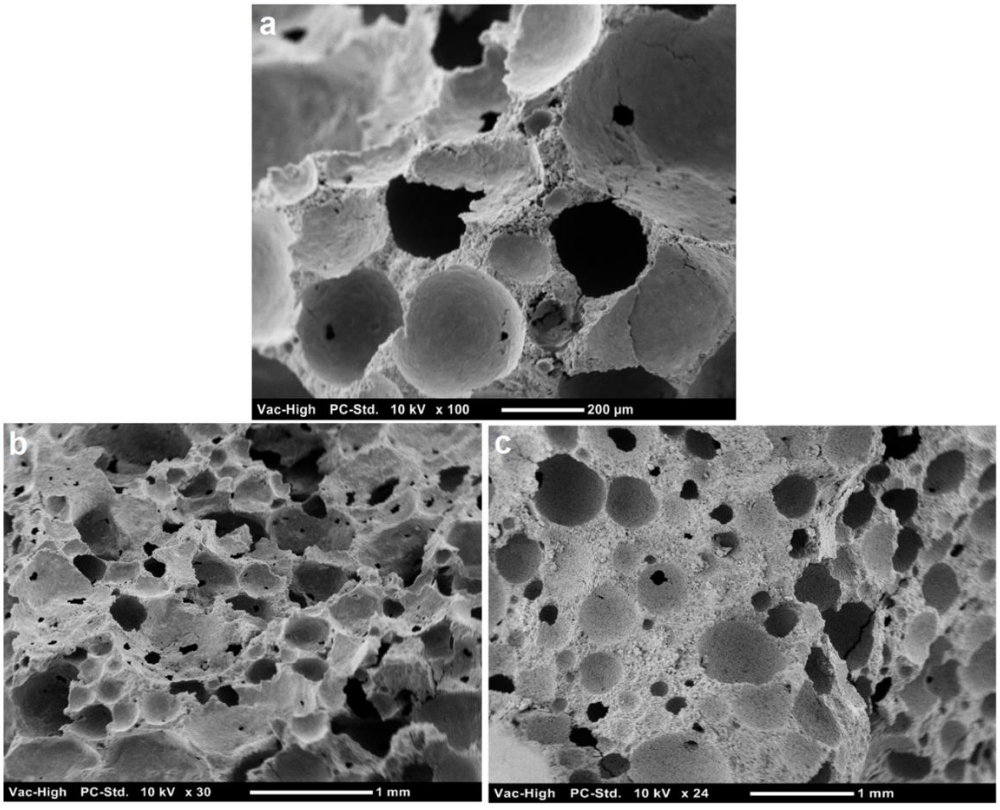

Figure 13. SEM images of the fractured surfaces of foam cements made from slurries with a density of 0.75 (left) and 1.3 g/cm3 (right).

2.3.5 Ultrasound Pulse Velocity

Ultrasound pulse velocity (UPV) is a simple nondestructive means of evaluating concrete, which could be used to assess the aerated slurry quality and its development over time.

Figure 14. shows the evolution of ultrasound pulse velocity over time (up to 50 hours) after mixing for three aerates slurries with different densities. UPV is observed to be higher for aerated slurries of higher density. At earlier ages, lower-density aerated slurries exhibit a minor rise in UPV for more than 10 hours while the higher-density slurry exhibits a clear trend towards UPV rise as soon as 1 hour after mixing.

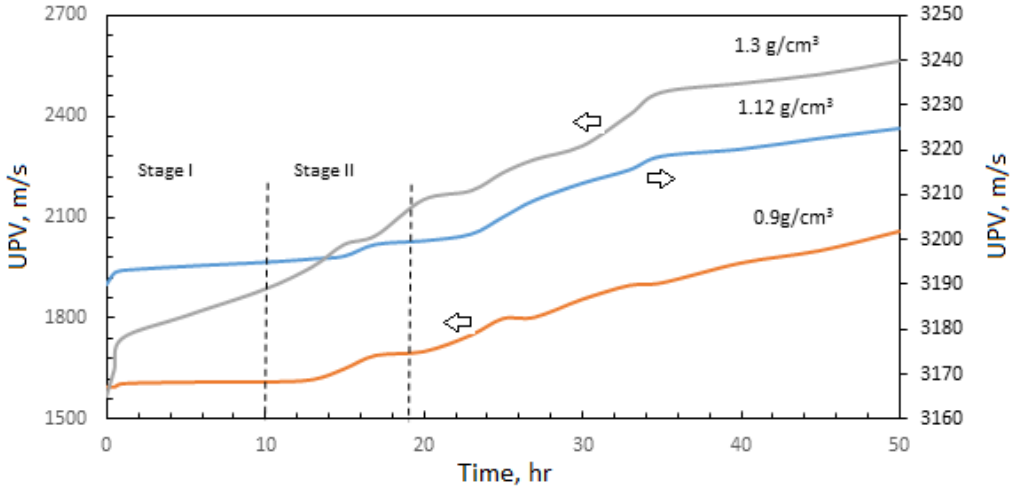

Figure 14. UPV time-history for aerated slurries of different densities.

In order to assess the variability of UPV measurements, three replicated aerated slurry specimens were prepared with the same mix design (Mix 13) and density (0.9 g/cm^3). The evolution of UPV with time is presented in **Figure 15**. for the three replicated specimens. The variations in UPV for these three test specimens are less than 6%, pointing at the potential value of UPV as a reliable method of monitoring the quality of aerated slurry (and its evolution with time of curing).

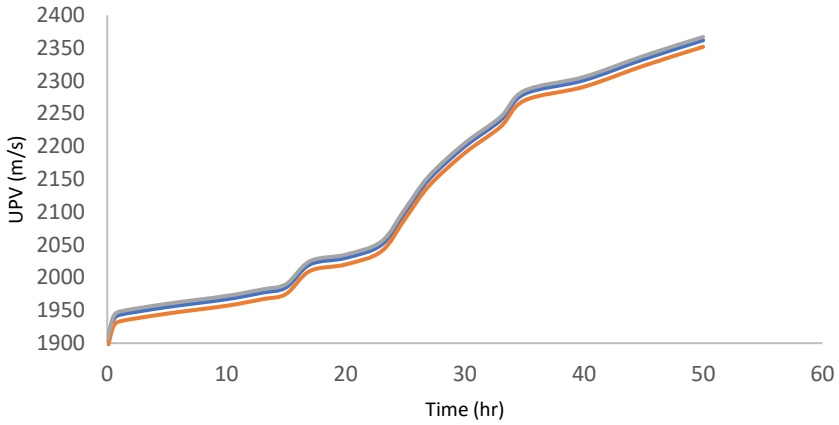

Figure 15. Reproducibility check on three UPV tests for the same mix design (Mix 13).

2.3.6 Thermal Conductivity

The lightweight aerated slurry is expected to make some contributions towards thermal insulation of the building. The measured values of thermal conductivity are shown in **Figure 16**. versus the density of aerated slurries. As expected, slurries of lower density offer lower values of thermal conductivity (Ng and Low 2010, Saygılı and Baykal 2011, Sengul, Azizi et al. 2011). Air bubbles act as barriers against thermal conduction; the isolated air bubbles do not make any significant contributions to heat transfer via convection (Alengaram, Al Muhit et al. 2013).

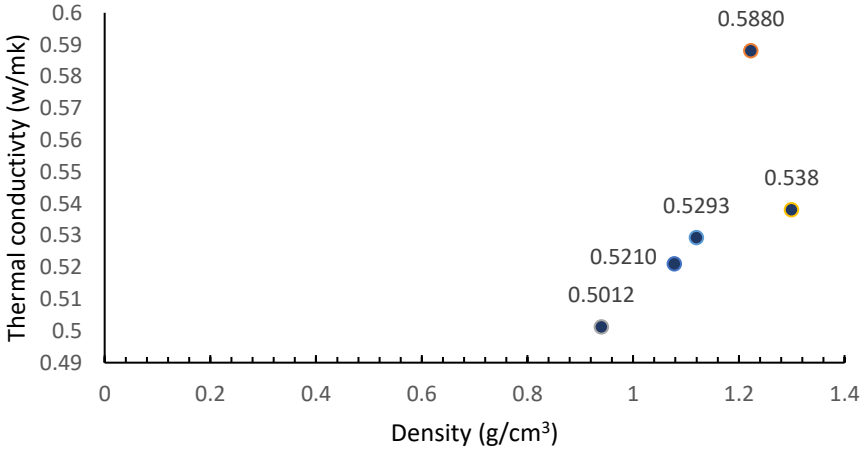

Figure 16. Thermal conductivity of aerated slurries versus their density.

2.4 Conclusions

Aerated slurry is developed as a lightweight matrix for production of cementitious composites embodying reinforcement of high specific surface area for structural applications. A highly flowable slurry is needed for thorough infiltration of the structural volume that is congested with fine reinforcement systems. This work developed and characterized an aerated slurry comprising a cementitious material of relatively high water/cement ratio that incorporated a foaming agent (saponin). High-speed mixing of the mixing water incorporating saponin produces the foamed water that is then used to prepare the aerated slurry by mixing with cement. The following conclusions were derived by conducting an experimental program on slurries of various densities (adjusted by varying the saponin content).

1. While lowering the density of the aerated slurry by increasing the dosage of foaming agent tends to lower its compressive strength, this relationship is not consistent. Production of fine, spherical and uniformly distributed air bubbles in aerated slurry favors achievement of higher compressive strengths.

2. Aeration of slurry benefits its moisture barrier qualities, which benefits its durability. The isolated air bubbles in aerated slurry seem to act as barriers against capillary sorption of moisture into the slurry, thus forcing tortuous diffusion paths. The extent of moisture sorption by slurry is also lowers with increasing air content. This could be attributed to the tendency of the isolated air bubbles to remain largely filled with air when the aerated slurry is exposed to moisture.

3. Aeration of the cement slurry significantly reduces its thermal conductivity, which benefits the energy-efficiency of building systems. The low thermal conductivity of air in the bubbles introduced via aeration, and the lack of effective convection due to the isolated nature of air

bubbles explain the benefits of aeration towards the insulation value of aerated slurry.

4. Ultrasound pulse velocity provides an effective nondestructive means of controlling the quality of aerated slurry and its evolution with time. This method can be conveniently implemented in field conditions for assessing the quality of aerated slurry, and its evolution with time.

2.5 Acknowledgments

The work reported herein was funded by the U.S. Army Grant No. W9132T-16-C-003-United States.

REFERENCES

REFERENCES

Alengaram, U.J., et al., A comparison of the thermal conductivity of oil palm shell foamed concrete with conventional materials. Materials & Design, 2013. 51: p. 522-529.

Alexanderson, J., Relations between structure and mechanical properties of autoclaved aerated concrete. Cement and Concrete Research, 1979. 9(4): p. 507-514.

Al-Jabri, K.S., et al., Concrete blocks for thermal insulation in hot climate. Cement and Concrete Research, 2005. 35(8): p. 1472-1479.

Almalkawi, A.T., et al., Behavior of a lightweight frame made with aerated slurry-infiltrated chicken mesh under cyclic lateral loading. Construction and Building Materials, 2018. 160: p. 679-686.

Almalkawi, A.T., et al., Mechanical properties of aerated cement slurry-infiltrated chicken mesh. Construction and Building Materials, 2018. 166: p. 966-973.

Almalkawi, A.T., S. Hamadna, and P. Soroushian, One-part alkali activated cement based volcanic pumice. Construction and Building Materials, 2017. 152: p. 367-374.

Bianchi, G., et al. Fabric reinforced cementitious matrix (FRCM) materials for structural rehabilitation. In Proceedings of the 39th IAHS World Congress. 2013.

Chen, Ying-Liang, et al. “Recycling of desulfurization slag for the production of autoclaved aerated concrete.” Construction and Building Materials 158 (2018): 132-140.

Dhir, R.K. and N.A. Henderson, Specialist Techniques and Materials for Concrete Construction. 1999: Institution of Civil Engineers.

Donnini, J., et al., Fabric-reinforced cementitious matrix behavior at high-temperature: Experimental and numerical results. Composites Part B: Engineering, 2017. 108: p. 108-121.

Du, L. and K.J. Folliard, Mechanisms of air entrainment in concrete. Cement and concrete research, 2005. 35(8): p. 1463-1471.

Fenwick, D.E. and D. Oakenfull, Saponin content of food plants and some prepared foods. Journal of the Science of Food and Agriculture, 1983. 34(2): p. 186-191.

Giannakou, A. and M. Jones, Potentials of foamed concrete to enhance the thermal performance of low rise dwellings. Innovations and development in concrete materials and construction. UK: Thomas Telford, 2002: p. 533-44.

Goual, M., et al., Estimation of the capillary transport coefficient of Clayey Aerated Concrete using a gravimetric technique. Cement and Concrete Research, 2000. 30(10): p. 1559-1563.

Guo, M., et al., Seismic performance experimental research for multi-ribbed composite wall strengthened with aerated concrete blocks. Journal of Sichuan University: Engineering Science Edition, 2011. 43(1): p. 51-57.

Hall, C. and M.R. Yau, Water movement in porous building materials—IX. The water absorption and sorptivity of concretes. Building and environment, 1987. 22(1): p. 77-82.

Jones, M. and A. McCarthy, Preliminary views on the potential of foamed concrete as a structural material. Magazine of concrete research, 2005. 57(1): p. 21-32.

Just, A. and B. Middendorf, Microstructure of high-strength foam concrete. Materials characterization, 2009. 60(7): p. 741-748.

Kearsley, E. and P. Wainwright, The effect of porosity on the strength of foamed concrete. Cement and Concrete Research, 2002. 32(2): p. 233-239.

Liu, Yiquan, et al. "Autoclaved aerated concrete incorporating waste aluminum dust as foaming agent." Construction and Building Materials 148 (2017): 140-147.

Liu, Z., et al., In situ continuously monitoring the early age microstructure evolution of cementitious materials using ultrasonic measurement. Construction and Building Materials, 2011. 25(10): p. 3998-4005.

Madjoudj, M., M. Quenendec, and R. Dheilly, Water capillary absorption of cellular clayed concrete obtained by proteinic foaming. Innovations and development in concrete materials and construction, Thomas Telford, UK, 2002: p. 513-521.

Maldonado-Valderrama, J., et al., Surface properties and foam stability of protein/surfactant mixtures: theory and experiment. The Journal of Physical Chemistry C, 2007. 111(6): p. 2715-2723.

Mallick, P.K., Fiber-reinforced composites: materials, manufacturing, and design. 2007: CRC press.

Melo, Javier Pinilla, et al. "Rheological and thermal properties of aerated sprayed mortar." Construction and Building Materials 154 (2017): 275-283.

Nambiar, E.K. and K. Ramamurthy, Air-void 31haracterization of foam concrete. Cement and concrete research, 2007. 37(2): p. 221-230.

Nambiar, E.K. and K. Ramamurthy, Sorption characteristics of foam concrete. Cement and Concrete Research, 2007. 37(9): p. 1341-1347.

Nelson, M., et al., Fiber-reinforced polymer stay-in-place structural forms for concrete bridge decks: State-of-the-art review. ACI Structural Journal, 2014. 111(5): p. 1069.

Ng, S.-C. and K.-S. Low, Thermal conductivity of newspaper sandwiched aerated lightweight concrete panel. Energy and Buildings, 2010. 42(12): p. 2452-2456.

Ohsaki, M., et al., Seismic Response Simulation of Building Structures, in High-Performance Computing for Structural Mechanics and Earthquake/Tsunami Engineering. 2016, Springer. P. 105-139.

Olorunsogo, F.T. and P.J. Wainwright, Effect of GGBFS particle-size distribution on mortar compressive strength. Journal of materials in civil engineering, 1998. 10(3): p. 180-187.

Osbourn, A., Saponins and plant defence—a soap story. Trends in plant science, 1996. 1(1)

Prim, P. and F. Wittmann, Structure and water absorption of aerated concrete. Autoclaved Aerated Concrete, Moisture and Properties, Elsevier, Amsterdam, 1983: p. 43-53.

Prim, P. and F. Wittmann, Structure and water absorption of aerated concrete. Autoclaved aerated concrete, moisture and properties, 1983: p. 55-69.

Prota, A., et al., Selective upgrade of underdesigned reinforced concrete beam-column joints using carbon fiber-reinforced polymers. ACI structural journal, 2004. 101(5): p. 699-707.

Qu, Xiaoling, and Xuguang Zhao. "Previous and present investigations on the components, microstructure and main properties of autoclaved aerated concrete–A review." Construction and Building Materials 135 (2017): 505-516.

Ramamurthy, K., E.K. Nambiar, and G.I.S. Ranjani, A classification of studies on properties of foam concrete. Cement and Concrete Composites, 2009. 31(6): p. 388-396.

Ribeiro, B.D., D.W. Barreto, and M.A.Z. Coelho, Use of micellar extraction and cloud point preconcentration for valorization of saponins from sisal (Agave sisalana) waste. Food and Bioproducts Processing, 2015. 94: p. 601-609.

Rosen, M.J. and J.T. Kunjappu, Surfactants and interfacial phenomena. 2012: John Wiley & Sons.

Saygılı, A. and G. Baykal, A new method for improving the thermal insulation properties of fly ash. Energy and Buildings, 2011. 43(11): p. 3236-3242.

Sengul, O., et al., Effect of expanded perlite on the mechanical properties and thermal conductivity of lightweight concrete. Energy and Buildings, 2011. 43(2): p. 671-676.

Shimoyamada, M., et al., Effects of soybean saponins on chymotryptic hydrolyses of soybean proteins. Journal of Agricultural and Food Chemistry, 1998. 46(12): p. 4793-4797.

Siline, Mohammed, Elhem Ghorbel, and Mekki Bibi. "Effect of freeze–Thaw cycles on the physicomechanical properties of a pozzolanic mortar." Construction and Building Materials 134 (2017): 32-38.

Sugama, T., L. Brothers, and T. Van de Putte, Air-foamed calcium aluminate phosphate cement for geothermal wells. Cement and Concrete Composites, 2005. 27(7): p. 758-768.

Tada, S. and S. Nakano, Microstructural approach to properties of moist cellular concrete. Proceedings Autoclaved Aerated Concrete, Moisture and Properties. Amsterdam: Elsevier, 1983: p. 71-89.

Uysal, H., et al., The effects of different cement dosages, slumps, and pumice aggregate ratios on the thermal conductivity and density of concrete. Cement and concrete research, 2004. 34(5): p. 845-848.

Valore, R.C. Cellular concretes Part 1 composition and methods of preparation. In Journal Proceedings. 1954.

Wei, S., Z. Yunsheng, and M. Jones, Using the ultrasonic wave transmission method to study the setting behavior of foamed concrete. Construction and Building Materials, 2014. 51: p. 62-74.

Zhang, Y., et al., Ultrasound monitoring of setting and hardening process of ultra-high performance cementitious materials. NDT & E International, 2012. 47: p. 177-184.

Zhang, Z., et al., Geopolymer foam concrete: an emerging material for sustainable construction. Construction and Building Materials, 2014. 56: p. 113-127.

CHAPTER 3: MECHANICAL PROPERTIES OF AERATED SLURRY-INFILTRATED CHICKEN MESH

This chapter was first published as "Mechanical Properties of Aerated Slurry-Infiltrated Chicken Mesh" by Almalkawi, Areej T., Weisheng Hong, Sameer Hamadna, Parviz Soroushian, A. G. N. D. Darsanasiri, Anagi Balchandra, and Ghassan Al-Chaar. Construction and Building Materials 166 (2018): 966-973.

3.1 Introduction

Aerated concrete is traditionally viewed as an insulating (non-structural) building material. This investigation evaluated the potential to improve the mechanical performance of aerate concrete through the use of a chicken mesh as a continuous reinforcement system with high specific surface area. There is a growing interest in the use of wire mesh reinforcement in concrete panels (Joseph, Prabakar et al. 2017, Liu, Wu et al. 2017). Within certain limits, the mesh behaves as homogeneous reinforcement, and produces concrete composites with desired tensile strength-to-weight ratio, cracking behavior and impact resistance (Wafa and Fukuzawa 2010). Ferrocement, a cementitious mortar with wire mesh reinforcement, benefits from these advantages associated with the use of nearly isotropic reinforcement systems of high specific surface area and desired mechanical bonding (Naaman 2000). This work is part of ongoing research that aspire smart utilization of lightweight material in congestion with chicken mesh for structural applications (Almalkawi, Hong et al. 2018).

The main thrust of the work reported herein was to develop a construction material that combines the advantages of wood (ductility, low bulk density, convenient use of fasteners such as screws, etc.) with those of reinforced concrete (moisture, weathering and decay resistance, load-bearing capacity, etc.). Achievement of these goals required use of relatively high reinforcement ratios, which necessitated the use of slurry infiltration in lieu of, say, troweling of mortar that is used in the case of ferrocement. Slurry infiltration enables through embedment of the chicken mesh wire in the cementitious matrix in spite of the congestion of volume with the required chicken mesh volume ratio. Aeration of the slurry was required to reduce the bulk density of the material. Chicken mesh (poultry netting) was used in this development as a readily available reinforcement system of high specific surface area with desired mechanical bonding potential in aerated slurry.

Streamlined methods were devised for producing aerated slurry-infiltrated chicken mesh as a structural material. An experimental program was conducted in order to gain insight into the mechanical performance of this material. The effects of chicken mesh reinforcement on the compressive strength of aerated slurry was investigated. The effect of aeration of slurry on the system performance was also evaluated. A semi-empirical theoretical basis was developed for the mechanical behavior of aerated slurry-infiltrated chicken mesh.

3.2 Experimental Program

3.2.1 Materials

3.2.1.1 Aerated Slurry

The slurry mix was prepared in this investigation with Type I Portland cement and tap water. In one of the mixtures, in order to achieve a viable fresh mix workability, a polycarboxylate-based superplasticizer was used. The aerated slurry was prepared by adding a foaming agent to the mixing water of slurry. Aeration introduces a homogenous system of fine air bubbles into the cement paste. This is accomplished using foaming agents that stabilize the air voids generated by agitating the mixing water of slurry to which the foaming agent has been added (Nambiar and Ramamurthy 2007, Ramamurthy, Nambiar et al. 2009, Zhang, Provis et al. 2014). Preparation of the aerated slurry started with production of foamed water. For this purpose , a foaming agent extracted from plants (saponin) was blended with the mixing water at 1200 rpm rotational speed using a mixing blade attached to a drill **Figure 17**. The resulting foamed water was then added to cement and mixed in a mortar mixer for 6 minutes. Current investigations are carried out to produce aerated alkali activated cement based volcanic tuff and limestone (Almalkawi, Hamadna et al. 2017)

(a) Prior to stirring (b) Foaming after stirring

Figure 17. Preparation of foamed water by stirring the mixing water incorporating the foaming agent.

3.2.1.2 Chicken Mesh

This work chose chicken mesh (hexagonal 20-gauge galvanized poultry netting) as a steel reinforcement system of high specific surface area. This selection was made due to the broad worldwide availability of chicken mesh. The common mesh used in this investigation was made of steel wires of 1 mm diameter (0.785 mm^2 cross sectional area). Chicken meshes are available with different wire diameters and spacings. The spacing of hexagonally configured wires generally increase with increasing wire diameter in order to provide comparable wire cross-sectional areas per unit width. Given the relatively large layers of chicken mesh that need to be infiltrated with aerated slurry, the preference in this investigation was for chicken meshes with larger wire diameter and spacing. The chicken mesh used in this investigation was non-isotropic. The stronger direction (vertical in **Figure 18**.) is referred to as longitudinal in this work.

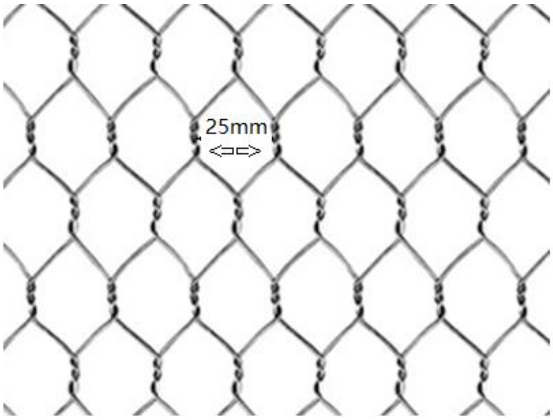

Figure 18. The chicken mesh used in the experimental program.

3.3 Experimental Methods

An experimental program was conducted in order to evaluate the effects of some key variables on the mechanical properties of aerated slurry-infiltrated chicken mesh under compressive, flexural and tensile loading. The interactions of chicken mesh with aerated slurry can be characterized as more complex than those between concrete and conventional reinforcing bars. More attention should be paid to the contributions of the aerated (slurry) matrix towards timely mobilization of the load-bearing capacity of the multiple chicken mesh layers tightly incorporated into the aerated slurry. Test results would be critical to understanding these complex interactions. Aerated slurry-infiltrated chicken mesh can, due to the high specific surface area of steel reinforcement, provide distinctly high levels of ductility and energy dissipation capacity. In addition, the high specific surface area and close spacing of chicken mesh wires could benefit various aspects of the aerated slurry performance, including its compressive strength, dimensional stability and resistance to shrinkage cracking. The experimental methods used for evaluating the mechanical behavior of aerated slurry-infiltrated chicken mesh are presented in the following results. The experimental were used to develop semi-empirical models for

predicting the mechanical performance of aerated slurry-infiltrated chicken mesh.3.3.1. Tests performed on slurry without chicken mesh reinforcement

The experimental work reported here used one non-aerated slurry as control, and different aerated slurry mixtures. The non-aerated slurry comprised cement: water: superplasticizer at 1: 0.36: 0.004 weight ratios. For the purpose of preparing the aerated slurry mixtures, the foaming agent was added to water and subjected to stirring at relatively high speed in order to product foamed mixing water, which was then added to cement and mixed using normal mixing procedures. The water/cement ratio of aerated slurry mixtures ranged from 0.40 to 0.55. The aerated slurry mix proportions are introduced in **Table 4**.The resulting aerated slurry was placed in 50 mm cube molds for compression strength test and bulk density measurement. The specimens kept in sealed condition at room temperature for 24 hour and cured at 95% relative humidity and room temperature for 7 days.

Table 4. The aerated slurry mix proportions.

Mix	Foaming Agent Dosage, % by wt.	Water/cement ratio
0	0	0.35 with 0.004 superplasticizer
1	0.005%	0.45
2	0.01%	
3	0.02%	
4	0.005%	0.50
5	0.01%	
6	0.02%	
7	0.005%	0.55
8	0.01%	
9	0.015%	
10	0.02%	
11	0.025%	

Table 4 (cont'd)

12	0.03%	
13	0.02%	0.6
14	0.025%	

3.3.1 Tests performed on aerated slurry-infiltrated chicken mesh

3.3.1.1 Compression

The prismatic compression test specimens had planar dimensions of 102 mm by 102 mm, with a height of 229 mm. The chicken mesh configuration used in compression testing of aerated slurry-infiltrated chicken mesh specimens is presented in **Figure 19.** There were two groups of chicken mesh in these specimens: (i) 30 interior layers placed in folded form; and (ii) four exterior layers wrapped around the interior layers to mitigate the potential for split cracking upon screw application to the surface. Along the height, where the chicken mesh layers are oriented in their strong direction, the total number of chicken mesh layers is thus 38. The aerated slurry mixture comprised cement: water: saponin at 1: 0.6: 0.00045 weight ratios.

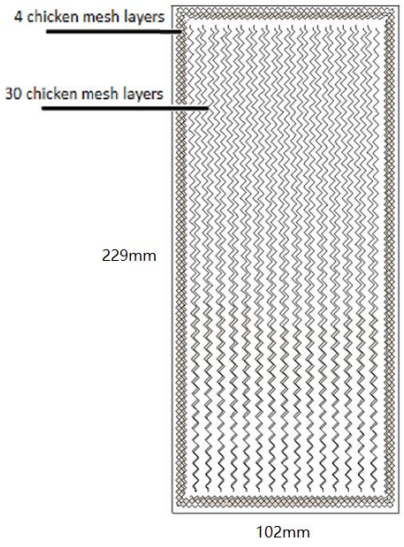

Figure 19. Aerated slurry-infiltrated chicken mesh compression test specimen.

3.3.1.2 Tension

Aerated slurry infiltrated chicken mesh sheets with 20 mm thickness and 150 mm width were subjected to tension testing. The number of chicken mesh layers in different tension test specimens varied from 12 to 24. The chicken mesh layers were oriented to that the tensile force was resisted in their strong direction. The tension test setup is shown in **Figure 20**. The free length of the tension test specimen between the two grips was 310 mm (with a total specimen length of 500 mm). Tension tests were performed at a constant displacement rate of 0.05 mm/s. The values of load and deflection were recorded during the tension tests using a data acquisition system.

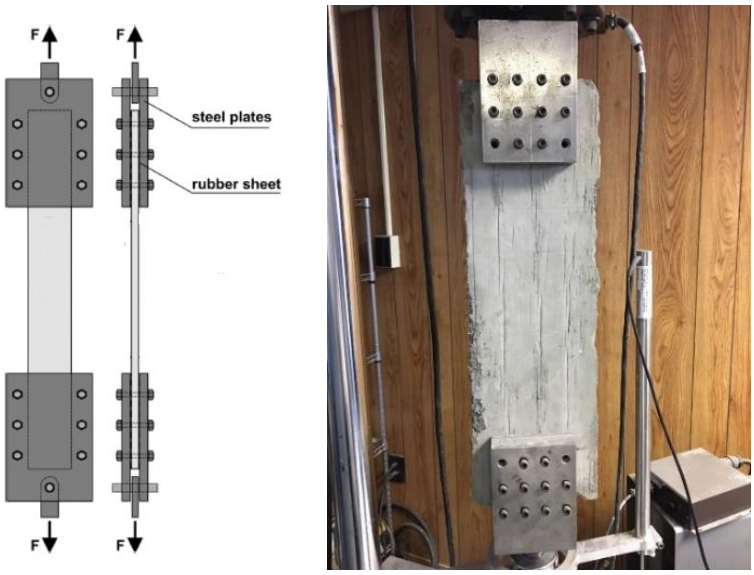

Figure 20. Tension test setup.

3.3.1.3 Flexure

The aerated slurry-infiltrated chicken mesh sheets tested in flexural had the same dimensions as the tension test specimens. They were subjected to four-point flexure loading over a span of 450 mm **Figure 21.**, Load was applied quasi-statically (with a constant displacement rate of 0.033 mm/s), and load-deflection data were collected during the flexure test up to failure.

Figure 21. Flexure test setup.

3.4 Test Results and Discussion

3.4.1 Compressive strength and bulk density of aerated slurry

The aerated slurry mix designs, defined by the foaming agent dosage (expressed as wt.% of cement) and water/cement ratio, and the corresponding measured values of 7-day compressive strength and bulk density are presented and **Figure 22**. Lower values of bulk density tend to correspond with lower compressive strength values. This is both because of the rise in air content and also the increase in water/cement ratio at higher dosages of foaming agent for achieving viable fresh mix rheology. Mix #13 with density of 0.9 g/cm^3 and compressive strength of 5.4 MPa at 7 days provides a viable balance of bulk density and strength for the targeted application. When compared with non-aerated slurry, it can be noted that aeration of slurry (Mix #13) produced 61% drop in bulk density and 90% drop in compressive strength. It should also be noted that increasing water/cement ratio does no necessarily reduces the compressive strength of the aerated slurry. Up to a certain limit, higher water/cement ratios can improve the homogeneity of foam distribution within the aerated slurry, and thus benefit its compressive strength. This work emphasized reduction of density in order to limit seismic forces (Guo, Juan et al. 2011, Ohsaki, Miyamura et al. 2016) and also allow for manual installation of the building

structural components. It was hypothesized that the presence of closely spaced chicken mesh wires with high specific surface area would benefit the compressive strength of aerated slurry-infiltrated chicken mesh.

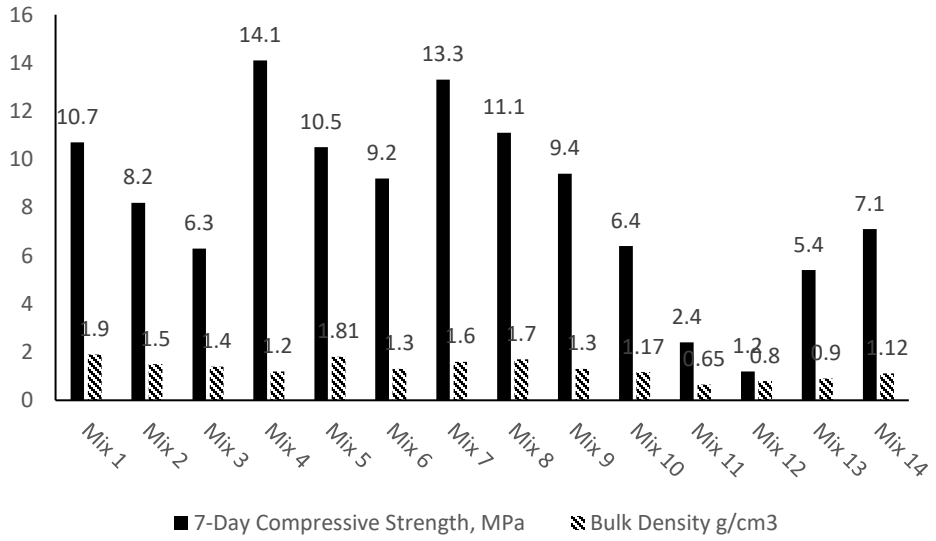

Figure 22. Compressive strength and bulk density test results for different aerated slurries.

3.4.2 Compressive behavior of the aerated slurry-infiltrated chicken mesh

A typical compressive stress-deflection curve for an aerated slurry-infiltrated chicken mesh prepared with the aerated slurry Mix #13 is presented in **Figure 23.** The presence of chicken mesh significantly improved the compressive strength and ductility of the aerated slurry. The aerated slurry alone provided a compressive strength of 5.4 MPa. In the presence of chicken mesh, a strain-hardening behavior was observed after this strength levels was reached. The ultimate strength was more than 15 MPa, noting that the specimen was unloaded after the maximum deflection limit of the test system was reached at about 70 mm. One can attribute the observed strain-hardening behavior (and the corresponding rise in compressive strength) of the

aerated slurry-infiltrated chicken mesh partly to the confining effect rendered by the wire mesh with closely spaced wires of high specific surface area.

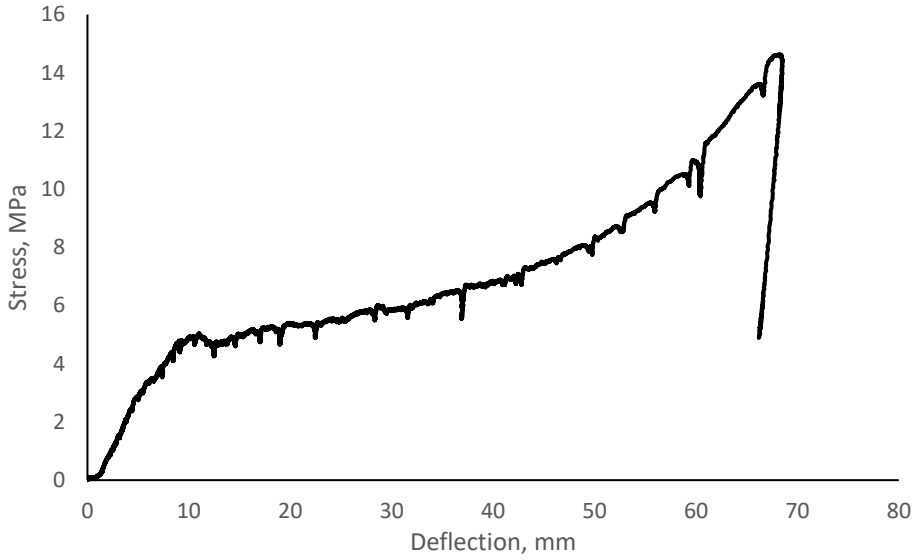

Figure 23. A typical compressive stress-deflection behavior of aerated slurry-infiltrated chicken mesh.

3.4.3 Tensile behavior of aerated slurry-infiltrated chicken mesh

The three slurries considered in this experimental program provided bulk densities (after hardening and air-drying) of: (1) 2.2 g/cm^3; (2) 1.3 g/cm^3; and (3) 0.8 g/cm^3. The highest density of 2.2 g/cm^3 was obtained without aeration of slurry. The tensile load-deflection curves obtained with 18 layers of chicken infiltrated with aerated (or non-aerated) slurry (producing a sheet of 25 mm thickness) are presented in **Figure 24**. together with the load-deflection curve for 18 layers of chicken mesh obtained without slurry-infiltration. The misaligned configuration of chicken mesh wires make it significantly compromises its stiffness and thus its merits as a tensile load-bearing system. The tendency towards realignment of chicken mesh wires at small deflections seriously undermine its structural stiffness. Infiltration with slurry (including aerated slurry), on the other hand, resists this tendency towards realignment of wires, and thus enables mobilization

of the tensile load-carrying capacity of the chicken mesh wires at relatively small displacements. Aeration of the slurry to reduce its bulk density does not significantly undermine its ability to mobilize the chicken mesh wires at small displacements to resist tensile forces. In short, chicken mesh and aerated slurry exhibit synergistic effects in the context of aerated slurry-infiltrated chicken mesh. The confining effects of chicken mesh increases the compressive strength of aerated slurry by more than 200%. Infiltration of chicken mesh with slurry also enables effects use of the tensile load-carrying capacity of the chicken mesh wires at structurally viable deformation levels.

Reduction of the slurry density via aeration from 2.2 to 0.8 g/cm^3 (by 63%) lowered the tensile strength of aerated slurry infiltrated chicken mesh from 5.4 to 4.2 MPa (by only 22%), as shown in **Figure 25.** This finding point at the potential of the aerated slurry-infiltrated chicken mesh to provide a desired balance of low bulk density and relatively high tensile strength. The tensile stiffness of slurry-infiltrated chicken mesh was not reduced significantly upon aeration for lowering its bulk density.

Figure 26. shows a tensile specimen of aerated slurry-infiltrated chicken mesh after failure in tension. A distributed damage zone was observed where the tendency towards realignment of chicken mesh wires, that was resisted by the aerated slurry surrounding the wires, led to crushing of the aerated slurry at large deformations.

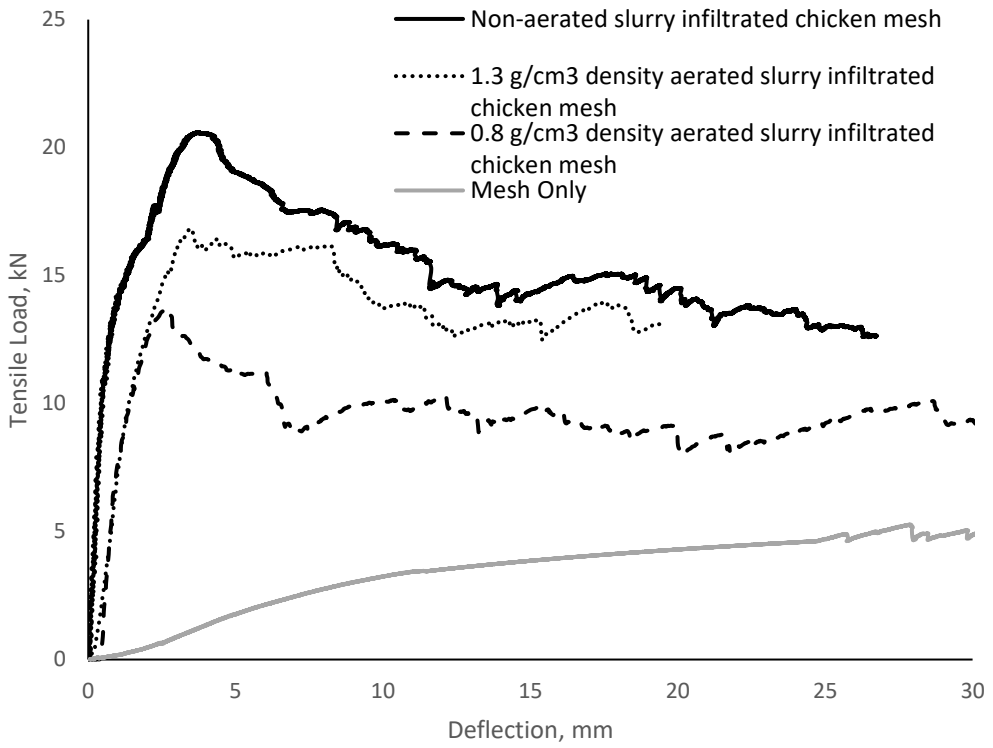

Figure 24. A typical compressive stress-deflection behavior of aerated slurry-infiltrated chicken mesh.

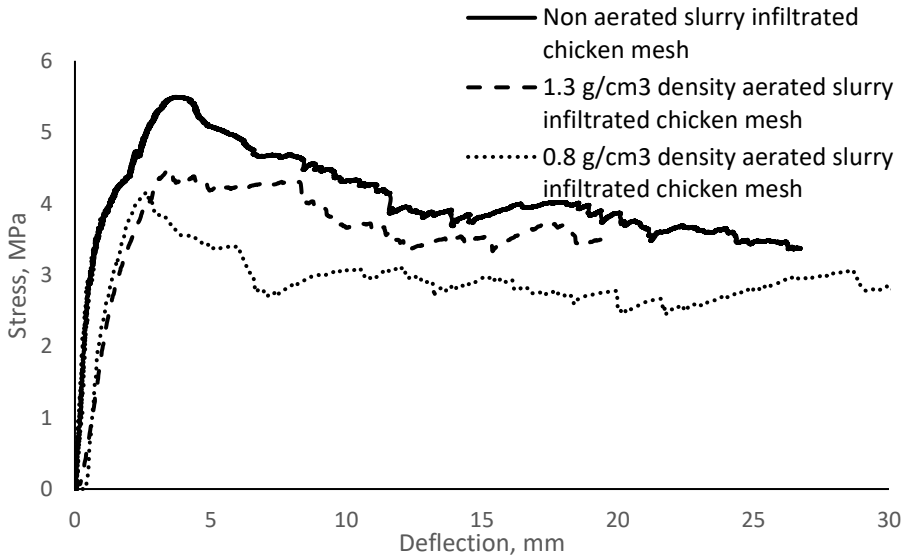

Figure 25. Tensile stress-deflection curves for non-aerated and aerated slurry-infiltrated chicken mesh.

Figure 26. Typical appearance of a failed tension test specimen of aerated slurry-infiltrated chicken mesh at relatively large tensile deformations.

The tensile strengths obtained for the slurry-infiltrated chicken mesh sheets presented above are summarized in **Table 5**. While the slurry density and the number of chicken mesh layers influence the tensile strength of aerated slurry-infiltrated chicken mesh sheets (with high concentration of chicken mesh), all these tensile strengths (except when 6 or 9 layers of chicken mesh are used) occur within a relatively narrow 3.64 – 4.40 MPa range. Significant reduction of bulk density could be obtained via aeration of the slurry without significant loss of the slurry-infiltrated chicken mesh tensile strength. These observations point at the potential of aerated slurry-infiltrated chicken mesh to provide a desired balance of tensile strength and bulk density.

Table 5. A summary presentation of the tensile strength test results for slurry-infiltrated chicken mesh sheets with different slurry densities and number of chicken mesh layers.

Slurry	Chicken Mesh Layers	Saponin/Cement (weight ratio)	Water/Cement (weight ratio)	Bulk Density (g/cm^3)
Non-Aerated	18/24	-	0.36 (0.004) superplasticizer)	2.2
Aerated	16/18	0.0002	0.5	1.3
Aerated	6/9/12/18	0.0005	0.6	0.8

3.4.4 Flexural performance

The three slurries considered in this experimental program provided bulk densities (after hardening and air-drying) of: (1) 2.2 g/cm^3; (2) 1.3 g/cm^3; and (3) 0.8 g/cm^3. The highest density of 2.2 g/cm^3 was obtained without aeration of slurry. Typical flexural stress-deflection curves for sheets of 25 mm thickness made with non-aerated and aerated slurries using 18 layers of chicken mesh are presented in **Figure 27.** The flexural behavior is observed to be ductile. Aeration of slurry lowered the flexural strength but not the ductility of the aerated slurry-infiltrated chicken mesh. Increasing the dosage of foaming agent to reduce the bulk density of the aerated slurry from 1.3 to 0.8 g/cm^3 had relatively small effects on the flexural performance of the resultant sheets. The peak flexural stress obtained with aerated slurry of 0.8 g/cm^3 bulk density was 6.9 MPa. Reduction of the aerated slurry density from 1.3 to 0.8 (by 38%) led to a reduction of the flexural stress from 7.8 MPa to 6.9 MPa (by 11%).

The flexure test specimens prepared with non-aerated slurry exhibited multiple cracking and a distributed flexural failure mode (**Figure 28a**.); flexural failure of the aerated specimens was less distributed (**Figure 28b.**).

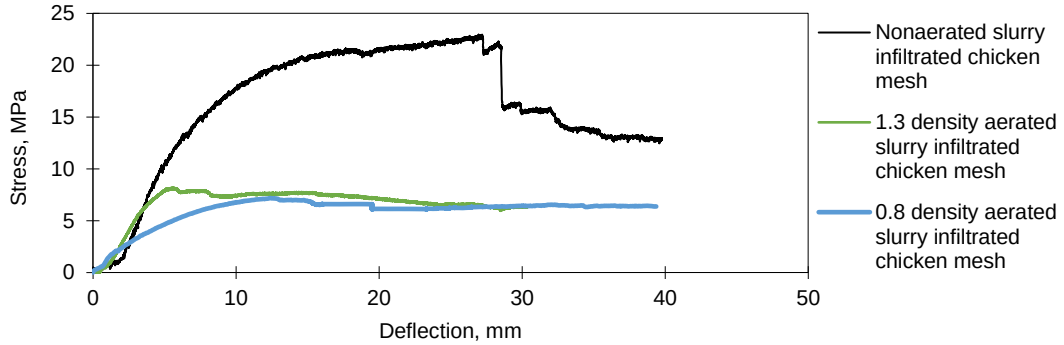

Figure 27. Flexure stress-deflection curves for non-aerated and aerated slurry-infiltrated chicken mesh sheets.

(a) Non-aerated slurry (b) Aerated slurry

Figure 28. Flexural failure modes of non-aerated and aerated slurry-infiltrated chicken mesh sheets.

3.4.5 Analysis of aerated slurry-infiltrated chicken mesh

The aerated slurry makes significant indirect contributions toward tensile strength by restraining the chicken mesh wires (which are partly oriented at an angle with respect to the tensile stress) from reorientation under tensile stress. The tensile strength of aerated slurry-infiltrated chicken mesh was expressed as follows:

$$\sigma_T = \alpha \rho f_y$$

where, σ_T = tensile strength of the aerated slurry infiltrated chicken mesh, ρ = area ratio of the chicken mesh wires, f_y = yield stress of the chicken mesh wires (310 MPa), and α = an empirical efficiency factor which reflects the degree of restraint offered by the aerated slurry against reorientation of the chicken mesh layers as well as the orientations of wires with respect to the tensile stress direction. An average value of α = 0.26 allows for prediction of the experimental values of tensile strength using the above equation.

In compression, one should account for the direct contribution of the chicken mesh wires (embedded in the aerated slurry matrix), and also their indirect confining effect which raises the effective compressive strength of the slurry. Considering these contributions of chicken mesh,

the composite compressive strength of aerated slurry-infiltrated chicken mesh may be expressed as follows:

$$\sigma_C = \beta\rho f_y + \gamma f_c'$$

where, σ_c = compressive strength of the aerated slurry-infiltrated chicken mesh, β = efficiency factor for the chicken mesh reinforcement in compression (it was assumed to be similar to the empirically derived efficiency factor of chicken mesh in tension, that is 0.26), and γ = efficiency factor of the aerated slurry in compression, which benefits from the confining effect of the chicken mesh reinforcement. A γ value of 4.6 allowed the above equation to predict the compression test results performed on aerated slurry-infiltrated chicken mesh. In other words, the aerated slurry that benefits from the beneficial effects of chicken mesh provides 4.6 times the compressive strength of plain aerated slurry. These relatively large beneficial effects can be attributed to: (i) the relatively low elastic modulus and high Poisson's ratio of the aerated slurry that produce relatively large strains in compression which, are restrained by the chicken mesh reinforcement of high elastic modulus and specific surface area with closely spaced wires, resulting in confining effects which raise the aerated slurry compressive strength; (ii) chicken mesh with high specific surface area and close wire spacing effectively reinforces the aerated slurry against the microcrack formation under restrained shrinkage, and the growth of these microcracks under load. The rise in compressive strength of aerated slurry with chicken mesh reinforcement is a significant factor enabling the otherwise non-structural (insulating) aerated slurry to make contributions to the aerated slurry-infiltrated chicken mesh structural performance.

Using concepts similar to those used with reinforced concrete, the nominal flexural strength (M_n) of an aerated slurry-infiltrated chicken mesh cross-section (**Figure 29**.) can be expressed as follows:

$$M_n = \alpha\rho f_y b(h-a)(\frac{h}{2})$$

where, 'a' is a value related to (and somewhat smaller than) the depth of neutral axis (c), and b and h are, respectively, the width and height of a rectangular cross-section. Similar to the approach to reinforced concrete flexural analysis, a constant compressive stress is assumed up to depth 'a' in order to simulate the nonlinear compressive stress distribution up to the depth neutral axis depth of 'c'. The value of 'a' can be derived based on the equilibrium of the tensile and compressive forces generated at the section under bending moment:

$$\alpha\rho f_y(h-a) = \left(\beta\rho f_y + \gamma f_c'\right)a$$

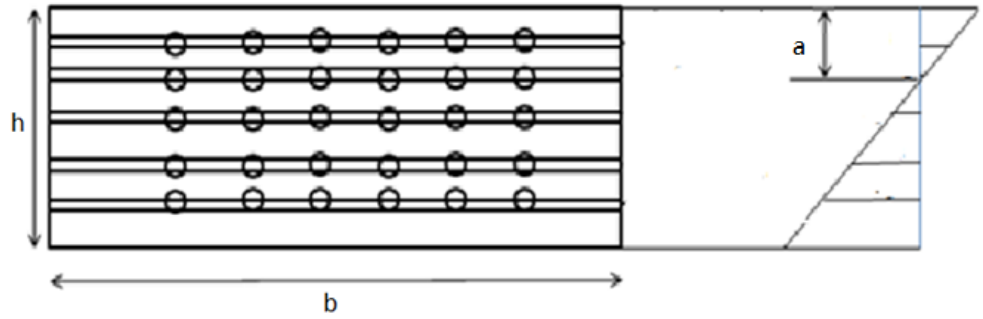

Figure 29. Cross-section and flexural strain distribution of an aerated slurry infiltrated chicken mesh rectangular section.

As a first step, the expression derived above for the nominal flexural strength of aerated slurry-infiltrated chicken mesh was verified using the experimental data generated for a beam and two sheets made with aerated slurry-infiltrated chicken mesh. These structural test specimens were made with a slurry proportioned at saponin: water: cement weight ratios of 0.00045: 0.6: 1 (which yielded a bulk specific gravity of 0.8 after hardening and air-drying).

Table 6. presents the aerated slurry-infiltrated chicken mesh sheet dimensions, reinforcement conditions, test results, and the experimental and theoretical values of flexural strength. The theoretical values of flexural strength obtained with the expression presented above are observed to be less than experimental values by only 3 to 5%. The approach outlined above for calculation of the nominal flexural strength of aerated slurry-infiltrated chicken mesh sheets and beams thus yielded favorable accuracy based on the limited test data generated in this investigation.

Table 6. Aerated slurry-infiltrated chicken mesh sheet and beam dimensions, reinforcement and loading conditions, and test results versus predicted values.

Specimen	# of Chicken Mesh Layers	Span, mm	Width, mm	Thickness, mm	Reinf. Area Ratio	Density, g/cm^3	Peak Load, N	3 or 4 Point Loading	Flexural Strength, N.m	
									Test	Theory
Sheet	12	450	150	20	0.04	0.8	1300	4	97.5	92.67
Sheet	18	450	150	25	0.03	0.8	2500	4	180.5	170.41
Beam	30	800	102	254	0.02	0.8	25000	3	5000	4910.248

3.5 Conclusions

1. The tensile behavior of aerated slurry-infiltrated chicken mesh relies upon the support provided by the aerated slurry against realignment of the chicken mesh wires. This interaction depends upon the quality (bearing capacity, elastic modulus and compressive strength) of the aerated slurry, and the concentration of chicken mesh as well as the specific surface area and the spacing of chicken mesh wires.

2. Slurry-infiltrated chicken mesh sheets exhibit a ductile behavior in tension. The transition from non-aerated slurry to aerated slurries of lower densities produces some drop in tensile strength, but not in the ductile tensile load-deflection behavior. The tensile load-carrying capacity of aerated slurry-infiltrated chicken mesh does not increase proportionally with the increasing

number of chicken mesh layers for the same sheet thickness. This is due to the interaction between the chicken mesh with the aerated slurry governs the ability to mobilize the chicken mesh load-bearing capacity within structurally viable ranges of deformation.

3. The aerated slurry-infiltrated chicken mesh sheets exhibit a distributed failure mode marked by crushing of the aerated slurry over a major fraction of the sheet volume. The crushing of aerated slurry under tension highlights the demand imposed by the tendency towards realignment of the chicken mesh wires under tension on the bearing and compressive qualities of the aerated slurry.

4. The flexural load-deformation behavior of the aerated slurry-infiltrated chicken mesh sheets was found to exhibit qualitative similarities with their tensile behavior. The observations summarized above for tensile behavior also applies to flexural behavior.

5. The flexural failure mode of aerated slurry-infiltrated chicken mesh sheets is dominated by a single crack, and does not exhibit the distributed failure mode observed in tension. In spite of this, the flexural failure is still highly ductile. In the case of the selected aerated slurry with 0.8 g/cm^3 density, aerated slurry-infiltrated chicken mesh sheets with about 20 mm thickness would require about 12 layers of chicken mesh in order to reach viable levels of flexural strength.

3.6 Acknowledgements

The work reported herein was funded by the U.S. Army Corps of Engineers Grant No. 9132T-16-C-0003 U.S. Army – United States.

REFERENCES

REFERENCES

Aboul-Anen, B., A. El-Shafey, and M. El-Shami, Experimental and analytical model of ferrocement slabs. International Journal of Recent Trends in Engineering, 2009. 1(6): p. 25-29.

Ahmad Zaidi, A.M. and Q.M. Li, Investigation on penetration resistance of foamed concrete. Proceedings of the Institution of Civil Engineers: Structures and Buildings, 2009. 162(1): p. 77-85.

Ahmad, I. and N. Mohamad, Structural behavior of precast lightweight concrete sandwich panel under eccentric load: an overview.

Ahmad, I., et al., Structural Behavior of Precast Lightweight Foamed Concrete Sandwich panel (PLFP) with Double Shear Truss Connectors under Eccentric Load: Preliminary Result. Advanced Materials Research, 2013. 795: p. 414-418.

Ahmad, T., M. Arif, and A. Masood, Experimental Investigations on Ferrocement Roof Slab System for Low Cost Housing. Journal of The Institution of Engineers (India): Series A, 2014. 95(1): p. 9-18.

Almalkawi, A.T., et al., Behavior of a lightweight frame made with aerated slurry-infiltrated chicken mesh under cyclic lateral loading. Construction and Building Materials, 2018. 160: p. 679-686.

Almalkawi, A.T., S. Hamadna, and P. Soroushian, One-part alkali activated cement based volcanic pumice. Construction and Building Materials, 2017. 152: p. 367-374.

Basunbul, I.A., M. Saleem, and G.J. Al-Sulaimani, Flexural behavior of ferrocement sandwich panels. Cement and Concrete Composites, 1991. 13(1): p. 21-28.

Desayi, P. and V. Reddy, Strength of ligthweight ferrocement in flexure. Cement and Concrete Composites, 1991. 13(1): p. 13-20.

Guo, M., et al., Seismic performance experimental research for multi-ribbed composite wall strengthened with aerated concrete blocks. Journal of Sichuan University: Engineering Science Edition, 2011. 43(1): p. 51-57.

Hamad, A.J., Materials, Production, Properties and Application of Aerated Lightweight Concrete: Review. 2014.

Husein, N.R., V.C. Agarwal, and A. Rawat, An Experimental Study on Using Lightweight Web Sandwich Panel as a Floor and a Wall.

Joseph, J.D.R., J. Prabakar, and P. Alagusundaramoorthy, Precast concrete sandwich one-way slabs under flexural loading. Engineering Structures, 2017. 138: p. 447-457.

Liu, J., et al., Experimental and numerical study of reactive powder concrete reinforced with steel wire mesh against projectile penetration. International Journal of Impact Engineering, 2017.

Memon, N.A., S.R. Sumadi, and M. Ramli, Strength and Behaviour of Lightweight Ferrocement-Aerated Concrete Sandwich Blocks. Malaysian Journal of Civil Engineering, 2006. 18(2): p. 99-108.

Naaman, A.E., Ferrocement and laminated cementitious composites. Vol. 3000. 2000: Techno press.

Nambiar, E.K. and K. Ramamurthy, Air-void characterisation of foam concrete. Cement and concrete research, 2007. 37(2): p. 221-230.

Ohsaki, M., et al., Seismic Response Simulation of Building Structures, in High-Performance Computing for Structural Mechanics and Earthquake/Tsunami Engineering. 2016, Springer. p. 105-139.

Radin Sumadi, S. and M. Ramli, Development of lightweight ferrocement sandwich panels for modular housing and industralized building system. 2008.

Ramamurthy, K., E.K. Nambiar, and G.I.S. Ranjani, A classification of studies on properties of foam concrete. Cement and Concrete Composites, 2009. 31(6): p. 388-396.

Van Rooyen, A.S., Structural lightweight aerated concrete. 2013.

Wafa, M.A. and K. Fukuzawa, Characteristics of ferrocement thin composite elements using various reinforcement meshes in flexure. Journal of Reinforced Plastics and Composites, 2010. 29(23): p. 3530-3539.

Yerramala, A., C. Ramachandurdu, and V.B. Desai, Flexural strength of metakaolin ferrocement. Composites Part B-Engineering, 2013. 55: p. 176-183.

Zhang, Z., et al., Geopolymer foam concrete: an emerging material for sustainable construction. Construction and Building Materials, 2014. 56: p. 113-127.

CHAPTER 4: BEHAVIOR OF A LIGHTWEIGHT FRAME MADE WITH AERATED SLURRY-INFILTRATED CHICKEN MESH UNDER CYCLIC LATERAL LOADING

This chapter was first published as "Behavior of a lightweight frame made with aerated slurry-infiltrated chicken mesh under cyclic lateral loading." by Almalkawi, Areej T., Weisheng Hong, Sameer Hamadna, Parviz Soroushian, and Ghassan Al-Chaar. Construction and Building Materials 160 (2018): 679-686.

4.1 Introduction

Aerated concrete is traditionally viewed as an insulating (non-structural) building material. A primary premise of the work reported herein is that a reinforcement system with high specific surface area would enable use of aerated concrete in structural applications. The high specific surface area and the confining role of such reinforcement is hypothesized to benefit the structural performance of aerated concrete. Construction with reinforcement systems of high specific surface area would be challenged by the congestion of reinforcement which is not favorable to convenient placement and consolidation of aerated concrete. An aerated slurry of high flowability was used in this work to thoroughly penetrate the congested reinforcement system, facilitating thorough consolidation and desired interfacial interactions with the reinforcement. This work chose chicken mesh (hexagonal 20-gauge galvanized poultry netting) as a steel reinforcement system of high specific surface area due to its broad availability across the world.

Concrete structures generally rely on frames as the primary lateral load-resisting structural systems (Arroyo and Gutiérrez 2016, Abd-Elhamed and Mahmoud 2017, Ruiz-García

and Aguilar 2017). Reinforced concrete frames can be designed to provide high levels of ductility and (hysteretic) energy dissipation capacity for efficient resistance of seismic forces (He, Lam et al. 1998, Rose 1998, Kwon, Seo et al. 2017, Yun, Kim et al. 2017). Aerated slurry-infiltrated chicken mesh can, due to the high specific surface area of steel reinforcement, provide distinctly high levels of ductility and energy dissipation capacity. The work reported herein evaluated the structural performance of an aerated slurry-infiltrated chicken mesh from under cyclic lateral loads. The data generated on the ductility, hysteretic energy absorption capacity and the lateral load-bearing capacity of the frame, accompanied with structural analyses of the frame, provide insight into the merits of aerated slurry-infiltrated chicken mesh as a robust building materials for construction of seismic-resistant building systems.

There has been growing interest in the use of lightweight aerated concrete as building envelope material. The desired balance of thermal and sound insulation qualities, fire resistance, strength, durability, cost, and ease of installation and maintenance of this material favor its broader use in building construction. Memon et al. (Memon, Sumadi et al. 2007, Ng, Low et al. 2012) and Ng et al.(Ng, Low et al. 2012) have reported data on the mechanical performance of autoclaved aerated panels. Low et al.(Low, Ng et al. 2014) and Wakili et al.(Wakili, Hugi et al. 2015) investigated the thermal performance of these panels. Tanner et al. (Tanner, Varela et al. 2005) and Costa et al. (Costa, Penna et al. 2011) investigated the failure modes and seismic behavior of autoclaved aerated concrete walls. The use of these walls in conjunction with steel frames has also been investigated under cyclic loading (Zhenggang, Peng et al. 2017). The use of fiber reinforced polymer composites towards seismic rehabilitation of autoclaved aerated concrete columns subjected to cyclic loading has also been investigated (Cho, Kim et al. 2012).

The innovative aspect of the work reported herein relates to transformation of an insulating lightweight (aerated) concrete into a structural material through reinforcement with a wire (chicken) mesh reinforcement of high specific surface area. A highly flowable aerated slurry is used to facilitate infiltration of the chicken mesh reinforcement with the lightweight cementitious matrix.

4.2 Materials and Methods

4.2.1 Aerated Slurry

Aeration introduces a homogenous system of fine air bubbles into the cement paste. This is accomplished using foaming agents that stabilize the air voids generated via agitation of the mixing water of slurry that incorporates the foaming agent (Nambiar and Ramamurthy 2007, Ramamurthy, Nambiar et al. 2009, Zhang, Provis et al. 2014, Huang, Zhang et al. 2015). Preparation of the aerated slurry started with production of foamed water. For this purpose, a foaming agent extracted from plants (saponin) blended with the mixing water at 1200 rpm rotational speed, using a mixing blade attached to a drill (**Figure 30**.). The foamed mixing water was then added to cement at water/cement ratio of 0.5. Mixing was accomplished in a mortar mixer for 2 minutes.

Figure 30. Preparation of foamed water.

The aerated slurry used to infiltrate the chicken mesh comprised cement: water: saponin at 1: 0.5: 0.0006 weight ratios, with a bulk density in hardened state of 0.9 g/cm3. Based on trial and adjustment studies, it was found that an aerated slurry with viscosity of 1900.8 cp and yield stress of 68.2 is capable of infiltrating multiple layers of chicken mesh with the opening size considered in this investigation.

Cube specimens of plain aerated slurry with 50 mm dimensions were also prepared for performance of compression tests. The molded specimens were stored in sealed condition (>95% relative humidity) at room temperature) for 7 days, and then subjected to compression testing. The average compressive strength was measured at 5.01 MPa.

4.2.2 Chicken Mesh

The chicken mesh considered in this experimental program (**Figure 31**.) comprised wire gauge No. 20 (with 0.88 mm diameter, 0.608 mm^2 cross sectional areas) configured hexagonally with wire spacing of 25 mm. Chicken meshes are available with different wire diameter and spacing. Commonly available chicken meshes are made with wires of different diameters; the spacing of hexagonally configured wires are generally increased with increasing wire diameter in order to provide comparable wire cross-sectional areas per unit width. Given the relatively large layers of chicken mesh that need to be infiltrated with aerated slurry, the preference in this investigation was for chicken meshes with larger wire diameter and spacing. **Figure 32**. depicts the anisotropic structure of chicken mesh, which provides higher strength in the longitudinal direction and lower strength in the transverse direction.

Figure 31. The chicken mesh used in this experimental program.

.

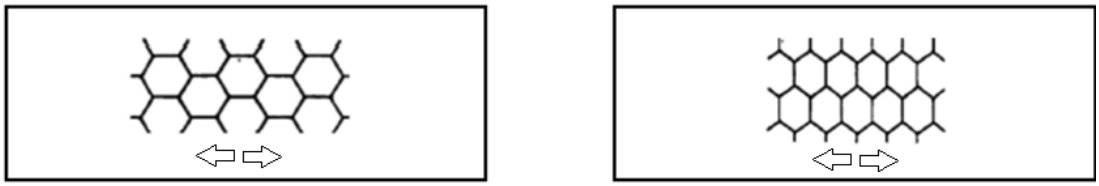

Figure 32. Chicken mesh orientations: longitudinal (left), and transverse (right).

4.2.3 Aerated Slurry-Infiltrated Chicken Mesh

Given the fine diameter of the chicken mesh wires, a relatively low volume fraction (e.g., 1%) of chicken mesh produces a relatively congested reinforcement system. As a result, cementitious materials with normal fresh mix rheology cannot be used in this application. The need to infiltrate multiple layers of chicken mesh led to the selection of a flowable slurry as the binder for use with chicken mesh reinforcement. Aerated slurry was used in this application to lower the density of structural materials for ease of installation and reduction of seismic forces. Aerated concrete is usually used as insulation and not in structural applications. It was hypothesized that the high specific surface area and the confining action of chicken mesh would enhance the mechanical performance of the resultant aerated slurry infiltrated chicken mesh to suit structural applications.

In chicken mesh, wires are oriented in different directions. Chicken mesh thus offers a high level of flexibility when subjected to tension, which is due to a tendency towards alignment of wires along the direction of tensile force. Their low stiffness excludes chicken mesh from

structural applications. When placed within a matrix (aerated slurry in this case), however, the wires in chicken mesh are restrained against realignment by the matrix. Depending on the extent of this restraint, the tensile force-resisting capacity of wires would be mobilized from the beginning. This raises the stiffness of chicken mesh, which could translate aerated slurry infiltrated chicken mesh into a structural building material. Semi-empirical equations were developed to express the tensile and compressive strengths of aerated slurry infiltrated chicken mesh, as described below.

4.2.4 Aerated Slurry Infiltrated Chicken Mesh Frame

The models presented earlier for predicting the flexural strength of aerated slurry infiltrated chicken mesh were verified using experimental results (Balaguru, Shah et al. 1977, Pankaj, Arif et al. 2002, Bedoya-Ruiz, Ortiz et al. 2014, Eskandari and Madadi 2015, Saleem and Ahmed 2015, Subramani and Anbuchezian 2017)

The tensile strength of aerated slurry infiltrated chicken mesh (σ_T) was expressed as follows:

$$\sigma_T = \alpha \rho f_y$$

where, ρ = area fraction of the chicken mesh wires (irrespective of their orientation) at a cross-section that is perpendicular to the tensile stress direction; f_y = yield stress of the chicken mesh wires (310 MPa); and α = an empirical efficiency factor which reflects the degree of restraint provided by the aerated slurry against realignment of wires (0.56 based on experimental results).

In compression, the composite behavior of aerated slurry infiltrated chicken mesh produces a compressive strength that can be expressed as follows:

$$\sigma_C = \beta \rho f_y + \gamma f_c'$$

where, σ_c = compressive strength; β = efficiency factor of chicken mesh reinforcement in compressive (it was assumed to be similar to the efficiency factor of chicken mesh in tension, that is 0.56); and γ = efficiency factor of aerated sully in compression, which was surprisingly found (in compression tests performed on an aerated slurry infiltrated chicken mesh) to be quite large (close to 5).

Using concepts similar to those used with reinforced concrete, the nominal flexural strength (M_n) of an aerated slurry-infiltrated chicken mesh cross-section (**Figure 33**.) can be expressed as follows:

$$M_n = \alpha\rho f_y b(h-a)(\frac{h}{2}) \quad 3$$

where, 'a' was assumed to be equal to the depth of neutral axis c, considering the highly ductile behavior of aerated slurry infiltrated chicken mesh. A constant compressive stress was assumed up to a depth 'a' in order to simulate the nonlinear compressive stress distribution. The value of 'a' can be derived based on the equilibrium of tensile and compressive forces generated at the section subjected to bending moment:

$$\alpha\rho f_y(h-a) = \left(\beta\rho f_y + \gamma f_c'\right)a \quad 4$$

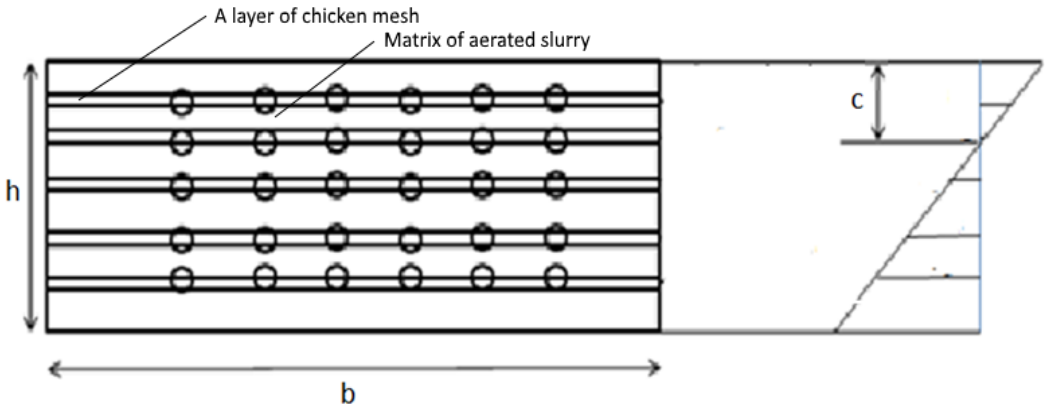

Figure 33. Cross-section and flexural strain distribution of aerated slurry infiltrated chicken mesh.

An aerated slurry infiltrated chicken mesh frame with 1.75 m height and 1.4 m width was designed to withstand a concentrated in-plane load of 8 KN applied at its top. The maximum bending moment under this loading condition is: M= F_t.h /2 = 7,000 N.m. The cross-section designed to resist this bending moment had 10 cm width and 25 cm height, reinforced with 30 layers of chicken mesh (with the chicken mesh layers oriented longitudinally along the element axis). The area fraction of longitudinally oriented chicken mesh layers at cross-sections is 1.6%. The resultant tensile and compressive strengths of the aerated slurry-infiltrated chicken mesh would be:

$\sigma_T = \alpha\rho f_y = 0.56x0.016x310 = 2.75\ MPa$

$\sigma_C = \beta\rho f_y + \gamma f_c'$ = 0.56x0.016x310 + 5x2.5 = 27.604 MPa

Equilibrium of tensile and compressive forces can be used to calculate the value of 'a' (assumed to be equal to the depth of neutral axis "c" in **Figure 33**.) required for calculating the nominal flexural strength:

$$\sigma_C . a = \sigma_T . (h - a)$$

27.604 xa = 2.75x (250-a)

a = 22.65 mm

The flexural strength of the aerated slurry infiltrated chicken mesh can now be calculated as:

$M_n = \alpha\rho f_y b(h-a)(\frac{h}{2})$ = 0.56x0.016x310x100x(250-22.65)x(250/2) = 7893.59 N.m

The nominal bending moment flexural strength of 7893.59 N.m exceeds the required flexural strength of 7,000 N.m by 8%.

Figure 34a. shows the formwork with chicken mesh reinforcement placed in it. The slurry was simply poured onto the chicken mesh (**Figure 34**.) to infiltrate the preplaced chicken mesh layers. After pouring of slurry, the frame was covered with plastic sheet to mitigate moisture loss. This allowed for curing at >95% relative humidity, that was achieved using the vapor released from the slurry during curing. The frame was cured at ambient temperature for 14 days.

(a) Formwork with preplaced chicken mesh (b) Infiltration of chicken mesh with aerated slurry

Figure 34. Construction of the aerated slurry-infiltrated chicken mesh frame.

4.2.5 Cyclic Testing

The frame behavior was evaluated under quasi-static cyclic lateral loading. The test procedure involved application of reversed load cycles of progressively increasing lateral displacements until the first major event (FME), defined here as yielding, occurred. Three reversed cycles of progressively increasing displacement amplitude were applied before the FME was reached. Subsequent loading followed the Sequential Phase Displacement (SPD) procedure which involves application of degradation and stabilization cycles at a constant displacement amplitude before progressing to the next phase with a greater displacement. The first cycle in a phase is applied with a larger displacement and is proceeded by three degradation cycles; subsequent application of three stabilization cycles completes the phase. Stabilized response is achieved when the decrease in resistance between two successive stabilization cycles is less than

5% (Soudki, West et al. 1996). If the decrease in resistance is more than 5%, additional stabilization cycles should be conducted. The frame tested in this study stabilized in five cycles. The procedure then moves on to the next phase (Salenikovich, Dolan et al. 1999, Gatto and Uang 2003, Ibarra, Medina et al. 2005).

Cyclic testing of the frame was performed in accordance with ASTM E2126 Method A, that closely follows the SPD procedure developed by TCCMAR (Porter 1987) with few modifications. The SPD procedure is based solely on the First Major Event (FME), where FME is defined as the displacement at which the structure starts to deform inelastically (anticipated yield displacement) (Krawinkler 2009). ASTM E2126, on the other hand, takes into account both FME and ductility ratio when determining the initial amplitude of each phase in the test protocol. In general, the SPD protocol is displacement-controlled, and involves triangular reversed cycles at increasing displacement levels. The displacement increase in ASTM E2126 is based on FME and ductility ratio. The SPD procedure begins with at least three incremental levels of three cycles each, within the elastic displacement region up to the First Major Event (FME). The SPD method recommends 200% of the FME as the displacement increment for each phase in the case of ductile systems (Salenikovich, Dolan et al. 1999, Gatto and Uang 2003).

The test protocol devised here, based on ASTM E2126 requirement comprised 15 steps of displacement increase, with trailing cycles after each peak cycle as shown **Table 7.**

Table 7. Test protocol for evaluation of the frame performance under cyclic lateral loads.

Load step	Drift	Peak Displacement, cm	Trailing Cycle Displ.	# of trailing cycles
1	0.050%	0.048	0.048	5
2	0.075%	0.072	0.054	6
3	0.100%	0.096	0.072	6
4	0.20%	0.192	0.144	3
5	0.3%	0.288	0.216	3
6	0.4%	0.384	0.288	3
7	0.7%	0.672	0.504	2
8	1.00%	0.960	0.720	2
9	1.50%	1.440	1.080	2
10	2.00%	1.920	1.440	2
11	2.50%	2.400	1.800	2
12	3.00%	2.880	2.160	2
13	4.00%	3.840	2.880	2
14	4.50%	4.320	3.240	2
15	5.00%	4.800	3.600	2

The column bases were fixed in an aerated slurry-infiltrated chicken mesh footing and installed on a reaction frame (**Figure 35**.) for in-plane lateral cyclic loading per ASTM E564. A load cell and a displacement transducer were used to collect the load and displacement data, using a data acquisition system, under cyclic lateral loads.

Figure 35. The test setup used for performance of cyclic tests on the aerated slurry-infiltrated chicken mesh frame.

4.3 Test Results and Discussion

4.3.1 Plastic-Hinge approach

The frame failed by plastic hinge formation in the beam, as expected from the strong column-weak beam approach adopted for seismic design of the frame. **Figure 36.** shows the plastic hinge formation in beam near the beam-column joint under repeated load cycles. The top part of the plastic hinge exhibited multiple cracking, while one crack formed at the bottom, which widened and connected to top cracks under cyclic deformations of growing amplitudes.

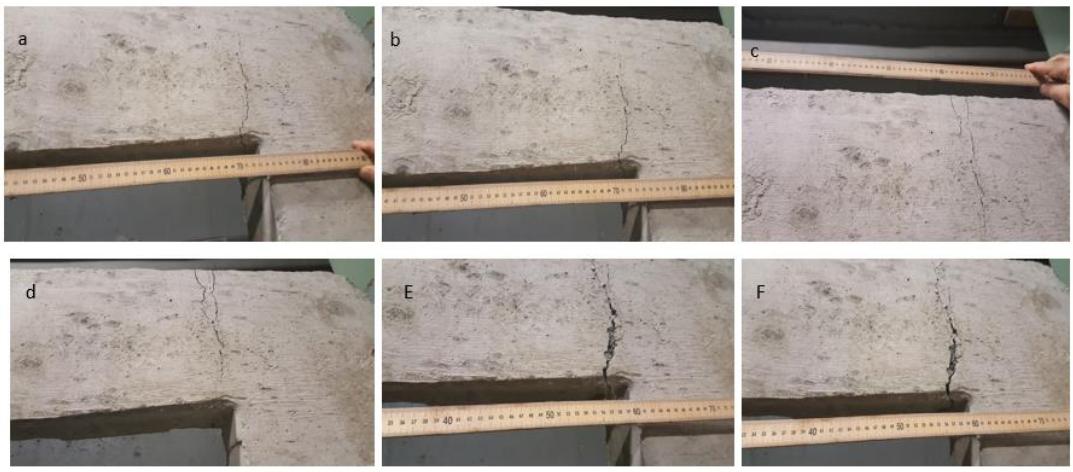

Figure 36. Plastic hinge formation in beam near the beam-column joint under reversed cycling testing with growing displacement amplitudes.

4.3.2 Hysteretic load-deflection curve

The cyclic load-deflection curve produced for the frame is presented in **Figure 37**. together with the initial envelope (connecting the initial peak loads at the initial load achieved for each displacement) as well as the stabilized envelope (connecting the stabilized peak loads after repeated cycles at each deformation) (Dolan and Heine 1997). The displacement cycles were unsymmetrical; this was forced by the size constraints of the reaction frame used in this test. The space available on one side of the frame was too small to allow for application of

symmetric cyclic deformations. **Figure 38a**. and **Figure 38b.** shows the average initial and stabilized envelopes, respectively, obtained by averaging the corresponding envelope curves produced in opposite displacement directions (Dolan and Johnson 1996, Dolan and Heine 1997). **Figure 37**. and **Figure 38**. are indicative of a ductile behavior with desired hysteretic energy absorption capacity. These observations support the effectiveness of chicken mesh as a distributed reinforcement of high specific surface area in enhancing the toughness and energy dissipation capacity of the cementitious matrix.

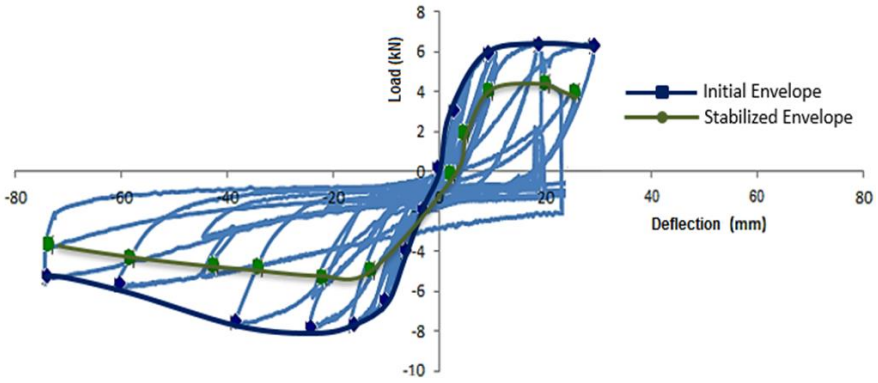

Figure 37. The hysteretic response, and the initial and stabilized envelopes of the frame subjected to cyclic loading per SPD (ASTM E2126) test method.

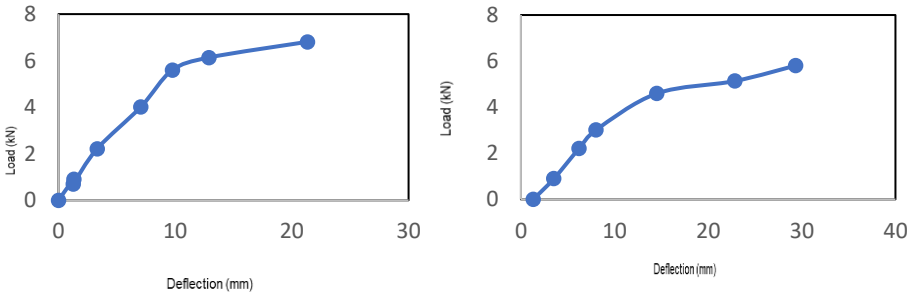

(b) Stabilized envelope (a) Initial envelope

Figure 38. Averaged initial and stabilized envelope curves of the aerated slurry-infiltrated chicken mesh frame.

A comparative study was made of the behavior of the aerated slurry-infiltrated chicken mesh frame versus lateral load-carrying system of similar geometric attributes comprising either oriented strandboard (OSB) or hardwood subjected to comparable cyclic lateral loads (Toothman 2003). **Figure 39**. shows the average initial envelopes of these systems. The aerated slurry-infiltrated chicken mesh frame is observed to provide ductility levels comparable to those of lateral load-carrying systems based on OSB and hardwood. The peak load-carrying capacity of the frame is more than those of systems based on OSB and hardwood; such comparisons, however, should also account for the weight of different systems.

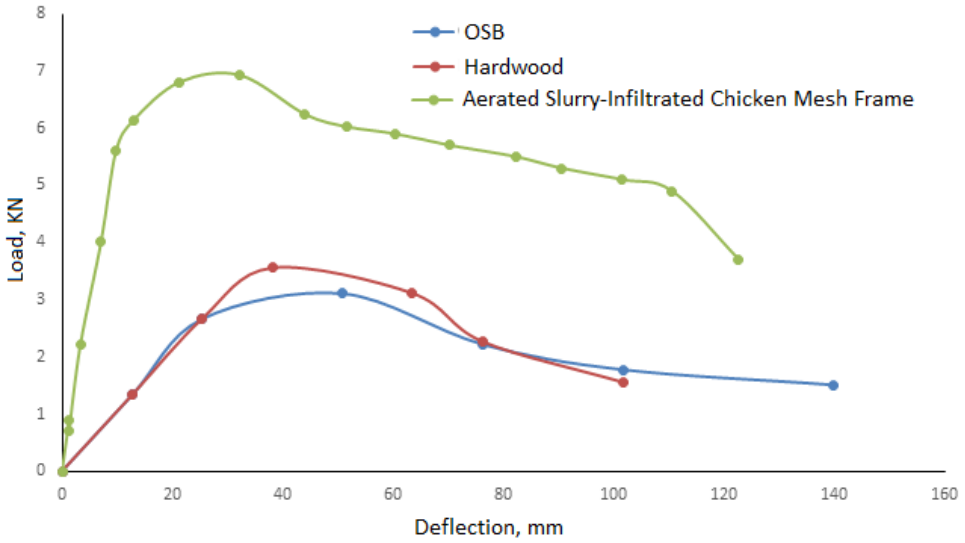

Figure 39. Averaged initial envelope curves of the aerated slurry-infiltrated chicken mesh frame versus those of lateral load-carrying systems based on OSB and hardwood.

4.3.3 Equivalent Energy Elastic Plastic (EEEP) curve

The envelope curves introduced above can be used, following the ASTM E2126 procedures, to derive the Equivalent Energy Elastic Plastic (EEEP) curve that represents an elasto-plastic interpretation of the aerated slurry-infiltrated chicken mesh behavior. The EEEP curve encompasses the same order of magnitude area as the actual load-displacement curve (form the origin to the ultimate displacement). This area is a measure of the toughness of the system.

Toughness is defined here as the energy required to fail the structural system. The EEP curve shown in **Figure 40**. incorporates a yield force(P_{yield}) and the corresponding displacement (Δ_{yield}), the failure displacement (Δ_u), the area under the load-displacement curve, and the elastic stiffness of the structural system.

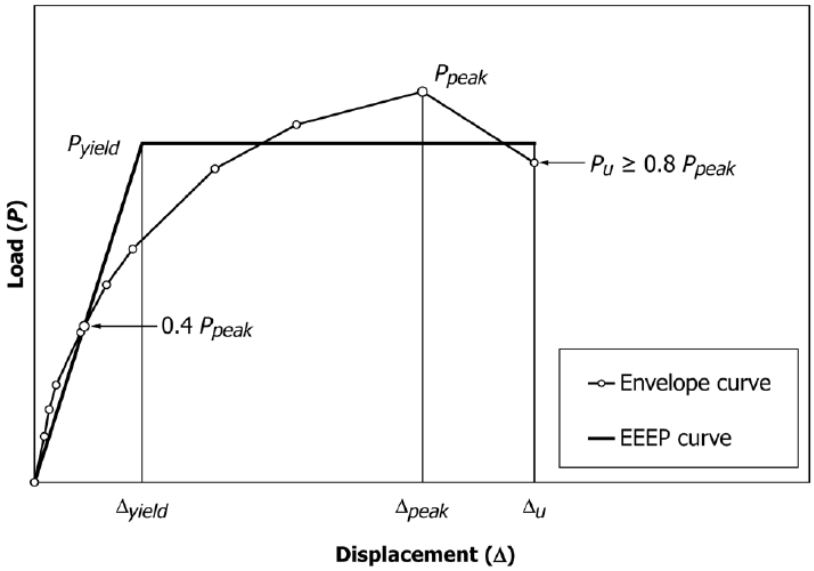

Figure 40. Definition of EEEP curve (ASTM E2126).

4.3.4 Elastic Stiffness

Figure 41. shows the averaged initial and stabilized envelope curves of the slurry-infiltrated chicken mesh frame, and also the EEEP curve corresponding to the initial envelope curve. Elastic stiffness, k_e, can be determined as the slope of the secant passing through the origin and the point on the load-displacement curve (or envelope curve) that is equal to 40% of the peak load, F_{peak}. The slope of this line is used to locate the elastic portion of the EEEP curve. In addition, it is used to find other parameters such as the yield load, yield displacement, and the ductility ratio.(Kesner, Billington et al. 2003)

$$\text{Elastic Stiffness} = k_e = \frac{0.4F_{Peak}}{\Delta_{0.4Fpeak}} \quad (5)$$

Elastic stiffness is a good indicator of the stiffness that a frame would exhibit when subjected to low to moderate displacements (Salenikovich 2000). The elastic stiffness obtained using the initial envelope curve for the aerated slurry-infiltrated chicken mesh following the above procedure is shown in **Figure 42**. and compared with later load resisting systems of comparable geometry made with OSB or hardwood sheeting. The elastic stiffness of the aerated slurry-infiltrated chicken mesh is observed to be higher than those provided by alternative lateral load resisting systems

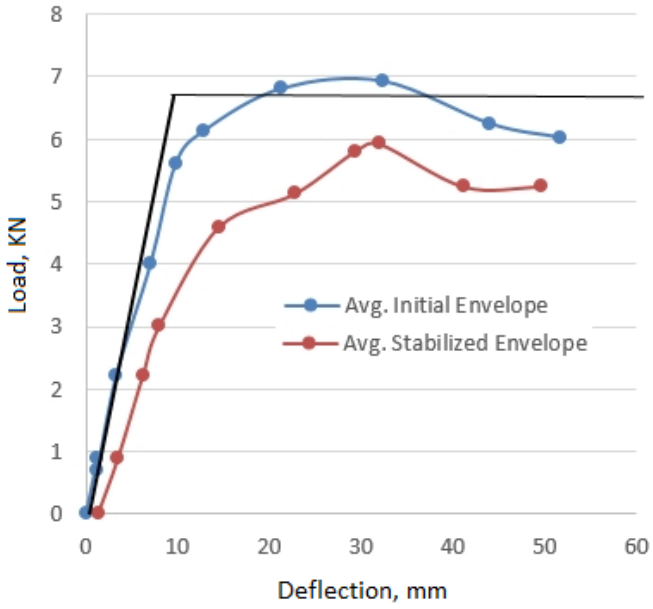

Figure 41. The initial and stabilized envelope curves of the aerated slurry-infiltrated chicken mesh frame, and the EEEP curve corresponding to the initial envelope.

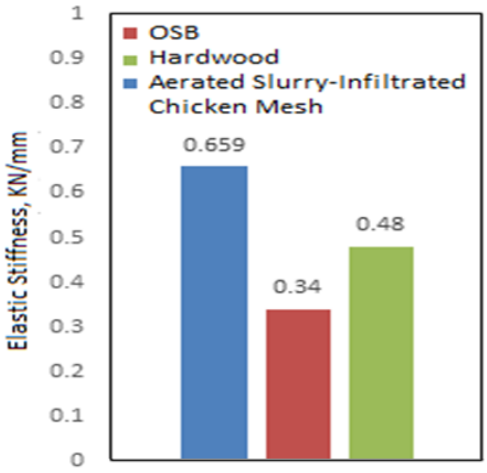

Figure 42. Elastic stiffness of different sheathing materials.

4.3.5 Failure load

Following the ASTM E2126 procedures, failure load was calculated as 80% of the peak load. Displacement at failure is another key parameter in assessing the seismic resistance of a lateral load-carrying system. The ability of a structure to dissipate energy arises partly from its ability to deform without failing (Park 1989, Salonikios, Kappos et al. 2000). **Table 8**. compares the failure load and the displacement at failure of the aerated slurry-infiltrated chicken mesh frame versus alternative lateral load-resisting systems with comparable geometry which are made with oriented strandboard (OSB) and hardwood sheathing. The aerated slurry-infiltrated chicken mesh frame is observed to provide a relatively high failure load but lower displacement at failure when compared with the alternative systems. A review of the initial envelopes of these systems (see **Figure 41.**, however, indicates that the overall ductility of the three systems is comparable, and the relatively low displacement at failure of the aerated slurry-infiltrated chicken mesh frame is a result of the approach taken by ASMT E2126 to define this displacement.

Table 8. Failure load and displacement at failure of aerated slurry-infiltrated chicken mesh frame versus alternative lateral load-carrying systems of comparable geometric attributes.

Lateral Load-Carrying System	Failure Load, kN	Displacement at Failure, mm
Aerated slurry w/chicken mesh	5.54	32.26
OSB	3.11	83.0
Hardboard	3.29	76.0

4.3.6 Yield load and yield displacement

Yield load is determined based on an approximation of the first major event, which is the theoretical load and displacement at which the structure starts to deform inelastically. For the area under the load-displacement curve and the EEEP curve to be equal, the value of F_{yield} is found where the area of the load-displacement curve equals the area of the EEEP curve . The area under the load-displacement curve (A) can be computed by integrating the initial envelope curve between x=0 to x=32.6 mm (the failure displacement as presented in **Table 9**.

$$F_{yield} = \frac{-\Delta_u \pm \sqrt{\Delta_u^2 - \frac{2A}{k_e}}}{\frac{-1}{k_e}} \qquad 6$$

where F_{yield}= Yield Load (Kip, KN), A = the area (kip.in, KN.mm) under the load-displacement curve from the origin to the failure displacement ($\Delta_{failure}$), and k_e = elastic Stiffness (kip/in, kN/mm). Once F_{yield} is determined, the yield displacement can be calculated using the following relationship:

$$\text{Yield Displacement } (\Delta_{yield}) = \frac{F_{yield}}{k_e} \qquad 7$$

Table 9. The parameters required for calculation of the yield load (and the calculated value of yield load).

Parameter	Numerical value
A, mm^2	255.2
Ke, KN/mm	0.659
$\Delta_{failure}$, mm	8.26
F_{yield}, KN	5.445

4.3.7 Ductility

Ductility is an important characteristic of a structural system, which reflects its ability to yield and deform inelastically without failure. The ability of structural member to bend but not fail is important exposure to sudden and powerful cycles of an intense earthquake. Different measures have been used to express the ductility of a structure. The most commonly accepted definition is that of ASTM E2126, which defines the ductility factor, μ, as the ratio of the failure displacement to the yield displacement. The ductility ratio, derived from test results, is defined as the displacement at failure load divided by the displacement at yield load (Salenikovich, Dolan et al. 1999, Thomsen IV and Wallace 2004)

$$\text{Ductility Ratio} = \mu = \frac{\Delta_{failure}}{\Delta_{yield}} \qquad 8$$

This value represents the relative displacement that a structure can undergo from yielding until failure. It reflects the ability of ductile structural systems to undergo further displacements beyond Δ_{peak}. When the structural component has reached its capacity, it transfers additional load onto other components. The ductility factor introduced above is the ratio of two displacements. If a structure undergoes large deformations before failure but has a large yield displacement, the structure is not necessarily a ductile system. The reverse is also true, so ductility should always be considered together with other performance indicators. Although ductility is an important characteristic, it should be noted that it is not a material property and caution should be used when comparing different structural systems. Given the variations that exists when calculating the elastic stiffness and yield load, a large margin for error and inconsistent results may be encountered.

The ductility factor of structural systems comprising sheathing materials varies from 4 to 10 for both OSB and hardboard (Toothman 2003) , compared to a ductility factor of 10.9 calculated for the aerated slurry infiltrated chicken mesh frame using Equation (8). The higher elastic stiffness of the frame tends to reduce its yield displacement, which raises the calculated value of ductility. These results point at the ductile behavior of the aerated slurry-infiltrated chicken mesh frame, and its ability to yield and undergo inelastic deformation to dissipate the input energy of severe earthquake ground motions.

In terms of weight, constructability, ductility and energy absorption capacity, the aerated slurry-infiltrated chicken mesh structural system seems to offer qualities which are intermediate between those of wood and reinforced concrete structural system.

4.4 Conclusions

1. An aerated slurry-infiltrated chicken mesh frame with column and beam cross-section comparable to those required for a single-story building design were subjected to cyclic lateral in-plane loading. The frame columns were fixed inside an aerated slurry-infiltrated chicken mesh footing. The frame failed by forming plastic hinges in beams near beam-column joints, which is compatible with the weak beam-strong column design of the frame.
2. The aerated slurry-infiltrated chicken mesh frame exhibited a ductile failure mode with a stable hysteretic behavior that provided significant energy absorption capacity.
3. The lateral load-bearing resistance, ductility and hysteretic energy absorption capacity of the aerated slurry-infiltrated chicken mesh frame were found to be favorable when compared with lateral load-resisting systems based on OSB and hardwood sheets.
4. The desired seismic performance of the aerated slurry-infiltrated chicken mesh frame can

be attributed to the high specific surface area of chicken mesh, its desired mechanical interlocking within the cementitious matrix, its dual role as flexural and shear reinforcement, and the confining effects of the highly-distributed chicken mesh reinforcement on the aerated slurry matrix.

5. Aerated slurry-infiltrated chicken mesh offers a desired balance of structural qualities at light weight. It is quite feasible that aerated slurry-infiltrated chicken mesh provides a desired balance of constructability, durability, and moisture and fire resistance. Its qualities seem to be intermediated between those of wood and reinforced concrete building materials.

REFERENCES

REFERENCES

Abd-Elhamed, A. and S. Mahmoud, Nonlinear static analysis of reinforced concrete framed buildings-A case study on Cairo earthquake. Journal of Engineering Research, 2017. 4(4).

Arroyo, O. and S. Gutiérrez, A seismic optimization procedure for reinforced concrete framed buildings based on eigenfrequency optimization. Engineering Optimization, 2016: p. 1-17.

Balaguru, P.N., S.P. Shah, and A.E. Naaman, Analysis and behavior of ferrocement in flexure. Journal of the Structural Division, 1977. 103(10): p. 1937-1951.

Bedoya-Ruiz, D., G. Ortiz, and D. Álvarez, Behavior of precast ferrocement thin walls under cyclic loading: an experimental and analytical study. Ingeniería e Investigación, 2014. 34(1): p. 29-35.

Cho, C.-G., et al., Cyclic responses of reinforced concrete composite columns strengthened in the plastic hinge region by HPFRC mortar. Composite Structures, 2012. 94(7): p. 2246-2253.

Costa, A.A., A. Penna, and G. Magenes, Seismic performance of autoclaved aerated concrete (AAC) masonry: from experimental testing of the in-plane capacity of walls to building response simulation. Journal of Earthquake Engineering, 2011. 15(1): p. 1-31.

Dolan, J. and A. Johnson, Cyclic tests of long shear walls with openings. Virginia Polytechnic Institute and State University, Timber Engineering Report No. TE-1996-002. Blacksburg, Virginia: VPISU, 1996.

Dolan, J.D. and C. Heine, Sequential phased displacement cyclic tests of wood-frame shear walls with various openings and base restraint configurations. 1997: Citeseer.

Dolan, J.D. and C. Heine, Sequential phased displacement tests of wood-framed shear walls with corners. 1997: Virginia Polytechnic Institute and State University.

Eskandari, H. and A. Madadi, Investigation of ferrocement channels using experimental and finite element analysis. Engineering Science and Technology, an International Journal, 2015. 18(4): p. 769-775.

Gatto, K. and C.-M. Uang, Effects of loading protocol on the cyclic response of woodframe shearwalls. Journal of Structural engineering, 2003. 129(10): p. 1384-1393.

He, M., F. Lam, and H.G. Prion, Influence of cyclic test protocols on performance of wood-based shear walls. Canadian Journal of Civil Engineering, 1998. 25(3): p. 539-550.

Huang, Z., T. Zhang, and Z. Wen, Proportioning and characterization of Portland cement-based ultra-lightweight foam concretes. Construction and Building Materials, 2015. 79: p. 390-396.

Ibarra, L.F., R.A. Medina, and H. Krawinkler, Hysteretic models that incorporate strength and stiffness deterioration. Earthquake engineering & structural dynamics, 2005. 34(12): p. 1489-1511.

Kesner, K.E., S.L. Billington, and K.S. Douglas, Cyclic response of highly ductile fiber-reinforced cement-based composites. ACI Materials Journal, 2003. 100(5): p. 381-390.

Krawinkler, H. Loading histories for cyclic tests in support of performance assessment of structural components. in The 3rd international conference on advances in experimental structural engineering, San Francisco. 2009. Citeseer.

Kwon, M., H. Seo, and J. Kim, Seismic performance of RC-frame structures with GFRP infill panels. Composite Structures, 2017. 160: p. 722-733.

Low, K.-S., S.-C. Ng, and N.-H. Tioh, Thermal conductivity of soil-based aerated lightweight concrete. KSCE Journal of Civil Engineering, 2014. 18(1): p. 220.

Memon, N.A., S.R. Sumadi, and M. Ramli, Ferrocement encased lightweight aerated concrete: a novel approach to produce sandwich composite. Materials Letters, 2007. 61(19): p. 4035-4038.

Nambiar, E.K. and K. Ramamurthy, Air-void characterisation of foam concrete. Cement and concrete research, 2007. 37(2): p. 221-230.

Ng, S.-C., K.-S. Low, and N.-H. Tioh, Potential use of clayey soil in aerated lightweight concrete. KSCE Journal of Civil Engineering, 2012. 16(5): p. 809-815.

Pankaj, M. Arif, and S.K. Kaushik, Mechanical Behavior of Ferrocement Composites: Numerical Simulation. Journal of Mateials in Civil Engineering, 2002. 14(2): p. 156-163.

Park, R., Evaluation of ductility of structures and structural assemblages from laboratory testing. Bulletin of the New Zealand National Society for Earthquake Engineering, 1989. 22(3): p. 155-166.

Porter, M.L. Sequential phased displacement (SPD) procedure for TCCMAR testing. in Proceedings of the Third Meeting of the Joint Technical Coordinating Committee on Masonry Research. 1987.

Ramamurthy, K., E.K. Nambiar, and G.I.S. Ranjani, A classification of studies on properties of foam concrete. Cement and Concrete Composites, 2009. 31(6): p. 388-396.

Rose, J.D., Preliminary testing of wood structural panel shear walls under cyclic (reversed) loading. 1998, American Plywood Association.

Ruiz-García, J. and J.D. Aguilar, Influence of modeling assumptions and aftershock hazard level in the seismic response of post-mainshock steel framed buildings. Engineering Structures, 2017. 140: p. 437-446.

Saleem, M. and J. Ahmed. Experimental characterization of ferrocement wall panels for sustainable low-cost housing in Pakistan. in Sustainable Buildings and Structures: Proceedings of the 1st International Conference on Sustainable Buildings and Structures (Suzhou, PR China, 29 October-1 November 2015). 2015. CRC Press.

Salenikovich, A.J., J.D. Dolan, and W.S. Easterling, Monotonic and cyclic tests of long steel-frame shear walls with openings. 1999.

Salenikovich, A.J., The racking performance of light-frame shear walls. 2000, Virginia Tech.

Salonikios, T.N., et al., Cyclic load behavior of low-slenderness reinforced concrete walls: failure modes, strength and deformation analysis, and design implications. ACI Structural Journal, 2000. 97(1): p. 132-141.

Soudki, K.A., et al., Horizontal connections for precast concrete shear wall panels under cyclic shear loading. PCI journal, 1996. 41(3): p. 64-80.

Subramani, T. and A. Anbuchezian, Experimental Investigation On Flexural Behavior Of Folded Ferro Cement Panels. International Journal of Application or Innovation in Engineering & Management (IJAIEM), 2017. 6(3): p. 045-049.

Tanner, J.E., et al., Seismic testing of autoclaved aerated concrete shearwalls: a comprehensive review. ACI structural journal, 2005. 102(3): p. 374.

Thomsen IV, J.H. and J.W. Wallace, Displacement-based design of slender reinforced concrete structural walls—experimental verification. Journal of Structural Engineering, 2004. 130(4): p. 618-630.

Toothman, A.J., Monotonic and cyclic performance of light-frame shear walls with various sheathing materials. 2003, Virginia Polytechnic Institute and State University.

Wakili, K.G., et al., Thermal behaviour of autoclaved aerated concrete exposed to fire. Cement and Concrete Composites, 2015. 62: p. 52-58.

Yun, H.-D., et al., Shear behavior of strain-hardening cement composite walls under quasi-static cyclic loading. Engineering Structures, 2017. 143: p. 398-409.

Zhang, Z., et al., Geopolymer foam concrete: an emerging material for sustainable construction. Construction and Building Materials, 2014. 56: p. 113-127.

Zhenggang, C., et al., Cyclic testing and parametric analyses of the fabricated steel frames infilled with autoclaved aerated concrete panels. Advances in Structural Engineering, 2017. 20(4): p. 629-640.

CHAPTER 5: EVALUATION OF THE ENERGY-EFFICIENCY OF AN AERATED SLURRY-INFILTRATED MESH BUILDING SYSTEM WITH BIOMASS-BASED INSULATION

This chapter was first published as "Evaluation of the Energy-Efficiency of an Aerated Slurry-Infiltrated Mesh Building System with Biomass-Based Insulation." Almalkawi, Areej T., Parviz Soroushian, and Som S. Shrestha. *Renewable energy* 133 (2019): 797-806.

5.1 Introduction

Beneficial use of thermal mass is an important consideration in design of climate-adapting sustainable buildings (Park 2015, Karol 2017, Ramakrishnan, Wang et al. 2017). The growing need for energy-efficient buildings with optimum thermal comfort has increased the reliance on thermal mass to meet these requirements (Perino and Serra 2015, Stazi, Bonfigli et al. 2015). Construction of buildings with heavier materials, including concrete and masonry, used within the insulation system, leads to reduced temperature swing in the indoor temperature (Zhu, Hurt et al. 2009). The high thermal inertia of such buildings allows for effective radiant heating in winter, and reduces the chance of indoor overheating in summer (Navarro, de Gracia et al. 2016, Johra and Heiselberg 2017, Lydon, Hofer et al. 2017). Building systems with high thermal mass, on the other hand, require more time to cool down or heat up. This feature could translate into thermal discomfort; more energy could also be used for heating and cooling to compensate for this effect (Hoes, Trcka et al. 2011). There are thus conditions where buildings constructed with lighter materials (e.g., wood) can offer improved thermal performance when compared with heavier buildings (Hoes and Hensen 2016, Johra and Heiselberg 2017). Opting for an effective amount of thermal mass is always critical, and depends on a number of factors, including climatic

conditions, occupancy patterns, internal heat gains, building orientation, and types of mechanical devices (Gelegenis and Axaopoulos 2017, Rehman 2017). These factors should be considered integrally with the thermal mass and insulation requirements to minimize the overall energy demand and maximize the thermal comfort of the building interior (Hoes, Trcka et al. 2010, Hoes and Hensen 2016). The availability of new building materials offer more options to address this challenging issue. Examples include hollow block walls, ventilated slabs (Ren and Wright 1998), phase change materials (PCM)(Zhou, Zhao et al. 2012), dynamic insulation systems (Imbabi, Elsarrag et al. 2012), and ultra-light-weight concrete (ULWC) (Roberz, Loonen et al. 2017).

The investigation reported herein covers the thermal aspects of developing a new building material, referred to as aerated slurry-infiltrated mesh, which is focused on maximum use of locally available materials (including insulation materials) towards development of sustainable, structurally safe and energy-efficient buildings. This building system offers an intermediate thermal mass, which occurs between those of wood and concrete building systems. The thermal mass provided is selected primarily based on structural requirements, and should be supplemented with proper indigenous insulation levels for realizing desired energy-efficiency and thermal comfort (Devi and Palaniappan 2014). The selection of thermal insulation must satisfy many criteria, including energy performance, economics, environmental impacts, and compatibility with structural design.

This work covers measurement of the insulation qualities of aerated slurry-infiltrated mesh and biomass-based insulation materials. The results are used, together with the structurally governed mass of the building, to identify the insulation conditions which yield desired thermal performance.

5.2 Experimental Evaluation of Insulation Qualities

5.2.1 Materials

5.2.1.1 Aerated Slurry

The aerated slurry had a water/cement ratio of 0.6; a foaming agent was used at different dosages to produce hardened material bulk densities ranging from 0.65 to 1.15 g/cm^3 (in oven-dried condition).

The aerated slurry was prepared by first mixing a foaming agent (saponin) with the mixing water for 6 minutes, using a drill with a blade attached to it and operated at a rotational speed of 1200 rpm (**Figure 43a.**) .The resulting foamed mixing water was then added to cement and mixed for 12 minutes in a planetary mortar mixer (**Figure 43**b.) to produce a homogeneous aerated slurry.

(a) Mixing of the foaming agent with water (b) Mixing of foamed water with cement

Figure 43. Preparation of the aerated slurry.

The thermal conductivity test specimens (**Figure 44**.) were in the form of thin circular plates. They were molded and consolidated under external vibration, demolded after 24 hours of storage in sealed condition, and then cured at >95% relative humidity) and room temperature to reach 7 days of age. The specimens were then oven-dried for 24 hours at 105±5^{o}C, weighed for evaluating their bulk density, and subjected to the thermal conductivity experiment.

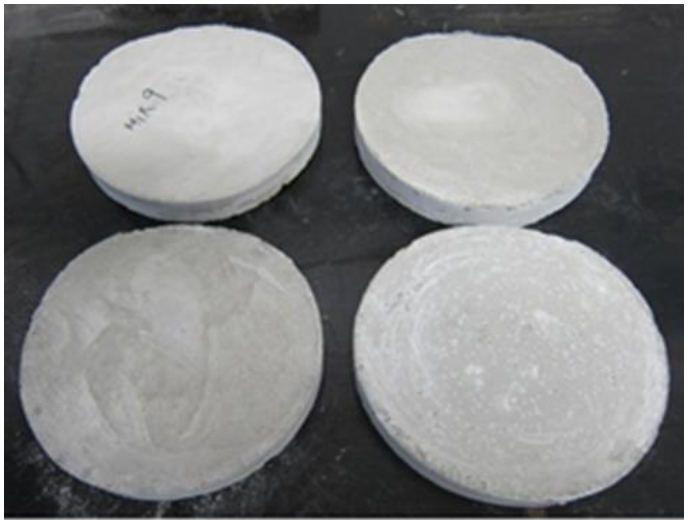

Figure 44. Examples of the aerated slurry thermal conductivity test specimens.

5.2.2 Biomass-Based Insulation Materials

Three categories of biomass-based insulation were used in this investigation: (i) ground wood; (ii) shredded straw; and (iii) a commercially available blow-in cellulose insulation. These three insulation materials are described in the following. The thermal conductivity test specimens of different biomass-based insulation materials had the same geometric attributes as the aerated slurry thermal conductivity test specimens.

5.2.2.1 Ground Wood Insulation

Wood branches collected locally (in air-dried condition) were ground using a hammer mill (**Figure 45**). The ground wood was passed through a sieve with 2.36 mm opening. **Figure 46**. shows the appearance of the resulting ground wood insulation. While the ground wood insulation was used without any treatment, mitigation of microbial degradation ay require their treatment. **Figure 47.** shows the particle size distribution of the ground wood insulation. The median particle size was about 0.8 mm, with particles ranging in size from 0.3 to 0.5 mm. The loosely packed ground wood had a bulk density of 0.291 g/cm^3.

Figure 45. The hammer mill used for grinding of wood.

Figure 46. Ground wood insulation.

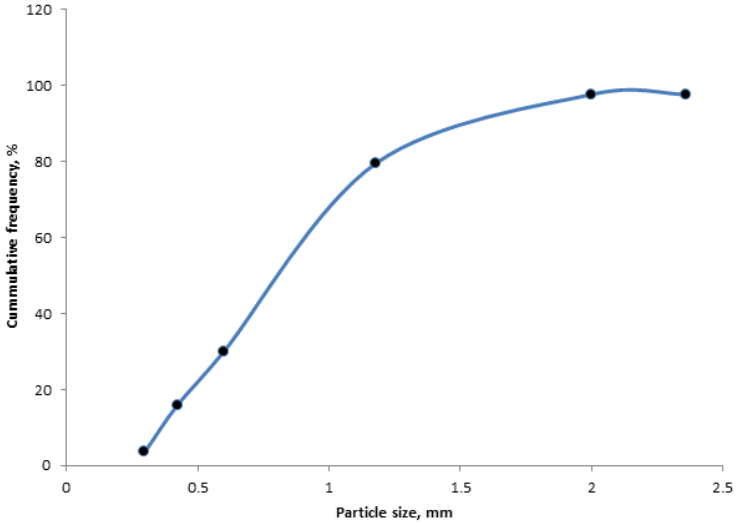

Figure 47. Particle size distribution of the ground wood insulation.

5.2.2.2 Shredded Straw Insulation

Wheat straw was shredded in the hammer mill shown in **Figure 48**. This mill is Type MUR manufactured by the American Pulverizer Co.; it has a 10 mm diameter sieve installed on it. The visual appearance of the resulting shredded straw insulation is presented in **Figure 49**. The length distribution of shredded straw is presented in **Figure 50**. Most straw fibrils are noted to be less than 1.5 mm in length. The loosely packed shredded straw insulation provided a bulk density of 0.069 g/cm^3.

Figure 48. The hammer mill used for shredding of straw.

Figure 49. Shredded straw insulation.

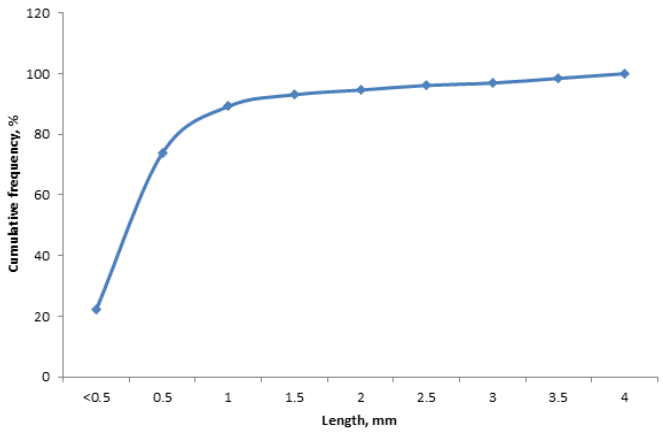

Figure 50. Length distribution of the shredded straw.

5.2.2.3 Commercially Available Cellulose

The commercially available cellulose (Green Fiber) insulation used in this investigation **Figure 51**. is available as a "low dust blow-in" insulation. According to the manufacturer, this insulation would provide a thermal conductivity of 0.042 W m^{-1} K^{-1} at 25° C when packed loosely with a bulk density of 0.056 g/cm^3. The cellulose insulation was used in this investigation at the manufacturer's recommended bulk density of 0.056 g/cm^3, and in loosely and densely packed conditions with bulk densities of 0.068 and 0.034 g/cm^3, respectively.

Figure 51. The commercially available cellulose (Green Fiber) 'low dust blow-in' insulation.

5.2.3 Thermal Conductivity Test Method

Thermal conductivity measurements were made using a test setup **Figure 52**. manufactured by Holometrix GHP that meets the ASTM C177 requirements. In this test, two similar specimens are placed between a middle hot plate and two outside cold plates. The hot and cold plates were typically kept at constant 30^{o}C and 20^{o}C temperatures, respectively, to represent the outdoor and indoor temperatures. The effects of temperature on the thermal conductivity of different insulation materials was also investigated. Temperatures on the hot and cold plates as well as the heat flow were monitored over a 24-hour time period. The results, after the processed reached equilibrium, were used to calculate the thermal conductivity of test specimens.

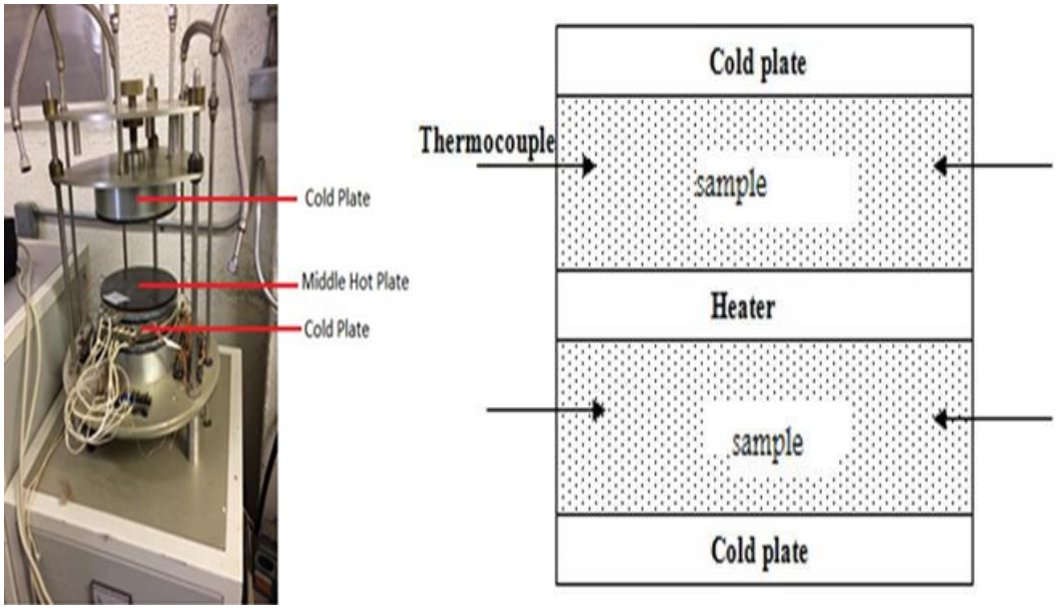

(a) Picture (b) Schematic

Figure 52. Thermal conductivity test setup.

The thermal conductivity test specimens used in this experimental work were circular plates of 195 mm diameter and 25.4 mm thickness. They were produced by containing the loose

insulation materials within a ring fabricated using a flexible polypropylene sheet of 1 mm thickness (**Figure 53.**) The ground wood, shredded straw and commercially available cellulose insulation test specimens are shown in **Figure 54**.

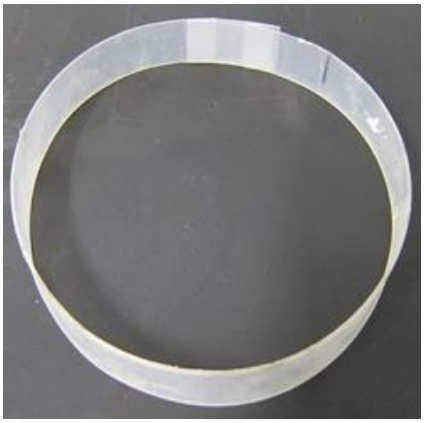

Figure 53. The polypropylene ring used to prepare biomass insulation materials.

(a) Ground wood (b) Shredded straw (c) Cellulose

Figure 54. Insulation specimens for thermal conductivity test.

5.2.4 Thermal Conductivity Test Results

The measured values of thermal conductivity for the ground wood, shredded wheat straw and cellulose (0.056 g/cm^3 bulk density) insulation materials were 0.0516, 0.0379 and 0.0389 W/m.K, respectively **Figure 55**. The indigenous insulation materials (ground wood and shredded straw) thus provide insulation qualities that are of the same order of magnitude of that provided by the commercially available cellulose insulation. The bulk density and thermal conductivity of

shredded straw and cellulose were comparable. Ground wood with a higher bulk density provided a higher level of thermal conductivity.

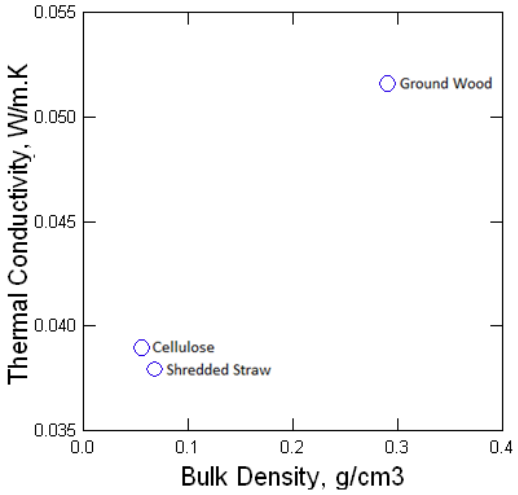

Figure 55. The relationship between the thermal conductivity and the bulk density of the three biomass-based loose insulation materials.

As noted earlier, the cellulose insulation material was tested at different bulk densities. The thermal conductivity test results presented in **Figure 56.** indicate that changing the bulk density to less than or more than the manufacturer's recommended level both reduce the thermal conductivity of the cellulose insulation. The thermal conductivity of these loose insulation materials is governed by a combination of conduction, convection and radiation. Their thermal conductivity is influenced by a number of factors including porosity and pore size distribution (Shrestha, Desjarlais et al. 2014).

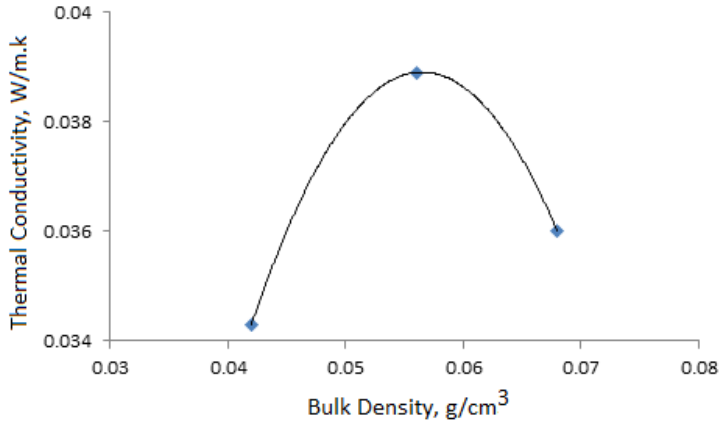

Figure 56. Effect of the cellulose insulation bulk density on its thermal conductivity.

The effects of temperature on the thermal conductivity of the biomass-based loose insulation materials were also investigated **Figure 57.** In this series of tests, the temperature difference of hot and cold plates was kept constant at 10^{o}C; the effects of the mean temperature (of hot and cold plates) on thermal conductivity were investigated. Thermal conductivity is observed to increase with increasing temperature; this effect is less pronounced in the case of the ground wood insulation. Conductive, convective and radiative heat transfer are influenced differently by temperature (and temperature gradient). The trends in temperature effects on thermal conductivity depend, among other factors, on the pore size of insulation materials (Shrestha, Desjarlais et al. 2014). The observed rise in thermal conductivity with increasing temperature is not unusual for insulation materials with multi-faceted heat transport mechanisms.

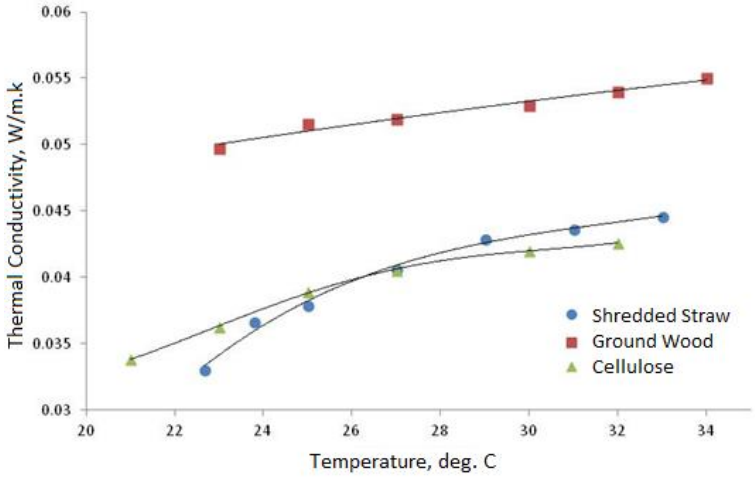

Figure 57. Thermal conductivity versus temperature for the loose biomass-based insulation materials.

The thermal conductivity test results for aerated slurries of different bulk densities are presented in **Figure 58**. The pore system in aerated slurry comprises isolated individual pores. Convective heat transfer can thus occur only within pores (and not between them). Given this condition, and since the cementitious binder is thermally more conductive than air, replacement of air with the cementitious matrix in aerated slurries of higher densities would produce higher thermal conductivities.

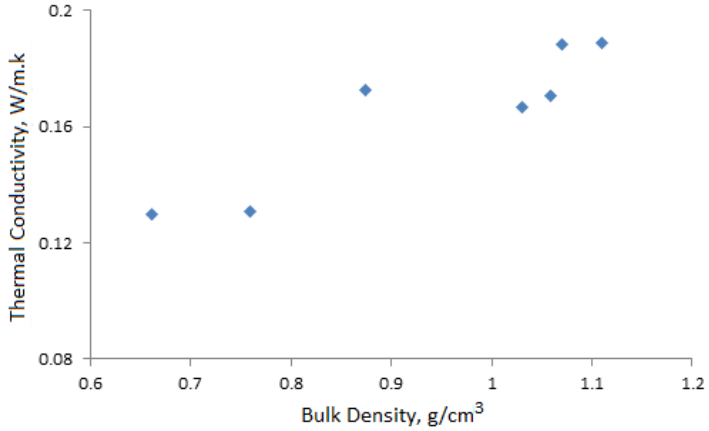

Figure 58. Thermal conductivity test results for aerated slurries of different bulk densities.

5.3 Thermal Simulation and Design of the Building System

A simple aerated slurry-infiltrated chicken mesh building designed to meet structural requirements was subjected to thermal analysis in order to evaluate its insulation requirements. The building planar dimensions are 4.9 m x 9.8 m, and its height is 2.4 m. The building structure (**Figure 59**.) comprises nine aerated slurry-infiltrated chicken mesh frames of 0.75 g/cm^3 bulk density to which external wall, internal wall all, roof and ceiling aerated slurry-infiltrated chicken mesh sheets are screwed. The floor also comprises aerated slurry-infiltrated chicken mesh sheets, which span the frame footings and are supported on compacted sand. All (roof, ceiling, wall and floor) sheets have a bulk density of 0.75 g/cm^3. The interior and exterior sheets are 19 and 25.4 mm thick, respectively.

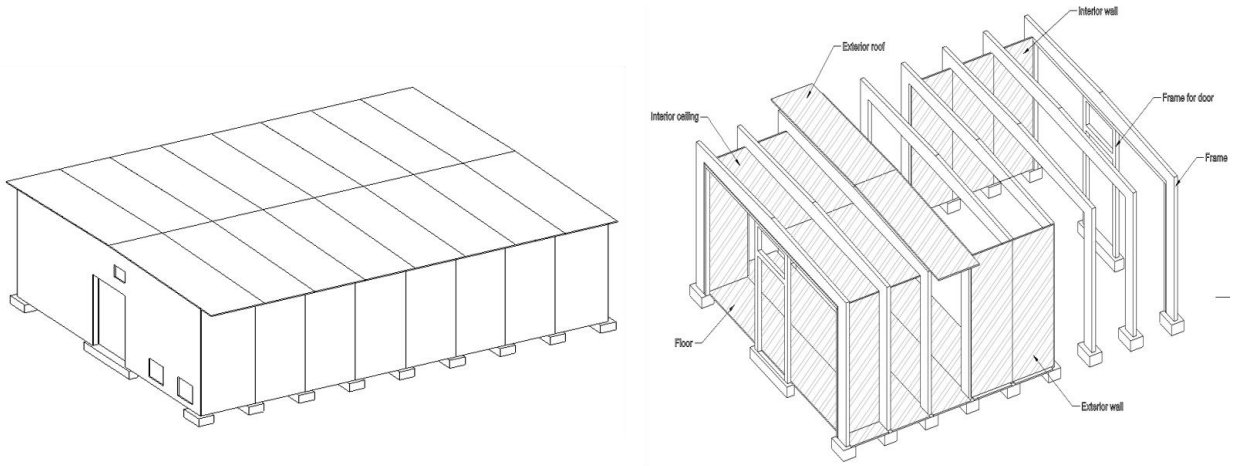

Figure 59. The building system.

5.3.1 Thermal Simulation of the Building System

The building system considered here serves military purposes and is used for business and residential occupancy during the day and at night, respectively. The building plans with business and residential occupancy patterns are presented in Figure 60. The design factors used in simulation of the building system using the eQUEST software are introduced in **Table 10.**

. The eQUEST software allows for multiple simulations of alternative building designs for comparative estimation of energy cost (Crawley, Hand et al. 2008, Yezioro, Dong et al. 2008, Rallapalli 2010). The energy-efficiency of the building system made with aerated slurry-infiltrated chicken mesh should be compared with those fabricated with wood which is prevalent in construction of small buildings. The building orientation considered in this analysis is depicted in **Figure 61**.

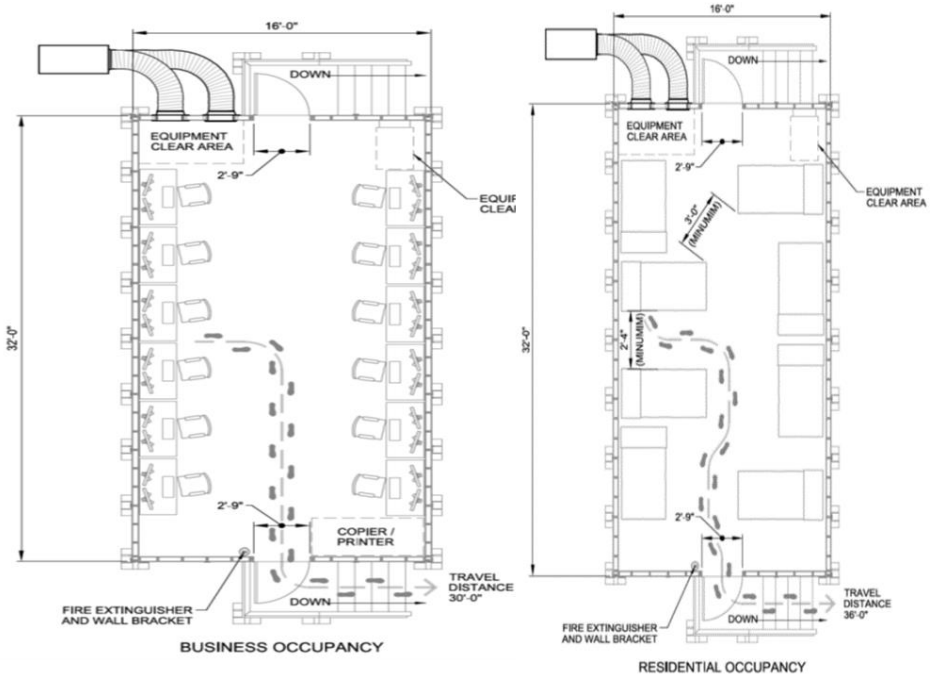

Figure 60. Building plans with business and residential occupancy patterns (1 ft = 0.305 m).

Table 10. The design factors used in simulation of the building system.

Design Factor	Value
Location	Amman- Jordan
Latitude (degree)	31.87
Longitude (degree)	35.22
Time zone (h)	2
Elevation (m)	757
People per zone floor	(Based on 1.4 m^2 per person = 34 persons per 48 m^2)
Occupancy schedule	Office schedule
Lighting	
Lighting schedule	Office light
Lighting power density (w/m^2)	8.6
Electric equipment	
Electric equipment power density (w/m^2)	10.8
Outdoor Air per person ((m^3/min)/person))	0.142
Outdoor air per area ((m^3/min)/m^2))	0.060
Infiltration rate (ACH)	0.8

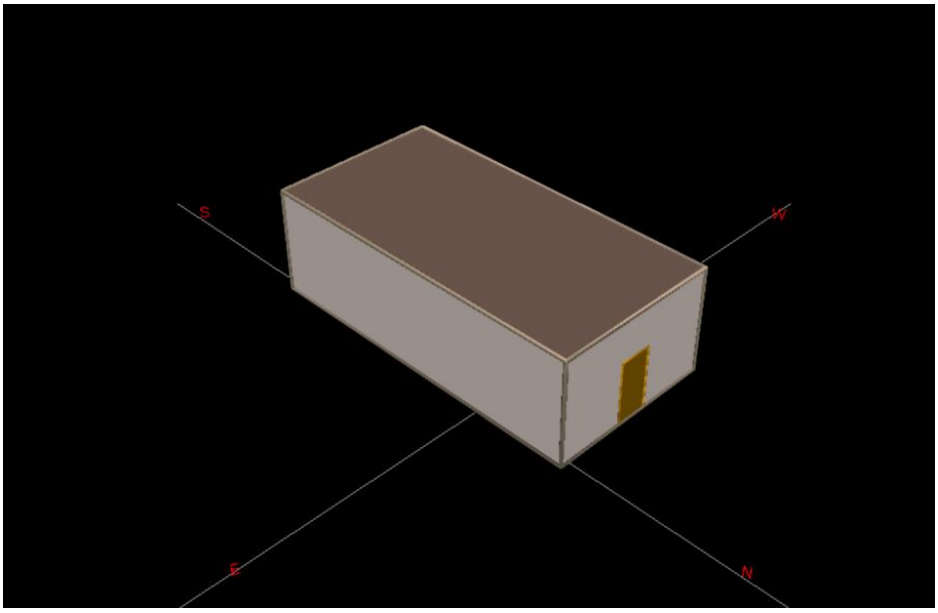

Figure 61. The building orientation.

Based on the test data introduced earlier, the thermal properties of the aerated slurry and the biomass insulation used in thermal analysis of the building are presented in **Table 11**.This table also presents typical thermal properties of plywood which is used as the control material used in construction of the conventional alternative to the building system considered here.

Table 11. Thermal properties of aerated slurry, biomass insulation, and plywood.

Material (bulk density, g/cm^3)	Thermal Conductivity, λ (W/mK)	Specific Heat, Cp (J/(kg.K))
Aerated Slurry (0.75)	0.31	870
Biomass Insulation (0.056)	0.039	840
Plywood - CDX (0.54)	0.12	1215

The thermal analysis investigate the effects of the thermal insulation levels of walls, roof and floor on the energy use of the building. Comparative analyses were also performed on the new building system versus a conventional wooden alternative to this system.

5.4 Results and Discussion

5.4.1 Energy Consumption

The building system comprises interior and exterior aerated slurry-infiltrated mesh walls, with biomass insulation placed in between the two sheets. **Figure 62**. shows the effects of the wall insulation (with roof and floor insulation kept constant) on the annual heating and cooling loads of the building. Beyond an R-value (US) of 20 wall insulation, increasing the insulation level does not reduce the heating and cooling loads of the building. Below this level of insulation, gains in the energy-efficiency of the building can be realized by adding to the wall insulation. The thickness of the biomass insulation with 0.039 W/mk thermal conductivity required to provide this level of wall insulation is 0.137 m (13.7 cm). Structural design requirements provide more than adequate spacing between exterior and interior wall sheets to place this level of biomass insulation.

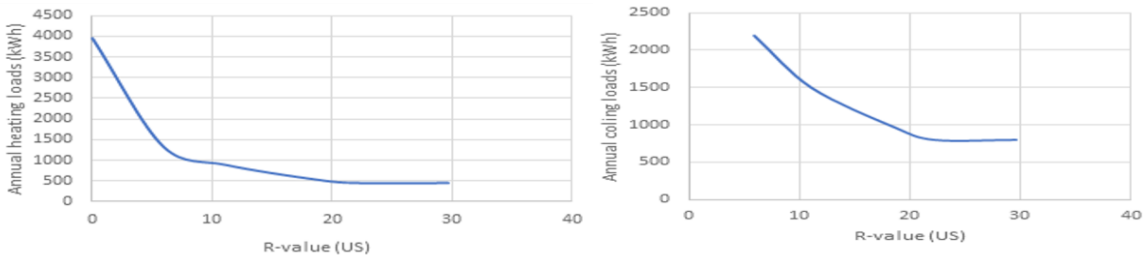

Figure 62. Effects of the wall insulation on the cooling and heating loads of the building (RSI (K.m2/W) = R-value (US) (ft2.oF.hr/Btu) /5.68).

The effects of roof insulation level on the annual heating and cooling loads of the building are presented in **Figure 63**. The heating and cooling loads are observed to decrease with increasing roof insulation up to an R-value (US) of 10, beyond which the benefits of further increasing the roof insulation level are minimal. A biomass insulation thickness of 6.85 cm would provide this required level of insulation. The cavity between the roof and ceiling sheets, decided based on structural requirements, is more than adequate for providing this level of insulation.

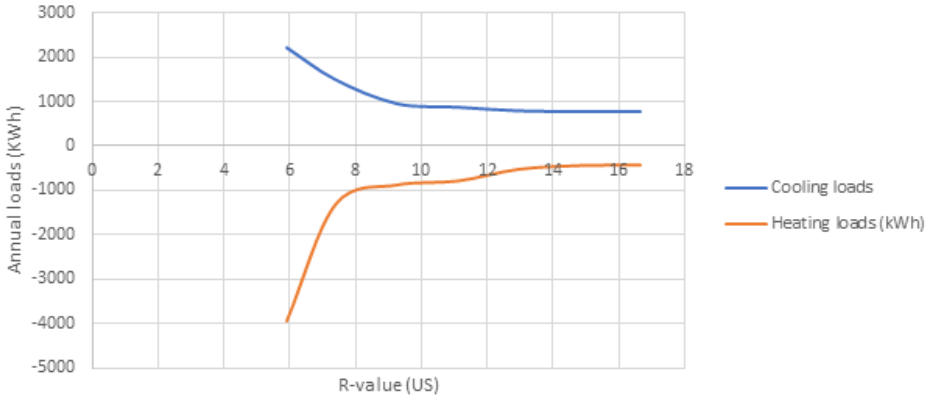

Figure 63. Effects of the roof insulation on the cooling and heating loads of the building (RSI (K.m2/W) = R-value (US) (ft2.oF.hr/Btu) /5.68).

The floor of the building system comprises an aerated slurry-infiltrated chicken mesh supported on 20.3 cm of compacted sand which provides a thermal conductivity of about 0.3

W/mK. The effects of the floor insulation levels on the annual heating and cooling loads presented in **Figure 64**. indicated that the heating and cooling energy consumption of the building decrease with increasing floor insulation up to about an R-value (US) of 4, beyond which the effects of further increasing the floor insulation level on the building energy use is minimal. Considering the insulation level provided by the aerated slurry-infiltrated chicken mesh sheet, 21 cm of compacted sand would be required under the floor sheets. Consideration of the insulation value of the aerated slurry-infiltrated chicken mesh floor sheets would reduce the required thickness of the compacted sand acting as insulation to 19 cm. The available compacted sand thickness of 20.3 cm is thus adequate for providing the required level of floor insulation.

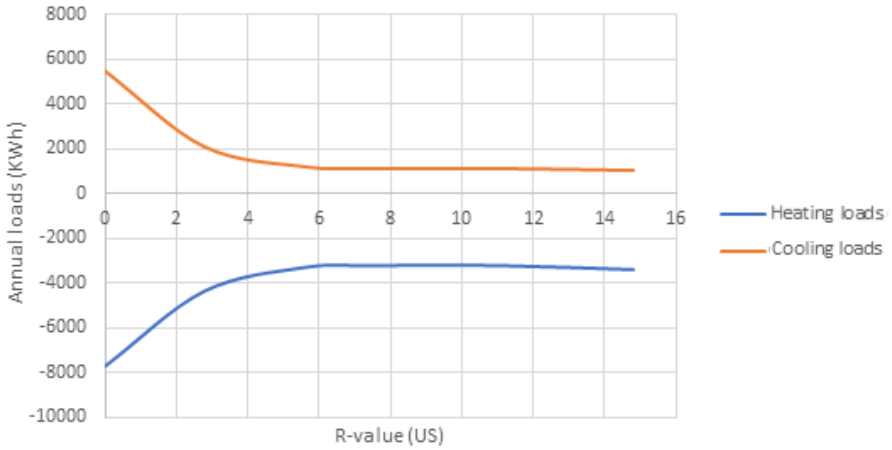

Figure 64. Effects of the floor insulation on the cooling and heating loads of the building (RSI (K.m2/W) = R-value (US) (ft2.oF.hr/Btu) /5.68).

5.4.2 Optimization of the Wall Insulation Condition

Heat loss from the building that is subject of this investigation occurs largely via transfer of heat through exterior walls in winter, noting that these walls constitute the largest surface area of the building envelope (Friess and Rakhshan 2017, Siddiqui, Kumar et al. 2017). An investigation was conducted to assess the optimum wall insulation condition, focusing on heat loss through walls (Al-Sanea, Zedan et al. 2005, Kaynakli 2011) which minimizes the cost of

meeting the energy demand of the building (Aditya, Mahlia et al. 2017). **Figure 65**. shows the effects of the wall insulation level on the energy use cost, the insulation cost, and the total cost. The total cost is observed to be minimized at wall insulation levels ranging from R-value (US) of 5 to 8, which correspond to biomass insulation thicknesses occurring within the 3.4 to 5.5 cm range.

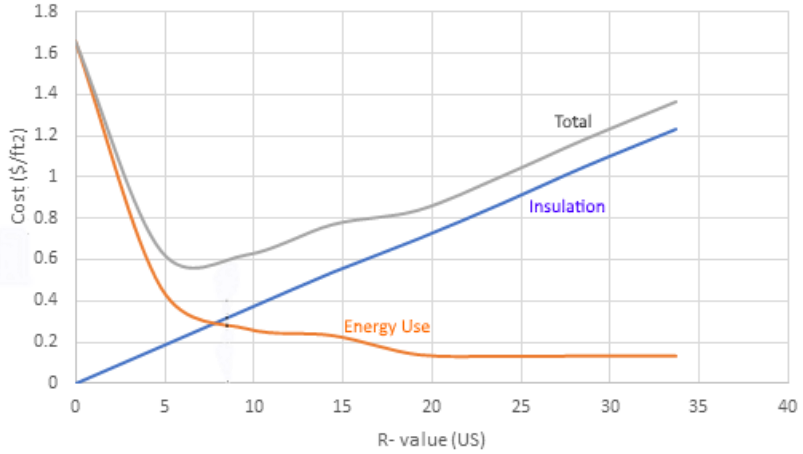

Figure 65. The heating/cooling, insulation and total costs versus the wall insulation condition.

5.4.3 Comparison with a Conventional Wood Building

While the aerated slurry-infiltrated mesh building structure is developed to be lightweight, it still weighs more than a conventional building system with wood structure. The thermal mass of the aerated slurry-infiltrated mesh building would thus be larger than that of a wood building. A larger thermal mass generally reduces the energy demand of a building, and favorably influences thermal comfort (Kosny, Petrie et al. 2001). Thermal time constant (TTC) is a thermal attribute of building envelopes that incorporates thermal mass. TTC is defined as the heat stored in the whole envelope (including internal air) per unit of heat transmitted to or from the outside through the elements surrounding the enclosure and by ventilation (Naji, Çelik et al. 2014, Wang 2015). It is the product of heat capacity (Q) and thermal resistance (R). TTC provides

an indication for the effective thermal capacity of a building. A shorter value of TTC indicates that a smaller heat flux would be required to achieve a unit change in temperature. A longer TTC value, on the other hand, suggests that the high thermal inertial of the building suppresses indoor temperature fluctuations.

The value of heat capacity per unit area (Q_A, J/m^2.K) can be calculated as follows (Athienitis and Santamouris 2013):

$$Q_A = \rho . d . c_p$$

where, ρ is the material density (kg/m^3), d is the thickness of the material (m), and c_p is the specific heat of the material (J/kg.K). In calculating TTC_A (TTC per unit area, seconds) of a composite wall, the Q_A.R value of each layer, including the outside and inside air layers, is calculated in sequence:

$$TTC_A = \sum_{i=1}^{n} Q_{Ai} . R_i$$

where, $Q_{Ai} . R_i = \left(\rho . d . c_p\right) . (R_0 + R_1 + \cdots + R_i)$, and n is the number of layers.

The value of TTC for each surface is the product of TTC_A and the surface area. Surfaces of higher TTC value reflect further benefits that can be realized from thermal mass (Liping and Hien 2007, Al-Sanea, Zedan et al. 2012). For the walls (**Figure 66**.) of the building system designed with aerate slurry-infiltrated mesh, the value of TTC_A was 13% larger than that designed with plywood (CDX). The total cooling and heating energy demands of the two building systems over a 12-month period are presented in **Figure 67**. and **Figure 68**. respectively. The aerated slurry-infiltrated mesh building is observed to be more energy-efficient than the wood building, which can be largely attributed to its larger thermal mass.

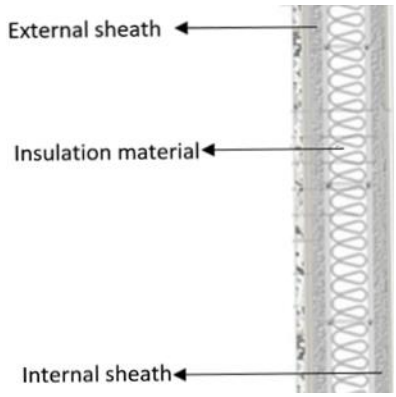

Figure 66. Schematics of a layered wall structure.

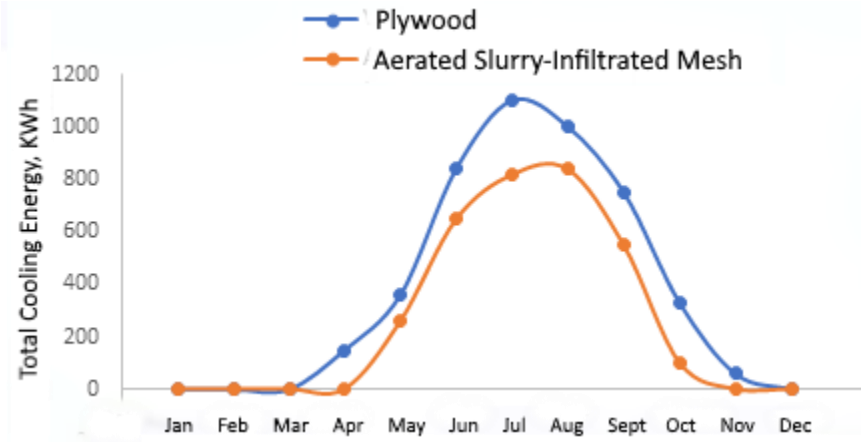

Figure 67. Cooling energy demand of the two building systems.

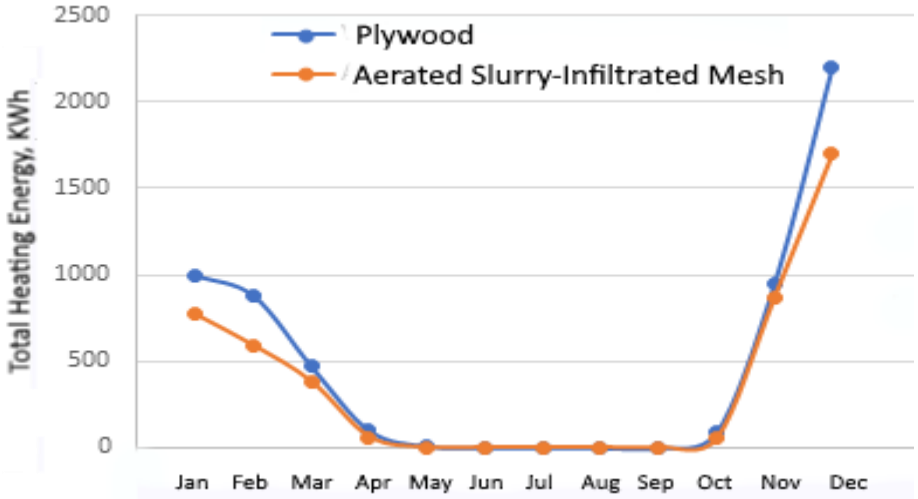

Figure 68. Heating energy demands of the two building systems.

5.5 Conclusions

Experimental and numerical investigations were conducted towards development of a building system that can be constructed using locally available structural and insulation materials. The structural material used here is referred to as aerated slurry-infiltrated mesh. The insulation materials are biomass-based, and include ground wood, shredded straw, and cellulose. The following conclusions were derived based on the experimental and numerical data generated in this work

1. Shredded straw with lengths less than 1.5 mm and a bulk density of about 0.069 g/cm^3 in oven-dried condition as well as ground wood with a particle size distribution largely covering the 0.5-2.5 mm range and a bulk density of about 0.291 g/cm^3 provided viable levels of thermal conductivity which were comparable to those provided by commercially available cellulose insulation materials.

2. Changing the bulk density of the loose biomass-based insulation materials to less than or more than a particular level reduces their thermal conductivity. The thermal conductivity of these loose insulation materials is governed by a combination of conduction, convection and radiation. Their thermal conductivity is influenced by a number of factors, including porosity and pore size distribution.

3. Thermal conductivity of loose biomass-based insulation materials included with increasing temperature; this effect was less pronounced in the case of the ground wood insulation. Conductive, convective and radiative heat transfer are influenced differently by temperature (and temperature gradient). The trends in temperature effects on thermal conductivity depend, among other factors, on the pore size of insulation materials. The observed

rise in thermal conductivity with increasing temperature is not unusual for insulation materials with multi-faceted heat transfer mechanisms.

4. In the case of aerated slurry, thermal conductivity was found to increase with increasing bulk density. The pore system in aerated slurry comprises isolated individual pores. Convective heat transfer can thus occur only within pores (and not between them). Given this condition, and since the cementitious binder is thermally more conductive than air, replacement of air with the cementitious matrix in aerated slurries of higher densities would produce higher thermal conductivities.

5. Thermal analysis of a building system made with aerated slurry-infiltrated mesh led to identification of wall, roof and floor insulation levels beyond which further rise in insulation level does not produce notable gains in energy-efficiency. Thicknesses of typical biomass-based insulation (and compacted sand in the case of floors) for providing the identified levels of insulation were determined. The structural design provides adequate space for placement of the required biomass-based insulation. Optimum levels of wall insulation were identified based on cost considerations.

6. The thermal mass of the aerated slurry-infiltrated mesh building system was found to benefit its energy-efficiency when compared with an equivalent building fabricated with wood.

REFERENCES

REFERENCES

Aditya, L., et al., A review on insulation materials for energy conservation in buildings. Renewable and Sustainable Energy Reviews, 2017. 73: p. 1352-1365.

Al-Sanea, S.A., M. Zedan, and S. Al-Hussain, Effect of thermal mass on performance of insulated building walls and the concept of energy savings potential. Applied Energy, 2012. 89(1): p. 430-442.

Al-Sanea, S.A., M. Zedan, and S.A. Al-Ajlan, Effect of electricity tariff on the optimum insulation-thickness in building walls as determined by a dynamic heat-transfer model. Applied Energy, 2005. 82(4): p. 313-330.

Athienitis, A.K. and M. Santamouris, Thermal analysis and design of passive solar buildings. 2013: Routledge.

Crawley, D.B., et al., Contrasting the capabilities of building energy performance simulation programs. Building and environment, 2008. 43(4): p. 661-673.

Devi, P. and S. Palaniappan, A case study on life cycle energy use of residential building in Southern India. Energy and Buildings, 2014. 80: p. 247-259.

Friess, W.A. and K. Rakhshan, A review of passive envelope measures for improved building energy efficiency in the UAE. Renewable and Sustainable Energy Reviews, 2017. 72: p. 485-496.

Gelegenis, J. and P. Axaopoulos, A Multi-Parametric Mathematical Approach on the Selection of Optimum Insulation Thicknesses in Buildings. Buildings, 2017. 7(1): p. 15.

Hoes, P. and J. Hensen, The potential of lightweight low-energy houses with hybrid adaptable thermal storage: comparing the performance of promising concepts. Energy and Buildings, 2016. 110: p. 79-93.

Hoes, P., et al., Exploring the optimal thermal mass to investigate the potential of a novel low-energy house concept. 2010.

Hoes, P., et al., Investigating the potential of a novel low-energy house concept with hybrid adaptable thermal storage. Energy Conversion and Management, 2011. 52(6): p. 2442-2447.

Imbabi, M.S.-E., E. Elsarrag, and T.G. O'hara, Dynamic insulation systems. 2012, Google Patents.

Johra, H. and P. Heiselberg, Influence of internal thermal mass on the indoor thermal dynamics and integration of phase change materials in furniture for building energy storage: A review. Renewable and Sustainable Energy Reviews, 2017. 69: p. 19-32.

Karol, E., Understanding possibilities: Thermal comfort using climatic design with low energy supplementation. Energy and Buildings, 2017.

Kaynakli, O., Parametric investigation of optimum thermal insulation thickness for external walls. Energies, 2011. 4(6): p. 913-927.

Kosny, J., et al., Thermal mass-energy savings potential in residential buildings. Report no., Buildings Technology Center, ORNL, 2001.

Liping, W. and W.N. Hien, The impacts of ventilation strategies and facade on indoor thermal environment for naturally ventilated residential buildings in Singapore. Building and Environment, 2007. 42(12): p. 4006-4015.

Lydon, G., et al., Coupling energy systems with lightweight structures for a net plus energy building. Applied Energy, 2017. 189: p. 310-326.

Naji, S., et al., Structure, energy and cost efficiency evaluation of three different lightweight construction systems used in low-rise residential buildings. Energy and buildings, 2014. 84: p. 727-739.

Navarro, L., et al., Thermal energy storage in building integrated thermal systems: A review. Part 2. Integration as passive system. Renewable Energy, 2016. 85: p. 1334-1356.

Park, Y., Adapting and Communicating Urban Climate by Design. 2015.

Perino, M. and V. Serra, Switching from static to adaptable and dynamic building envelopes: A paradigm shift for the energy efficiency in buildings. Journal of Facade Design and Engineering, 2015. 3(2): p. 143-163.

Rallapalli, H.S., A comparison of EnergyPlus and eQUEST whole building energy simulation results for a medium sized office building. 2010, Arizona State University.

Rehman, H.U., Experimental performance evaluation of solid concrete and dry insulation materials for passive buildings in hot and humid climatic conditions. Applied Energy, 2017. 185: p. 1585-1594.

Ren, M. and J. Wright, A ventilated slab thermal storage system model. Building and Environment, 1998. 33(1): p. 43-52.

Roberz, F., et al., Ultra-lightweight concrete: Energy and comfort performance evaluation in relation to buildings with low and high thermal mass. Energy and Buildings, 2017. 138: p. 432-442.

Shrestha, S.S., A.O. Desjarlais, and J.A. Atchley, Thermal Performance Evaluation of Walls with Gas Filled Panel Insulation. 2014, Oak Ridge National Lab.(ORNL), Oak Ridge, TN (United States). Building Technologies Research and Integration Center (BTRIC).

Siddiqui, O., et al., Modelling for performance prediction of highly insulated buildings with different types of thermal mass. Applied Thermal Engineering, 2017. 122: p. 139-147.

Stazi, F., et al., The effect of high thermal insulation on high thermal mass: Is the dynamic behaviour of traditional envelopes in Mediterranean climates still possible? Energy and Buildings, 2015. 88: p. 367-383.

Wang, Y., Optimization for Building Control Systems of a School Building in Passive House Standard. 2015, Universität München.

Yezioro, A., B. Dong, and F. Leite, An applied artificial intelligence approach towards assessing building performance simulation tools. Energy and Buildings, 2008. 40(4): p. 612-620.

Zhou, D., C.-Y. Zhao, and Y. Tian, Review on thermal energy storage with phase change materials (PCMs) in building applications. Applied energy, 2012. 92: p. 593-605.

CHAPTER 6: AERATED CEMENT SLURRY AND CONTROLLING FUNGAL GROWTH OF LOW-COST BIOMASS-BASED INSULATION MATERIALS

This chapter was first published as " Almalkawi, A. T., & Soroushian, P. (2019). Aerated cement Slurry and controlling fungal Growth of Low-cost Biomass-Based insulation Materials. Scientific Reports, 9(1), 1-10.

6.1 Introduction

Biomass ash-based insulation in the form of wood chips or ground wood offers desired thermal insulation qualities complemented with low cost, ready availability, and favorable ecological features. There are, however, concerns with the resistance to fire, moisture and fungus growth of such insulation. The work reported herein focuses on improvement of the resistance to fungus growth of low-cost biomass-based insulation comprising largely of wood chips or ground wood.

Fungal proliferation inside buildings can have adverse effects on the health of building residents (Nevalainen and Seuri 2005, Portnoy, Kwak et al. 2005, Lee, Grinshpun et al. 2006); it can also cause discoloration and degradation of construction (Ezeonu, Price et al. 1994, Murtoniemi, Hirvonen et al. 2003, Klamer, Morsing et al. 2004). Mold growth on conventional insulation materials is habitually related to moisture occurred fro m flooding, water condensation or plumping leaks.(Nielsen, Holm et al. 2004) . Many research investigations have addressed the impact of dampness level on the tendency of construction materials to mold growth (RAUTIALA, KASANEN et al. 2000). At relatively low levels of humidity, fungi do not tend to inoculate on the surfaces of building materials (Yang and Clausen 2007) . Relative humidity levels of 70% to 90%

are sufficient to trigger fungal augmentation on construction materials (Haas, Habib et al. 2007, Viitanen, Vinha et al. 2010). Besides the relative humidity of the environment, the water holding capacity (WHC) and/or the equilibrium moisture content (EMC) of a particular building material are also important indicators of the potential for fungal growth on a material exposed to humid conditions (Choi, Lanning et al. 2010, Mensah-Attipoe, Reponen et al. 2015)

Building materials that are broadly categorized as "green" are becoming increasingly popular for indoor (and other) applications. Green indoor products are often promoted for low-emission, low-toxicity and recyclability attributes (Spiegel and Meadows 2010, Huang and Wang 2014, Kibert 2016). These qualities contrast those of the highly popular reconstituted wood products (e.g., oriented strandboard – OSB) used in interior building applications that are fabricated with such adhesives as urea formaldehyde that release harmful emissions and are prone to fungal growth.

Reconstituted wood products have realized their current prominence because they can make value-added use of wood strands/fibers/particles that are abundantly available at low cost. The work reported herein concerns the use of low-cost and abundantly available wood flakes or ground wood as insulation materials in building construction. These low-cost and abundant products would be viable as insulation materials as far as they complement viable insulation qualities with desired resistance to fungal growth as well as moisture and fire. The work reported herein concerns the insulation attributes and the resistance to fungal growth on wood flakes and ground wood. Low-cost treatment methods are also developed for achieving improved resistance to fungal growth.

Bio-based materials have been used in construction for centuries[46]. They can exhibit desired durability and may deteriorate under the action of microorganisms such as fungi and bacteria. The activity of such microorganisms depends mainly on environment factors (relative humidity and temperature), and also on the building material (substrate) characteristics such as hygroscopicity (Schmidt 2006, Yang and Li 2007) . Bio-based materials may hold a potential source of nutrients for fungal and bacterial activity. Under similar environmental conditions, different bio-based materials may be affected differently by mold growth (Palumbo, Navarro et al. 2015, Palumbo, Lacasta et al. 2017). Their resistance against mold growth decides their suitability for construction application. This property is usually assessed in the critical moisture content that is amenable to fungal growth (Sedlbauer 2001, Brischke and Thelandersson 2014).

Resistance of materials to mold growth can be enhanced by the addition of biocides. Boric acid and derived salts (borates) are widely used as biocide along with commercial insulation materials such as blowing cellulose (Palumbo Fernández 2015, Palumbo, Lacasta et al. 2017). Such substances have the dual-action as a biocide and as a fire retardant; they are viewed as a greener alternative to metal-based fungicides (Hernandez-Torres, Chen et al. 2017), commonly considered in wood preservation; their toxicity is, however, scrutinized nowadays (Fernández-Calviño, Rousk et al. 2017, Kobetičová and Černý 2017, Piemonte, Francioni et al. 2017). Another approach is the use nonbiocidal techniques for protection against fungi (Morrell 2017, Palumbo, Lacasta et al. 2017, Winandy and Morrell 2017). Bio-based insulation materials can be impregnated with water repellents, such as waxes(Frenkel 2017) , or pretreated to reduce their hygroscopicity (Essoua, Beauregard et al. 2017, Li, Ye et al. 2017) . This work evaluated the

effectiveness of impregnating bio-based thermal insulation materials with aerated cement slurry in order to improve their resistance to fungal growth in different humidity conditions.

6.2 Materials

6.2.1 Wood Particles

Wood branches collected locally (in air-dried condition) were ground using a hammer mill. The resulting wood particles were passed through a sieve with 2.36 mm opening**.**

Figure 69. shows the appearance of the fine wood particles which were evaluated as insulation material. While these fine wood particles could be used for thermal insulation without any treatment, mitigation of microbial degradation would be a concern. **Figure 70.** shows the particle size distribution of the fine wood particles using sieve analysis method. The median particle size was about 0.8 mm, with particles ranging in size from 0.3 to 2.36 mm. The loosely packed fine wood particles had a bulk density of 0.291 g/cm^3.

Figure 69. Fine wood particles.

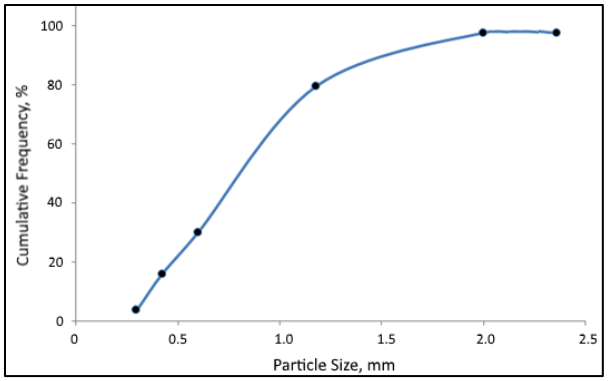

Figure 70. Particle size distribution of the ground wood.

6.2.2 Wood Chips

Wood chips with less than 25 mm particle size (**Figure 71**.) were also considered as sustainable insulation materials. The particle size distribution of these wood chips is presented in **Figure 72**. The bulk density of these wood chips was 0.205 g/cm^3.

Figure 71. Wood chips.

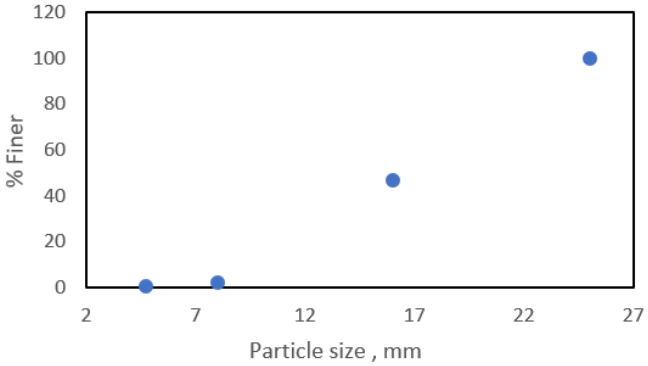

Figure 72. Particle size distribution of the wood chips insulation.

6.2.3 Shredded Straw

Shredded wheat straw (**Figure 73**.) with the length distribution shown in **Figure 74**. was also used in this investigation. The bulk density of shredded straw was 0.610 g/cm^3.

Figure 73. Shredded straw.

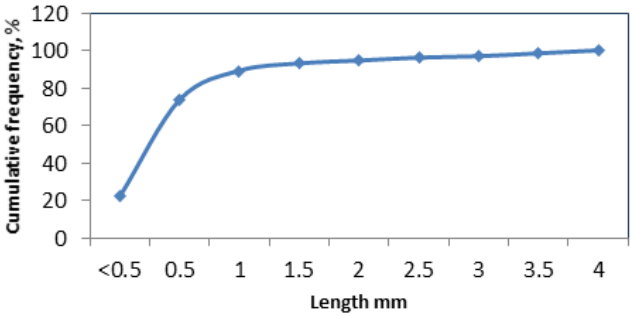

Figure 74. Length distribution of the shredded straw.

6.2.4 Treatment of Biomass with Aerated Slurry

An aerated cement slurry was used for pretreatment of fine wood particles, wood chips and shredded straw in order to improve the resistance of biomass to fungal growth without imposing major weight penalties. The aerated slurry was prepared at a water/cement ratio of 0.6, with saponin used as the foaming agent. Saponin was first added to the mixing water and stirred at a rotational speed of 1,200 rpm to produce a stable foam. The foamed water was then mixed with cement in a planetary mixer over 12 minutes to produce a homogenous aerated slurry; the dosage of the foaming agent (saponin) was adjusted to produce (after curing and oven-

drying of slurry) a bulk density of 0.75 g/cm^3. Physical and mechanical properties of aerated slurry cement were studied in our previous works (Almalkawi, Hamadna et al. 2017, Almalkawi, Salem et al. 2018, Almalkawi, Hong et al. 2018, Almalkawi, Hong et al. 2018, Almalkawi, Soroushian et al. 2019). The aerated slurry was added to fine wood particles, wood chips or shredded straw at an aerated slurry-to-biomass weight ratio of 0.2 in a drum mixer. **Figure 75**. shows wood chips after treatment with aerated slurry. This treatment raised the bulk density of wood chips, finer wood particles and shredded straw from 0.291 to 0.295, from 0.205 to 0.214, and from 0.610 to 0.627, respectively.

Figure 75. Wood chips treated with aerated cement slurry.

The thermal conductivities of find wood particles and wood chips measured, prior to an after treatment with aerated cement slurry, are summarized in **Table 12.** When compared with the thermal conductivities of commercially available thermal insulation materials such as expanded polystyrene (Styrofoam), that is 0.033 W/m.K, fine wood particles and wood chips are observed to provide reasonable low thermal conductivities for use as thermal insulation in building construction. The thermal conductivity of shredded straw was more than three times those of fine wood particles and wood chips, which could be due to convective heat transfer of loose straw. Treatment of wood straw with aerated slurry slightly reduced its thermal conductivity, which could be due to a slight reduction in the convective heat transfer. This trend

was opposite of that observed with fine wood particles and wood chips, which experienced a slight rise in thermal conductivity after treatment with aerated slurry.

Table 12. Thermal conductivities of fine wood particles and wood chips.

Specimen	Thermal conductivity, W/m.K
Fine wood particles	0.0516
Fine wood particles (treated)	0.0535
Wood chips	0.0638
Wood chips (treated)	0.0587
Shredded straw	0.196
Shredded straw (treated)	0.189

6.3 Methods

6.3.1 Water-Holding Capacity

The water-holding capacity of the insulation materials was measured by keeping triplicate samples (container sized 4 cm cube) in water as submerged condition till the saturation for flooding simulation purposes. The maximum water-holding capacity (WHC, %) of the samples was expressed as the mass ratio of water to dry materials in Equation.

$$WHC = (M_{final} - M_{initial})/M_{initial} \times 100$$

where, $M_{initial}$ is the initial weight of air-dried sample (g), and M_{final} is the weight of fully saturated sample (g). The mean and standard deviation values were computed for all triplicated samples.

6.3.2 Equilibrium Moisture Content

The equilibrium moisture content of the insulation samples was measured according per ASTM C1498-04a (2004) and ASTM D2216-05 (2005). Samples of insulation materials (5 cm cube) were dried initially at 105°C to reach a constant mass. Triplicated insulation materials kept in

sealed condition in 48 L stainless-steel chambers with relative humidity (70%) and temperature range of (22-25^{o}C). A constant air exchange rate of 1 h^{-1} was maintained and passed through the chamber at relative humidity of 70%. The weight of each specimen was monitored over regular intervals for constant mass observation, the equilibrium moisture content was determined per the equation:

$$EMC = (M_{final} - M_{initial})/M_{initial} \times 100$$

where, EMC is the equilibrium moisture content (%); where, $M_{initial}$ is the initial weight of air-dried sample (g) and M_{final} is the weight of sample at equilibrium condition with the water vapor in air inside the chamber (g). the values averaged for all triplicated measurements .

6.3.3 Artificial Inoculation

The aim of this investigation was to testify the vulnerability of insulation materials to augmentation by a model fungal species subjected to different nutrient sources at favorable temperature and humidity ranges. Aspergillus niger was chosen as the ideal fungus type for this indoor environment condition (Rao, Burge et al. 1996, Bartlett, Kennedy et al. 2004, Lee, Grinshpun et al. 2006). The A. niger strain was obtained from the American Type Culture Collection (Rockville, MD, USA) with designed number (ATCC 9642). Development of spore (conidia) inocula was conformed per the ASTM G21-96. A spore suspension was stimulated by augmenting the fungi for two weeks on V8 agar culture. 5 ml of a based wetting-agent solution (0.2% $NaNO_3$, 0.05% KCl , 0.03% K_2HPO_4, 0.05% $MgSO_4$, 0.02% KH_2PO_4 ,0.01% Tween 80 , 0.001% $FeSO_4$,) was poured in Petri dish, and the culture were kindly moved to a sterile bottle. The insulation materials were artificially inoculated by spraying 0.4 ml of suspension solution onto

the specimens. The confined Petri dishes (**Figure 76**.) holding the wetted and inoculated materials were kept in a sterile bench at incubation conditions 25^{o}C for 28 days.

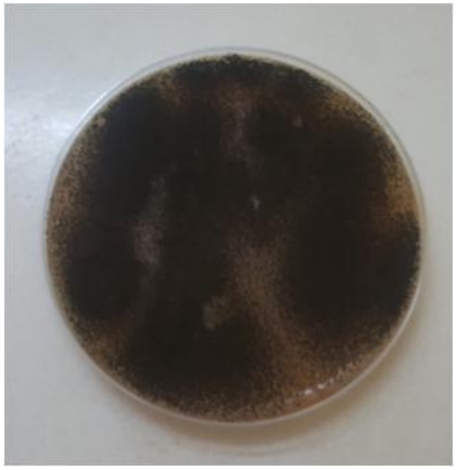

Figure 76. Fungi (Aspergillus) inoculated in a nutrient medium.

To evaluate the potential of fungal growth, the insulation materials were moisturized to three levels: ambient level, simulated rain, and the water holding capacity (WHC) level. The ambient moisture condition reached by subjecting the materials to 22◦C and 34-40% relative humidity for 24 hours. Simulated rain was produced by showering the specimens for 5 minutes with approximately 530 ml water followed by drying for 24 hours at ambient condition of 20◦C and 35-40% relative humidity. This process produced a moisture condition that in-between ambient and WHC and simulated at the same time an accidental wetting throughout construction building. The WHC condition was achieved by storing the samples in water for two days. The weight gain of Fungi A. niger was monitored over the inoculation period. They exhibited rapid weight from 4 to 8 days in nutrient medium, after which they reached the stationary phase of incubation **Figure 77.**)

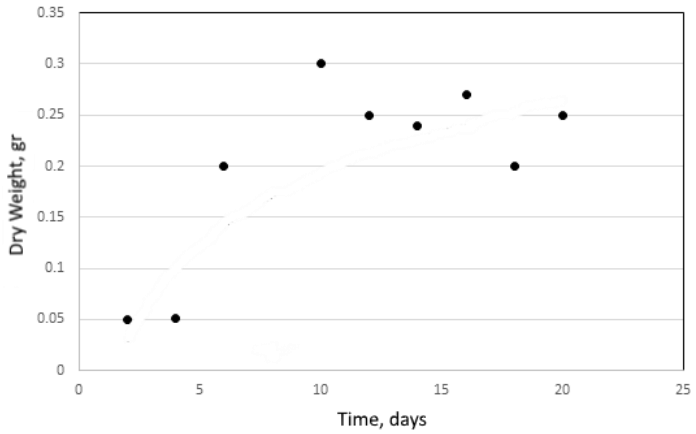

Figure 77. The growth curve of Aspergillus niger cultivated as batch cultures in nutrient medium (each data paint is the mean value of two measurements.

Fungal growth on different insulation materials was visually detected on a weekly basis following the ASTM C1336 (96) procedures. Microscopic inspections were made when fungus growth was noted; the amount of growth was classified in categories using the following scale (Figure 77.):

No growth noticed microscopically	0
Microscopical cultivation existence	1
Microscopical cultivation coating all surface	2
Macroscopical (visible to naked eye) cultivation existence	3
Macroscopical cultivation covering 75% of the surface	4

Figure 78. Classification scale for fungal growth.

An image processing tool (image J software) developed by the U.S. National Institutes of Health (NIH) was used to determine the surface area of the entire sample (A_s) and that of the area contaminated with fungal growth (A_c) (Abràmoff, Magalhães et al. 2004, Wijekoon, Goodwin et al. 2008, Schindelin, Arganda-Carreras et al. 2012) . The percentage of the surface covered by fungal growth (P_c) was calculated as (Ac/As x100) and was plotted versus the incubation time for

each insulation material. The fungal growth rating was confirmed by microscopic observation (20x) and with the aid of a digital image (taken by a 16 MP Samsung camera).

6.4 Results and Discussion

6.4.1 Water uptake

The equilibrium moisture content (EMC) test results at 85-92% relative humidity and 20°C temperature were presented in **Figure 79**. EMC reflects a dynamic equilibrium, and changes with the relative humidity and temperature by the surrounding air. The EMC of the wood- and straw-based insulation materials ranged from 5 to 6%. Treatment of wood chips with aerated slurry reduced their equilibrium moisture content by about 50%. Moisture contents exceeding 18% would encourage growth of fungi which were present in wood and straw as spores and may degenerate cellulose to create what is commonly referred to as “dry rot”. At moisture contents below 18%, fungi become dormant. If the moisture content exceeded a certain level, fungi may grow exponentially (Ashour, Georg et al. 2011, D’Alessandro, Bianchi et al. 2017).

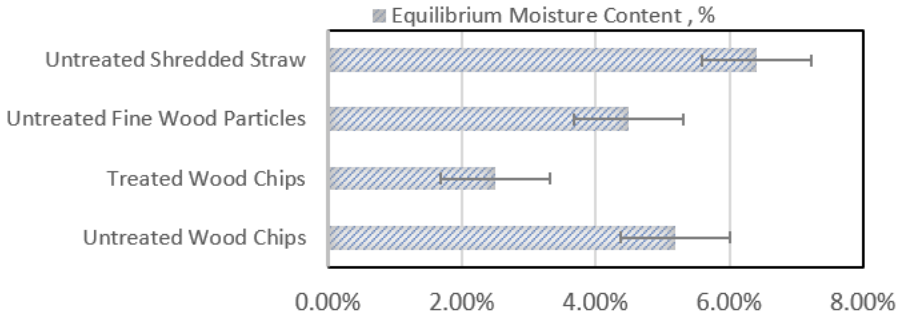

Figure 79. Equilibrium moisture contents of selected insulation materials.

The water holding capacity test results for untreated wood chips and untreated fine wood particles, measured over 65 days of submersion, were presented in **Figure 80**. Fine wood particles

had a water holding capacity of 366%, which was higher than that for wood chips (230%). Both fine wood particles and wood chips exhibited a tendency to immediately absorb some moisture.

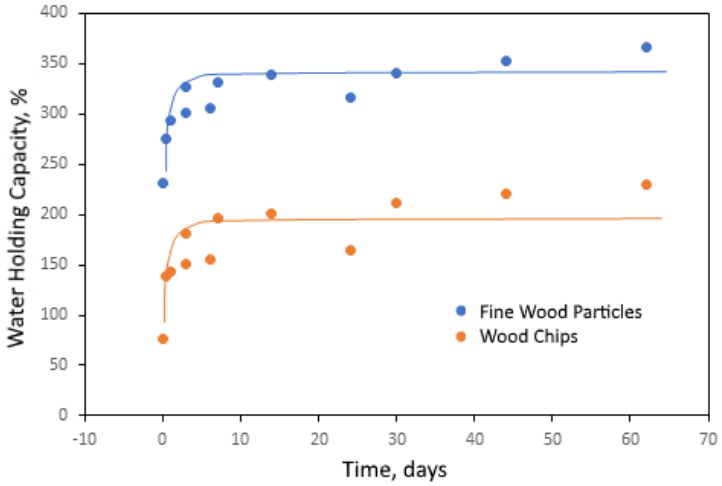

Figure 80. Water holding capacity test results for untreated wood chips and fine wood particles over a submersion period of 65 days.

6.4.2 Visual and Microscopic Observations

Visual inspections were made to evaluate the susceptibility of bio-based insulation materials to fungal growth. An example of visually notable fungal growth on the biomass insulation materials was presented in **Figure 81**.

(a) Untreated wood straw prior to (left), and 21 days after introduction of fungi (right)

Figure 81. An example of visually notable fungus growth on untreated shredded straw that was submerged in water for 48 hours and then exposed to 21 days of fungal.

The test data summarized in **Table 13**. indicate that the trends in fungal growth on untreated wood chips and untreated shredded straw are similar. Treatment of wood chips with aerated slurry was highly effective in mitigating fungal growth for all the moisture conditions considered here. After four weeks, treated wood chips in ambient and simulated rain conditions did not exhibit any indications of fungal growth. It was only after four weeks that minor fungal growth could be detected on treated wood chips in the 'water holding capacity' moisture condition. In the case of treated shredded straw, fungal growth was not observed after 3 weeks of exposure in ambient and simulated rain conditions and was minor in the 'water holding capacity' moisture condition. In ambient condition fungal growth was not observed on treated shredded straw after 4 weeks; fungal growth was present on treated shredded straw after 4 weeks in simulated rain and 'water holding capacity' moisture conditions

Table 13. Results of the visual examination of fungal growth on untreated and treated biomass insulation materials over time in different moisture conditions (ASTM C1338): ambient moisture (Amb), simulated rain (Rain), and water wetted to water holding capacity.

Average value of growth visible on surface of insulation materials												
	1 Week			2 Week			3 Week			4 Week		
	Amb	Rain	WHC	Amb	Rain	WHC	Amb	Rain	WHC	Amb	Rain	WHC
Untreated Wood Chips	0	0	0	0.5	1	1	0	1.5	2	2	3	2
Untreated Shredded Straw	0	0	0	0.5	1	1	0	1.5	2	2	3	2

6.4.3 Optical microscope

Optical microscope examination of treated wood chips (**Figure 82a**.) and treated shredded straw (**Figure 82b**.) after 4 weeks of exposure in ambient condition confirmed that treatment with aerated slurry was effective in mitigating fungal growth on these biomass insulation materials. For untreated wood chips and untreated shredded straw (**Figure 82d**.), on

the other hand, fungal colonization on surfaces was obvious under similar exposure conditions. Similar trends have been reported for cement-bonded wood particleboards made with eucalypt and ryber wood particles (Okino, De Souza et al. 2004).

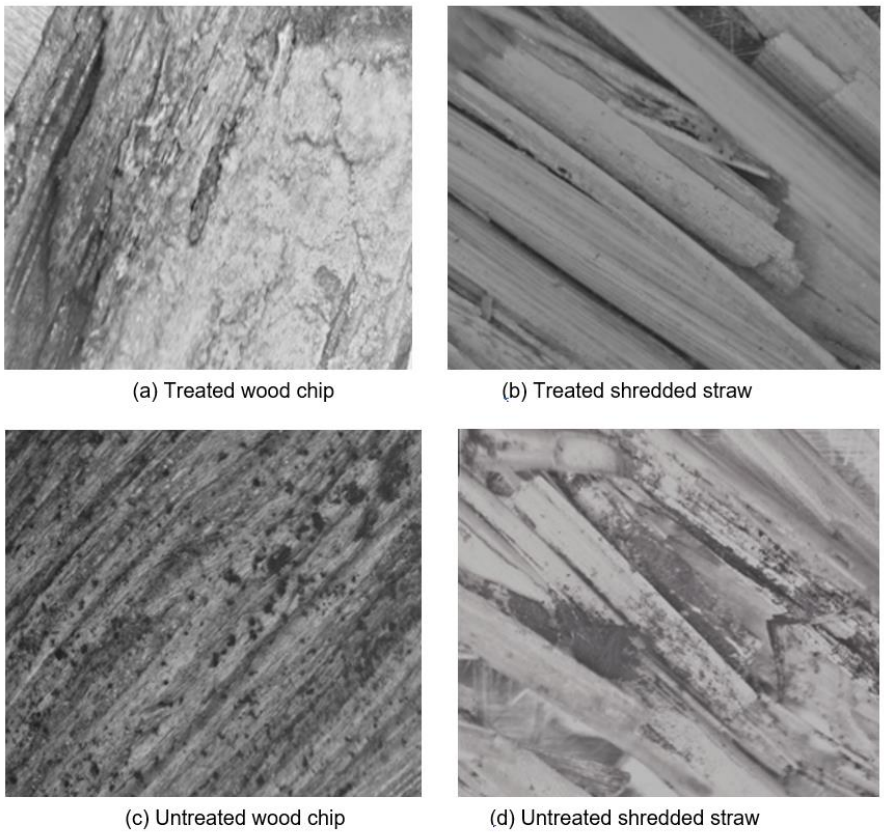

Figure 82. Optical microscope images of treated and untreated wood chips and shredded straw after 4 weeks of exposure to fungi in ambient moisture.

6.4.4 Natural Inoculation

Figure 83. showed the percent of surface area covered by fungal growth versus incubation time following natural inoculation with A. niger fungi. When untreated wood chips were subjected to high humidity prior to incubation, fungal growth was observed within the first week of incubation. When exposed directly to water, fungal growth on untreated wood chips occurred after a lag period of 25 days. This lag period can be explained by: (i) the need for moisture content

to drop below a threshold level required to support fungal growth; and (ii) washing away of some naturally inoculated fungi during the submersion period. Fungal growth did not occur on treated wood chips irrespective of the pre-exposure to high humidity or directly to water.

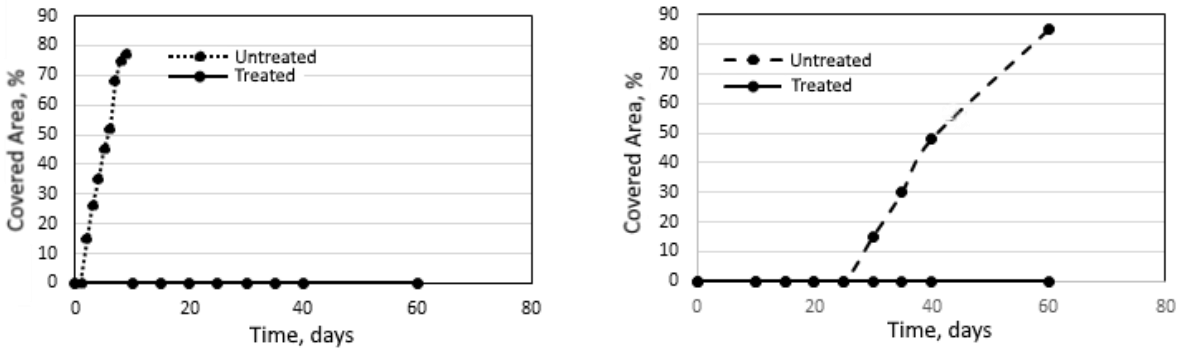

(a) High humidity exposure (b) Direct water exposure

Figure 83. Fungal coverage of untreated and treated wood chips subjected to high humidity or direct water exposure prior to incubation.

The effectiveness of aerated slurry treatment as an effective means of mitigating fungal growth on the biomass ash-based insulation could be attributed to: (i) coating of biomass and filling of its pores with aerated slurry, which produces a physical barrier against access of fungi to biomass; (ii) the relatively high pH of aerated cement slurry (pH= 11); and (iii) the amenability of the partially cured aerated slurry to further curing upon exposure to moist conditions.

6.5 Conclusions

Wood chips and particles as well as shredded straw are low-cost and abundantly available materials with desired thermal insulation qualities. Fungal growth on wood and straw in humid environments, however, is a concern. An experimental investigation was conducted in order to assess the merits of a simple and low-cost method of treating wood chips/particles and straw for control of fungal growth without while retaining their desired thermal insulation quality without

imposing a weight penalty. The following conclusions were derived based on the test data generated in this investigation.

1. Treatment of wood chips/particles and shredded straw with aerated slurry effectively mitigates fungal growth in diverse moisture and fungal growth conditions.

2. Treatment of wood and straw with aerated slurry does not produce any notable changes in the thermal insulation and bulk density due to the relatively low bulk density of aerated slurry, and the use of a relatively low dosage of aerated slurry for treatment of wood or straw.

3. The effectiveness of aerated slurry against fungal growth on wood and straw can be attributed to: (i) its ability to effectively fill the surface pores and core the surfaces of biomass, producing a physical barrier against fungal growth; (ii) the relatively high pH of aerated cement slurry; and (iii) the amenability of the partially cured slurry on wood and straw surfaces to benefit from exposure to humid environments via further curing.

REFERENCES

REFERENCES

Abràmoff, M. D., Magalhães, P. J. & Ram, S. J. Image processing with ImageJ. Biophotonics international 11, 36-42 (2004)

Almalkawi, A. et al. Physio-Microstructural Properties of Aerated Cement Slurry for Lightweight Structures. Materials 11, 597 (2018).

Almalkawi, A. T. et al. Mechanical properties of aerated cement slurry-infiltrated chicken mesh. Construction and Building Materials 166, 966-973 (2018).

Almalkawi, A. T., Hamadna, S. & Soroushian, P. One-part alkali activated cement based volcanic pumice. Construction and Building Materials 152, 367-374 (2017).

Almalkawi, A. T., Hong, W., Hamadna, S., Soroushian, P. & Al-Chaar, G. Behavior of a lightweight frame made with aerated slurry-infiltrated chicken mesh under cyclic lateral loading. Construction and Building Materials 160, 679-686 (2018).

Almalkawi, A. T., Soroushian, P. & Shrestha, S. S. Evaluation of the Energy-Efficiency of an Aerated Slurry-Infiltrated Mesh Building System with Biomass-Based Insulation. Renewable Energy 133, 797-806 (2019).

Almalkawi, A.T., Balchandra, A. and Soroushian, P., Potential of Using Industrial Wastes for Production of Geopolymer Binder as Green Construction Materials. Construction and Building Materials, 220, pp.516-524 (2019)

Ashour, T., Georg, H. & Wu, W. An experimental investigation on equilibrium moisture content of earth plaster with natural reinforcement fibres for straw bale buildings. Applied thermal engineering 31, 293-303 (2011).

Bartlett, K. H., Kennedy, S. M., Brauer, M., Van Netten, C. & Dill, B. Evaluation and a predictive model of airborne fungal concentrations in school classrooms. Annals of Occupational Hygiene 48, 547-554 (2004).

Brischke, C. & Thelandersson, S. Modelling the outdoor performance of wood products–A review on existing approaches. Construction and Building Materials 66, 384-397 (2014).

Choi, B.-M., Lanning, S. & Siebenmorgen, T. A review of hygroscopic equilibrium studies applied to rice. Transactions of the ASABE 53, 1859-1872 (2010).

D'Alessandro, F., Bianchi, F., Baldinelli, G., Rotili, A. & Schiavoni, S. Straw bale constructions: Laboratory, in field and numerical assessment of energy and environmental performance. Journal of Building Engineering 11, 56-68 (2017).

Essoua, E. G. G., Beauregard, R., Amor, B., Blanchet, P. & Landry, V. Evaluation of environmental impacts of citric acid and glycerol outdoor softwood treatment: Case-study. Journal of Cleaner Production 164, 1507-1518 (2017).

Ezeonu, I., Price, D., Simmons, R., Crow, S. & Ahearn, D. Fungal production of volatiles during growth on fiberglass. Applied and Environmental Microbiology 60, 4172-4173 (1994).

Fernández-Calviño, D. et al. Ecotoxicological assessment of propiconazole using soil bacterial and fungal growth assays. Applied Soil Ecology 115, 27-30 (2017).

Frenkel EJ, Derivaz P, inventors; Asulab AG, assignee. Watch with touch reading and setting of time functions. United States patent US 6,052,339. 2000 Apr 18.

Haas, D. et al. Assessment of indoor air in Austrian apartments with and without visible mold growth. Atmospheric Environment 41, 5192-5201 (2007).

Hernandez-Torres JM, Chen L, Cooper WR, inventors; Owens Corning Intellectual Capital LLC, assignee. Biocides for bio-based binders, fibrous insulation products and wash water systems. United States patent US 9,718,729. 2017 Aug 1.

Huang, M. & Wang, B. Evaluating green performance of building products based on gray relational analysis and analytic hierarchy process. Environmental Progress & Sustainable Energy 33, 1389-1395 (2014).

Kibert, C. J. Sustainable construction: green building design and delivery. (John Wiley & Sons, 2016).

Klamer, M., Morsing, E. & Husemoen, T. Fungal growth on different insulation materials exposed to different moisture regimes. International biodeterioration & biodegradation 54, 277-282 (2004).

Kobetičová, K. & Černý, R. Ecotoxicology of building materials: A critical review of recent studies. Journal of Cleaner Production 165, 500-508 (2017).

Lee, T. et al. Relationship between indoor and outdoor bioaerosols collected with a button inhalable aerosol sampler in urban homes. Indoor air 16, 37-47 (2006).

Li, Z. et al. Antifungal potential of Corallococcus sp. strain EGB against plant pathogenic fungi. Biological Control 110, 10-17 (2017).

Mensah-Attipoe, J., Reponen, T., Salmela, A., Veijalainen, A. M. & Pasanen, P. Susceptibility of green and conventional building materials to microbial growth. Indoor Air 25, 273-284 (2015).

Morrell, J. J. in Wood is Good 213-226 (Springer, 2017).

Murtoniemi, T., Hirvonen, M. R., Nevalainen, A. & Suutari, M. The relation between growth of four microbes on six different plasterboards and biological activity of spores. Indoor Air 13, 65-73 (2003).

Nevalainen, A. & Seuri, M. Of microbes and men. Indoor Air 15, 58-64 (2005).

Nielsen, K. F., Holm, G., Uttrup, L. & Nielsen, P. Mould growth on building materials under low water activities. Influence of humidity and temperature on fungal growth and secondary metabolism. International Biodeterioration & Biodegradation 54, 325-336 (2004).

Okino, E. Y. et al. Cement-bonded wood particleboard with a mixture of eucalypt and rubberwood. Cement and Concrete Composites 26, 729-734 (2004).

Palumbo Fernández, M. Contribution to the development of new bio-based thermal insulation materials made from vegetal pith and natural binders: hygrothermal performance, fire reaction and mould growth resistance. (2015).

Palumbo, M., Lacasta, A., Navarro, A., Giraldo, M. & Lesar, B. Improvement of fire reaction and mould growth resistance of a new bio-based thermal insulation material. Construction and Building Materials 139, 531-539 (2017).

Palumbo, M., Navarro, A., Giraldo, P., Lesar, B. & Lacasta, A. Performance Of Biobased Insulation Board From Crop By-Products And Natural Gums. (2015).

Piemonte, V., Francioni, F., Capocelli, M. & Prisciandaro, M. Biodegradation Of Acrylic Paints: Process Modelling Of Biocide Effect On Biomass Growth At Different Temperatures. Brazilian Journal of Chemical Engineering 34, 557-566 (2017).

Portnoy, J. M., Kwak, K., Dowling, P., VanOsdol, T. & Barnes, C. Health effects of indoor fungi. Annals of Allergy, Asthma & Immunology 94, 313-320 (2005).

Rao, C. Y., Burge, H. A. & Chang, J. C. Review of quantitative standards and guidelines for fungi in indoor air. Journal of the Air & Waste Management Association 46, 899-908 (1996).

Rautiala, S., Kasanen, J. P., Raunio, P., Rantamäki, J. & Kalliokoski, P. The Relationship between Measured Moisture Conditions and Fungal Concentrations in Water-Damaged Building Materials. Indoor Air 10, 111-120 (2000).

Schindelin, J. et al. Fiji: an open-source platform for biological-image analysis. Nature methods 9, 676-682 (2012).

Schmidt, O. Wood and tree fungi: biology, damage, protection, and use. (Springer Science & Business Media, 2006).

Sedlbauer, K. Prediction of mould fungus formation on the surface of and inside building components. Fraunhofer Institute for Building Physics (2001).

Spiegel, R. & Meadows, D. Green building materials: a guide to product selection and specification. (John Wiley & Sons, 2010).

Viitanen, H. et al. Moisture and bio-deterioration risk of building materials and structures. Journal of Building Physics 33, 201-224 (2010).

Wijekoon, C., Goodwin, P. & Hsiang, T. Quantifying fungal infection of plant leaves by digital image analysis using Scion Image software. Journal of Microbiological Methods 74, 94-101 (2008).

Winandy, J. & Morrell, J. Improving the utility, performance, and durability of wood-and bio-based composites. Annals of Forest Science 74, 25 (2017).

Yang, C. S. & Li, D. W. Ecology of fungi in the indoor environment. Sampling and analysis of indoor microorganisms. Hoboken, New J ersey: John Wiley & Sons, Inc, 191-214 (2007).

Yang, V. W. & Clausen, C. A. Antifungal effect of essential oils on southern yellow pine. International biodeterioration & biodegradation 59, 302-306 (2007).

CHAPTER 7: ONE-PART ALKALI ACTIVATED CEMENT BASED VOLCANIC PUMICE

This chapter was first published as "One-part alkali activated cement based volcanic pumice." Almalkawi, Areej T., Sameer Hamadna, and Parviz Soroushian Construction and Building Materials 152 (2017): 367-374.

7.1 Introduction

Conventional “two-part” alkali activated binders are synthesized via alkali-activation of solid aluminosilicate feedstocks (e.g., metakaolin, coal fly ash and ground granulated blast furnace slag) with highly alkaline solutions (e.g., sodium silicate and sodium hydroxide) (Alonso and Palomo 2001, Lee and Van Deventer 2002, Lecomte, Liégeois et al. 2003, Duxson, Fernández-Jiménez et al. 2007, Kong, Sanjayan et al. 2007, Andini, Cioffi et al. 2008, Bernal, Rodríguez et al. 2012, Heah, Kamarudin et al. 2012, Lizcano, Gonzalez et al. 2012, Deb, Nath et al. 2014). These two-part alkali activated binders, comprising largely of alkali aluminosilicate hydrates, offer important advantages over alternative cementitious binders in terms of sustainability, thermos-mechanical performance and chemical stability. The two-part nature of alkali activated binders, however, challenges their transition to mainstream construction applications. The need to handle highly caustic solutions, and the requirement to mix these caustic solutions (in lieu of water) with solids constitute setbacks in their large-scale implementation.

Efforts have been undertaken in recent years to develop “one-part” hydraulic cement formulations which, upon addition of water, undergo hydration reactions which yield the desired alkali aluminosilicate hydrate structure of conventional alkali activated binders(Hajimohammadi,

Provis et al. 2008, Hajimohammadi, Provis et al. 2010) . These efforts can be categories into two groups: (i) heat treatment of the blend of raw materials (aluminosilicate precursor and alkalis in solid form) to yield a compounded and activated hydraulic cement; and (ii) simple blending of the raw materials in dry form. The second category, however, may not be a viable option because the resultant 'cements' embody caustic solids in raw form, which could generate significant heat upon the addition of water. These 'one-part cements' could also have limited shelf life due to the affinity of alkalis for the humidity in air. The first group, which seems to be more viable, requires input of relatively high thermal energy to bring about compounding and activation effects; this energy consumption, however, compromises the sustainability of the resultant hydraulic cements. The long-term durability of these "one-part" cements needs to be verified (Muntingh 2006, Provis and Van Deventer 2009, Van Deventer, Provis et al. 2012).

The primary focus of the work reported herein was on development of one-part alkali activated cements formulated with natural volcanic tuff as aluminisilicate precursor (Areej Almalkawi 2017). This work emphasized the sustainability of the resultant hydraulic cement by employing a combination of calcination of volcanic tuff at moderate temperature followed by mechanochemical processing of the blend of volcanic tuff with other raw materials to produce the hydraulic cement.

Volcanic tuffs offer a wide range of reactivity depending upon their degree of crystallinity and mineralogy (Nesbitt and Young 1984). Reactive volcanic tuffs have been used for production of historic concrete. Early stone buildings have made use of more reactive volcanic tuffs together with lime to produce relatively strong and durable mortars, some of which have survived few centuries of exposure to weathering and seismic effects (Shi and Day 1993, Goldsworthy and ZHU

2009, Allen 2015) . Aluminosilicate precursors such as reactive volcanic tuff (or ash) can undergo dissolution and precipitation processes in lime solution (Jha and Singh 2011, Mason 2012, Al-Zboon, Al-smadi et al. 2016, Djobo, Elimbi et al. 2016, Tekin 2016), which yield calcium aluminosilicate hydrate (C-A-S-H) structures with desired binding attributes (Walkley, San Nicolas et al. , Nath and Sarker 2015) . Considering the variability in the reactivity of different volcanic tuffs, this investigation resorted to thermal activation of the tuff at moderate temperatures in order to achieve viable levels of reactivity prior to processing of the tuff and other raw materials into a hydraulic cement.

7.2 Experimental Program

7.2.1 Materials

Natural pumice was obtained from HESS Pumice® mining, Idaho (United States). Some properties of this pumice, reported by the manufacturer, are presented in **Table 14**. The other raw materials used for production of the pumice-based hydraulic cement included lime, Sodium sulfate and Soda Ash (Na_2CO_3) as chemical reagents, and gypsum as additive. Soda ash as well as sodium sulfate have been shown in past investigations to accelerate the hydration process of lime-aluminosilicate binders(Allahverdi and Ghorbani 2006) . While conventional alkali activated binders are obtained via alkali activation of aluminosilicate precursors without a focus on the addition of lime, the lime constituent of this hydraulic cement produces a hybrid structure of (Ca, Na) aluminosilicate hydrates and probably calcium silicate hydrate which is amenable to room-temperature curing. This hybrid chemistry, when used in the context of a one-part hydraulic cement, also seems to yield hydration products with improved moisture resistance.

Table 14. Some properties of the pumice used as raw material (aluminosilicate precursor) in synthesis of one-part hydraulic cement.

Hardness (Mohs)	pH	R radioactivity	Crystalline $Si0_2$	Softening Point	GE Brightness	Specific Gravity
6	7.2	0	None Detected	900°C	84	2.35

7.2.2 Formulations of Raw Materials and Their Processing into Hydraulic cements

The formulations of raw materials considered in this investigation for synthesis of hydraulic cements are introduced in These formulations were partly based on those developed in the literature on two-part alkali activated binders which employ volcanic tuff in powder form: lime weight ratios in the 0.6-0.75: 0.3-0.23 range(Cultrone, Sebastian et al. 2005, Chatterji, Brenneis et al. 2016) .

Each formulation was blended and heat-treated at 700°C for four hours (with a heating rate of 10°C/min) in order to improve its reactivity. This temperature was selected after trial studies involving heat treatment at different temperatures. After heat-treatment, the product was allowed to cool down to room temperature over several hours (with the furnace turned off).

After cooling, the heat-treated blends were ball-milled for the purpose of size reduction and mechanochemical processing. The ball-milling parameters are presented in **Table 15**. A ceramic jar (5.6 L) ball mill was used in this investigation operated at an optimum rotational speed as a function of the internal diameter of the jar and diameter of the steel balls(Watanabe 1999). This process yielded the hydraulic cements formulated with pumice for construction applications. Transformation of raw materials into hydraulic cement, and the change in crystalline structure caused by ball-milling support the mechanochemical effects rendered by this milling process.

Table 15. Mechanochemical processing (milling) conditions of the heat-treated blends of raw materials (three sizes of steel balls were used in equal weights).

Steel Ball Diameter (mm)			**Steel Ball-to-Material Weight Ratio**	**Milling duration (hr)**
Large	Medium	Small		
76.2	25.4	12.7	10	3

7.2.3 Characterization Methods

The hydraulic cement was used to prepare mortar mixtures. The mortar mix designs considered in this investigation are introduced in **Table 16**. These mixtures were prepared using a mortar mixer. Fresh mixtures were cast and consolidated in 50-mm cube molds, demolded after 24 hours (during which they were stored under wet burlap), sealed and stored at 90% relative humidity and room temperature for compression testing at 7 and 14 days of age. Most mortar mixtures evaluated in this work had a natural sand-to-indigenous hydraulic cement ratio of 2.5, and water/cement ratio of 0.5 (for achieving desired workability). The compressive strength of cube specimens was measured using a LLOYD EZ20 universal testing machine at a crosshead speed of 0.1 mm/min. Ten replicates specimens prepared from each mix were tested in compression, and the mean values are reported as compressive strength

.

Table 16. The formulations of raw materials considered for synthesis hydraulic cements.

Mix	Precursor (pumice) Wt%	Chemical Reagent(s)	Water/binder ratio	Sand
1	60	40 (Sodium Sulfate)	0.6	3
2	65	0.35 (Soda Ash)	0.6	3
3	60	0.2 (lime)+ 0.20 (Soda Ash)	0.6	3
4	75	0.25 (lime)	0.6	3
5	75	0.25(Sodium Sulfate)	0.6	3
6	60	0.2 (Sodium Sulfate) + 0.2 (Gypsum)	0.6	3
7	75	0.20 (lime) + 0.05 (Gypsum)	0.6	3
8	75	0.20 (lime) + 0.05 (soda ash)	0.71	3
9	65	0.35(lime)	0.71	3
10	20	0.2(lime)+0.6 (gypsum)	0.74	3
11	85	0.15 (Sodium Sulfate)	0.6	3
12	50	0.5 (lime)	0.6	3
13	60	0.3(Sodium sulfate) + 0.1 (lime)	0.6	3

The chemical composition of raw pumice was determined using X-ray fluorescence (XRF) spectroscopy. Phase compositions of the samples were examined by X-ray diffraction (XRD) spectroscopy. FTIR spectroscopy was conducted in the 4000–400 cm^{-1} range to investigate the chemical environment (bond structure) of the as-received pumice and the synthesized alkali activated cement based on pumice.

The raw (untreated) pumice and the end products of alkali activation were subjected to SEM observation for evaluating their microstructural features. SEM observations were carried out on a JCM-5000 NeoScope™ at an accelerating voltage of 10-15 kV using a secondary electron (SE) detector. SEM observations were made on the pumice external surface and on the fractured

surfaces of hydrated paste at 28 days of age. Samples were sputtered with gold prior to SEM observations.

Thermogravimetric analysis (TGA) was performed by heating the samples at a rate of 10°C min^{-1} in a dry air flow between 50°C and 950 °C.

The exothermic heat of hydration of the hydraulic cement was measured using a calorimeter (TAM Air Isothermal Calorimeter). In this test, about 25g of freshly mixed paste was weighed into a flask, which was then capped and placed in the calorimeter. Heat generation caused by exothermic hydration reactions was monitored over 18 hours.

7.3 Test Results and Discussion

7.3.1 Particle Size Distribution

The visual appearance and particle size distribution (produced via laser granulometry) of the pumice used in this investigation are presented in **Figure 84**. The median particle size of the pumice was 9.8 µm, and its specific surface area was 300 m^2/kg .

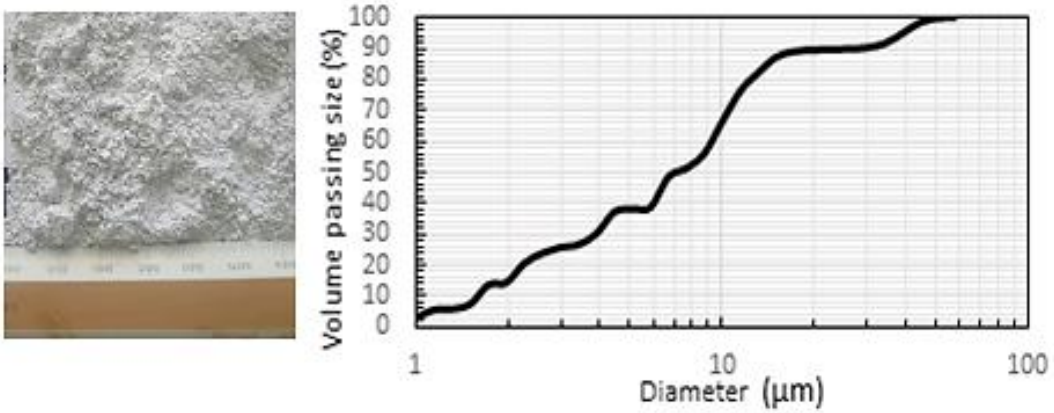

Figure 84. The visual appearance and the particle size distribution of the pumice used in this investigation.

7.3.2 Chemical Composition

Table 17. presents the chemical composition, obtained via XRF spectroscopy, and loss on ignition of the pumice used in this investigation. The results indicate that the pumice used here is rich in SiO_2 and K_2O; its Al_2O_3 content is near the lower range expected for pumice. As an aluminosilicate material, pumice (alone or in combination with other minerals) can be transformed into inorganic (cementitious) binders via dissolution and precipitation steps using different alkali hardeners or reactive ingredients.

Table 17. Chemical composition of the pumice used in the experimental work.

Chemical compound	Fe_2O_3	SiO_2	Al_2O_3	CaO	K_2O	MgO	LOI %
	1.1	76.2	13.5	0.8	1.8	0.05	5

7.3.3 Compressive Strength of Mortar

The 7-day compressive strength test results summarized in **Figure 85a.** indicate that, with heat treatment of raw materials at a relatively low temperature of 700^oC, satisfactory compressive strengths (up to 22 MPa) can be achieved at 28 days of age. Mix 9 (Pumice activated with lime) was observed at age 7 and 28 days in dry and wet conditions) as shown in **Figure 85b.** . Results indicated that Mix9 achieved average 7-days compressive strength is 5 MPa and its compressive strength increases with time to reach around 22 MPa after 28 days with moisture stability with average wet compressive strength about 20 MPa.

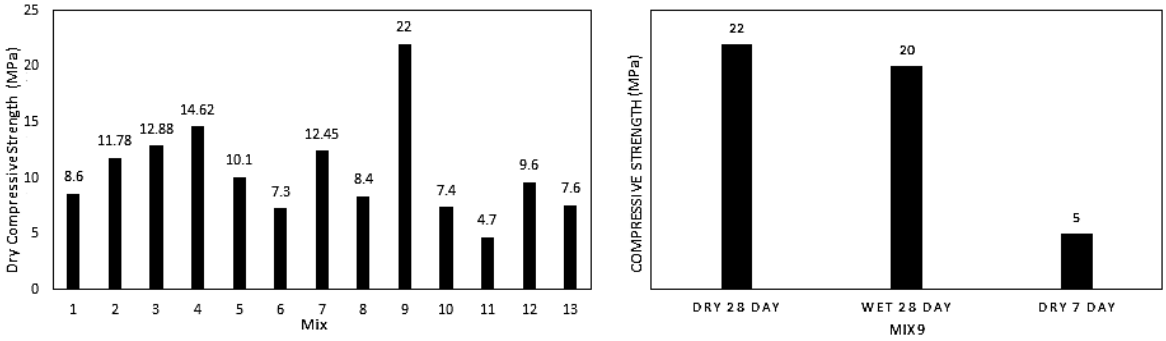

(a) 28-day compressive strength test results (b) Effects of age and moisture condition on Mix 9

Figure 85. Compressive strength test results.

7.3.4 Mineralogy

The mineralogical compositions of the pumice and the feed sample before and after mechanochemical processing, obtained via x-rat diffractometry, are presented in **Figure 86.** The XRD pattern of as-received pumice exhibits a major amorphous hump, centered at 2θ = 25°. X-ray diffraction patterns of the feed sample (un-milled) and the milled sample have general similarities but some differences. The milled alkali activated cement exhibits both amorphous and crystalline phases, which is characteristic of the glassy phase in volcanic materials (Djobo, Elimbi et al. 2016, Djobo, Elimbi et al. 2016). This pattern points at the presence of an amorphous phase, which gives a broad band at 2θ=20-28°, together with minerals, Manitobaite and Melanterite identified by sharp diffraction peaks. The appearance of Quartz after milling could be attributed to the breakdown of covalent bonds of the silicate network of the volcanic tuff (Si–O^-, Ca–O^- and Al–O^-). The presence of moisture in atmosphere enables transformation of Si–O^- to silanol groups (Si–OH) which can form Quarts through polycondensation/crystallization (Kalinkina, Kalinkin et al. 2001, Djobo, Elimbi et al. 2016).

In addition, a sharpening of the XRD peaks of AAC after milling is noted around 35°. Prior to milling, one can observe the nucleation of mini shoulders in around 2θ= 65° and 2θ=73°. These nuclei grew into well-identified crystals (Melantrite) upon milling. In other words, thermal treatment of the blend of raw materials (prior to milling) led to nucleation of Melantrite, and mechanochemical treatment (milling) led to growth of this crystalline structure (Wang, Xue et al. 2000, Hua and Li 2007, Charoonsuk and Vittayakorn 2017, Senna 2017).

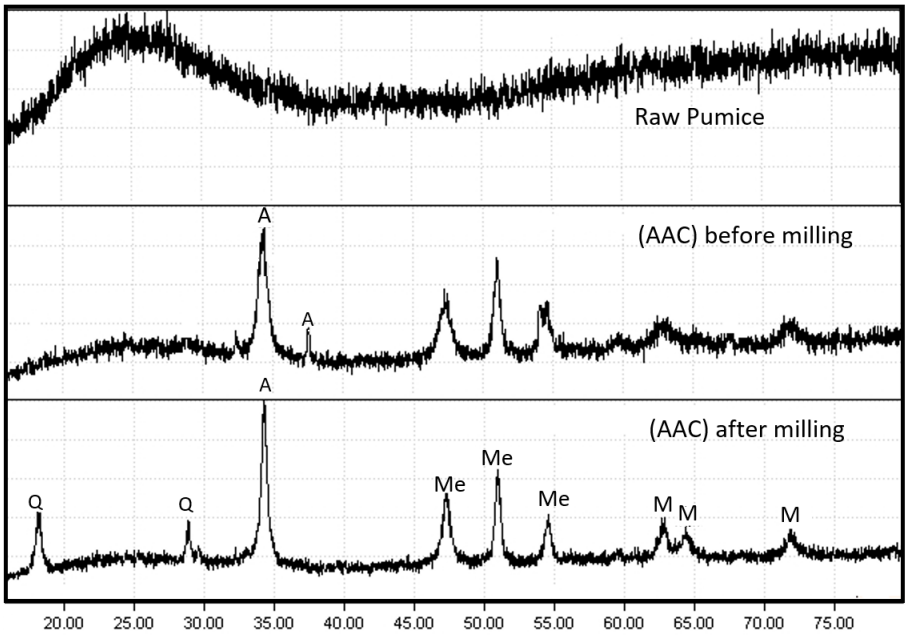

Figure 86. XRD patterns of the raw pumice, and alkali activated cements formulated with pumice. M (Manitobaite); A (Alite); Me (Melanterite); Q (quartz).

7.3.5 Chemical Environment

Figure 87. presents the FTIR spectra of the raw pumice and the hydration products of the cement formulated (and processed) with this pumice. For raw pumice, the characteristic peak observed at 1032 cm^{-1} may be attributed to the asymmetric vibration of Si-O-Si that generally occurs in the 1000–1044 cm^{-1} region (Gök, Göde et al. 2006, Li, Yang et al. 2009).

The prevalence of asymmetric vibration of Si-O-Si over its stretching vibration points at the relatively low degree of polymerization of silica tetrahedra in this pumice (Chindaprasirt, Jaturapitakkul et al. 2009). The presence of silica as a chemical constituent of pumice is in line with the detection of the asymmetric vibration of Si-O-Si detected in the FTIR spectrum of pumice. The relatively weak peaks of raw pumice between 1200-1400 cm^{-1} can be attributed to the asymmetric stretching vibrations of Al–O/Si–O bonds(Kani and Allahverdi 2009, Li, Yang et al. 2009). The peaks at 1600, 2366 and 2978 cm^{-1} in the pumice spectrum correspond to stretching vibration of O-H and bending vibration of H–O–H groups in the water molecules contained in pumice (Chabiron, Pironon et al. 2004).

The broadened peak in the 641-1400 cm^{-1} region of the FTIR spectrum of the hydrated paste may be due to the merging of IR peaks corresponding to the other metal oxides present in pumice (AC130). The Si–O–Si/Si–O–Al bending band can be observed at 641 cm^{-1} in the FTIR spectrum cement hydrates(Li, Yang et al. 2009). These bands are common in aluminosilicate precursors and provide an indication of the degree of amorphization of the material, since its intensity is lower at a higher degree of crystallinity (Fomina, Strokova et al. 2013). In the spectrum generated for cement hydrates, the peak at 2366 cm^{-1} could correspond to the formation of carbonates in both of raw pumice and the hydrated paste.

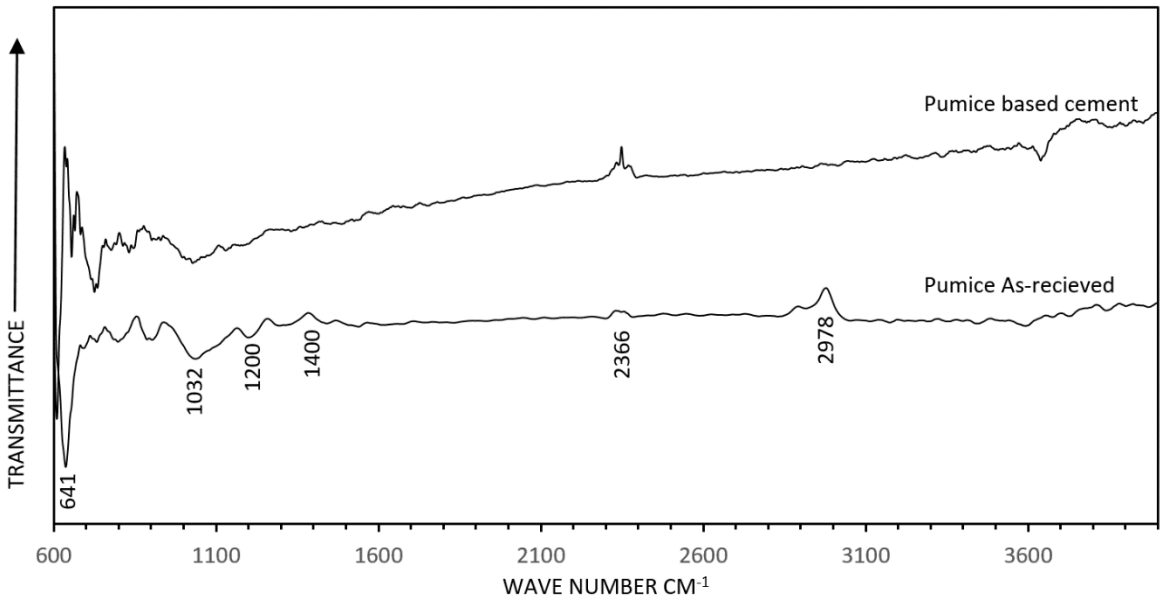

Figure 87. FTIR spectra for raw pumice (a) and the hydration products of the cement formulation (and processed) using pumice (Mix 9).

7.3.6 Microstructural Characteristics

Scanning electron microscope images depicting the micro morphological features of the original pumice, the non-hydrated cement, and the resultant hydration products (at 28 days of age) are presented in **Figure 88**. Pumice (**Figure 88a.**) seems to comprise larger particles that are covered with finer particles ranging in size from few micrometers down to sub-micrometer dimensions. Measurements made on the particle size distribution of pumice (presented later) confirmed this observation.

An SEM image of the hydration products of the hydraulic cement is presented in **Figure 88c.** (taken from a fractured surface of the hydrated binder). Based on the observations made on the raw pumice (**Figure 88b.**), some non-hydrated cement particles could be identified among hydration products (marked by an arrow in **Figure 88c.**). This observation that some non-reactive phases were inherited from the parent material by the hydration products has also been made

by other investigators(He, Zhang et al. 2012, He, Jie et al. 2013) . An SEM image (at lower magnification) taken of the exterior surface of hydration products is presented in **Figure 88d**.). The microstructure is observed to be porous, exhibiting some shrinkage microcracks. While these microcracks may be caused by the excess drying of specimens for the purpose of scanning electron microscopy, one should be aware of the fact that some alkali activated binders exhibit larger shrinkage than binders based on ordinary Portland cement(Van Jaarsveld, Van Deventer et al. 1997, Wallah 2009) .

The porosity and pore size of the alkali activated binder observed here seem to be larger than those found in ordinary Portland cement paste. This finding point at the need to reduce the water/binder ratio, which could be accomplished using water-reducers. Special processing techniques employing vacuum or applying pressure to remove excess water and air have been used to produce a less porous polymeric microstructure (Živica, Balkovic et al. 2011, He, Jie et al. 2013).

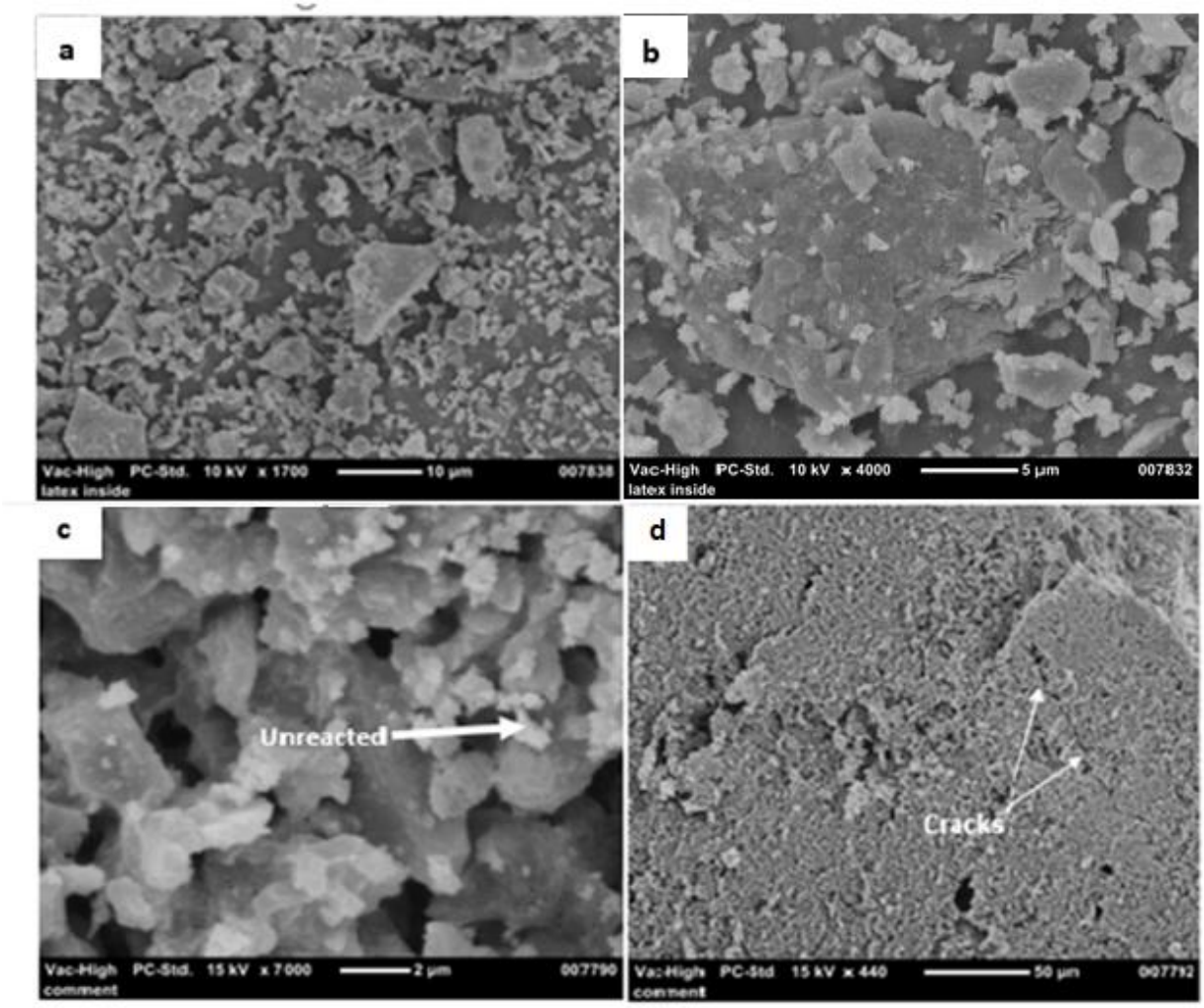

Figure 88. SEM observation for microstructure of raw pumice (a,b), and hydration products of alkali activated cement based on pumice (c,d).

7.3.7 Thermogravimetric Analysis

The thermogravimetric and differential thermal analysis data produced for raw pumice are presented in **Figure 89**. The measured value of weight loss for pumice at 900°C is 7 wt.%. Most of the weight loss occurs below 550°C, which presumably results mostly from the water content of pumice. As a hydrophilic material, pumice absorbs water (AC130). The main weight loss before 550°C from raw pumice was a result of water loss due to both evaporations of free water and condensation/polymerization of T–OH groups (T = Si, Al). The presence of water can

be confirmed using the FTIR spectrum of **Figure 86.** that exhibits O–H vibration bands at 2366 and 2978 cm^{-1}. Moreover, the DTA curve for raw pumice in **Figure 90.** exhibits endothermic peaks due to removal of adsorbed moisture and OH species attributed to metal oxides as well as volatile organic impurities existing at small concentrations (Mourhly, Khachani et al. 2015).

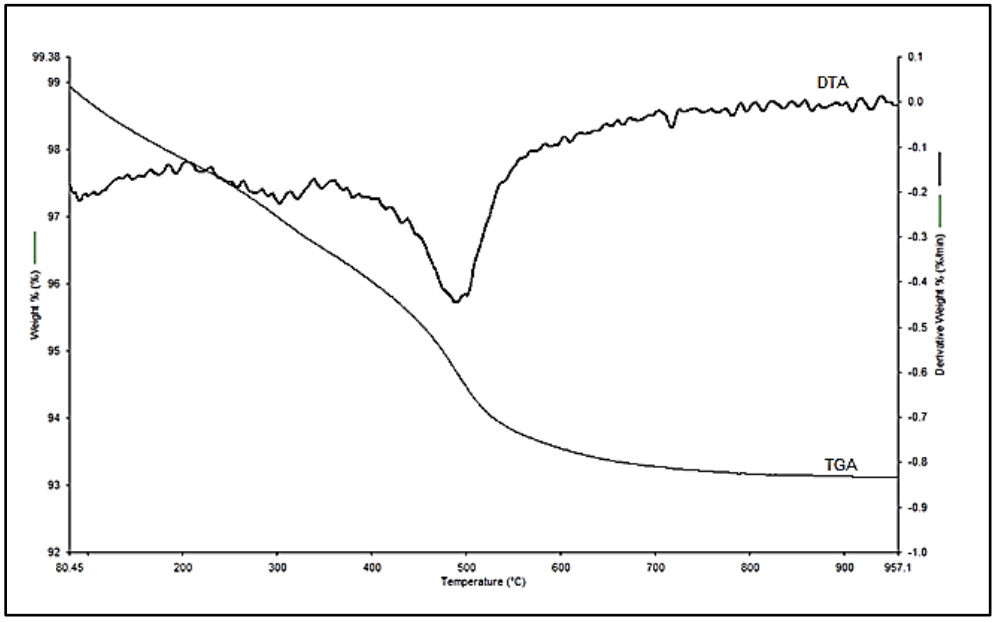

Figure 89. Thermogravimetry and differential thermal analysis data for the raw pumice used as aluminosilicate precursor.

The thermogravimetry and differential analysis data produced for the alkali activated binder are presented in **Figure 90**. A minor weight loss of 0.5% is observed in the 400-430°C temperature range which is typically indicative of the reactivity of volcanic tuff (Tchakouté, Kong et al. 2015). The second major weight loss occurs in the 450-680°C temperature range, that can be assigned to the loss of the chemically bond water present in the alkali activated cement structure (Djobo, Tchakouté et al. 2016) . A DTA thermogram of paste resulting from hydration of the cement formulated with pumice exhibits an endothermic reaction in the range of 400-450°C, this peak is correlated to the loss of physically adsorbed water from the surface and

matching with weight loss in TGA curve. The gain in weight beyond 750°C may point possible oxidation phenomena that might include allotropic phase transformation of iron oxides (Wen, Li et al. 2004, Leonelli, Kamseu et al. 2007), which could occur due to leakage of oxygen into the test chamber. Re-adsorption of some CO_2 released from the specimen at elevated temperature could be another factor causing the observed weight gain.

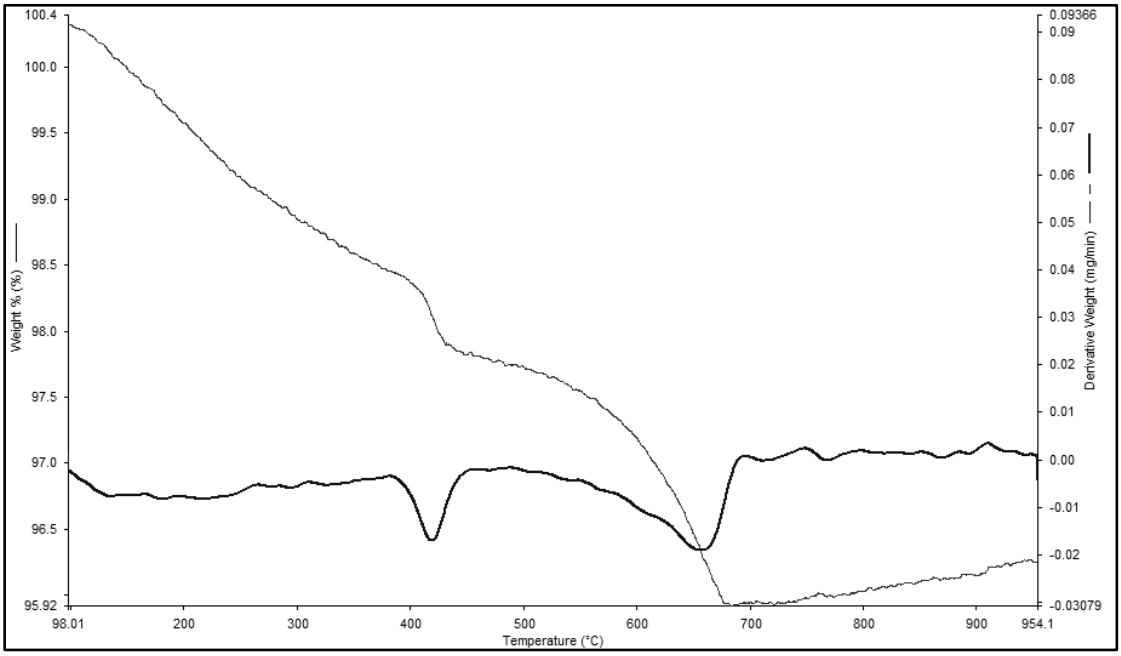

Figure 90. Thermogravimetric curve of alkali activated cement based on pumice after thermal activation.

7.3.8 Isothermal conduction calorimetry measurement

The calorimetry measurement was used herein to evaluate the heat released during alkaline activation of volcanic pumice with three different activators (sodium sulphate, lime and sodium carbonate) at 27°C. The results, depicted in **Figure 91.**, show initial exothermic peaks occurring in less than 2 hours. These initial peaks correspond to the dissolution-precipitation of the reactive phases at 27°C (Djobo, Elimbi et al. 2016, Djobo, Elimbi et al. 2016), including

aluminate and silicate species (Yip, Lukey et al. 2004, Buchwald, Hilbig et al. 2007, Li and Liu 2007, Kumar, Kumar et al. 2010) . The rapid deceleration after the first peak indicates that the wetting process and the initial dissolution and reaction phenomena slow down. This is followed by the appearance of a second peak for the paste activated with sodium sulphate (after about 40 minutes) and with lime (after about 5 hours). When lime is used as the chemical reagent, a weak shoulder appears at about 2 hours, that could be due to hydration of metal oxides in pumice only, or reactions attributed to the instant sorption of lime and formation of nucleation sites on pumice particles (Langan, Weng et al. 2002, Kumar, Kumar et al. 2010).There is a very late (at about 10 hours) trend towards rising of the rate of heat release, but no peak prior to that, when sodium carbonate is used as the chemical reagent. The later stages of dissolution occur simultaneously with polymerization reactions, both of which contribute to heat generation.

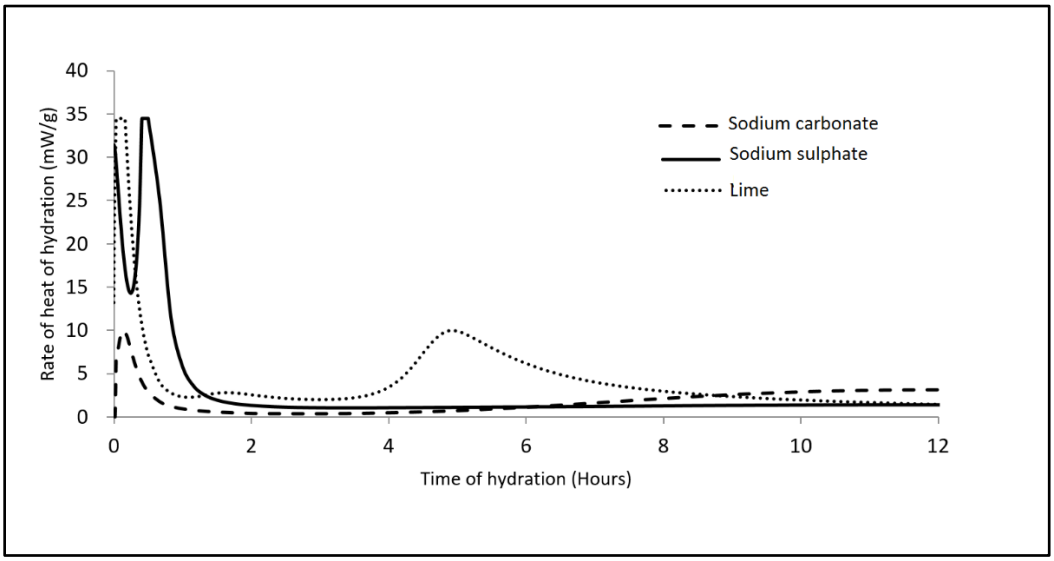

Figure 91. Effect of chemical reagents on heat released during geopolymerization reaction for24 hour at 27°.

As seen in these curves in **Figure 92**. , an exothermic peak appears immediately when water is mixed with raw pumice which can be attributed to the instant sorption of activation

solution on the surface of raw material particles and the ensuing dissolution of the solid aluminosilicate and aluminate precursors (Kani, Allahverdi et al. 2017). An additional exothermic peak (after 2 hours) for the blend of raw materials (before heating or milling), which may be linked to the formation of a transient hydrate product. Appearance of second peak after 5 hours for alkali activated cement subjected to milling (mechanochemical synthesis) can be attributed to partial replacement of SiO_4 tetrahedra of the silicate network of the volcanic tuff with AlO_4 tetrahedra, which decreases the length of silicate chain and leads to the formation of Al-substituted phase (Djobo, Elimbi et al. 2016, Djobo, Elimbi et al. 2016); this is consistent with the XRD pattern for AAC after milling. After a period of time (7 hours) for all mixtures, the process reached an apparent thermally steady state, during which the freshly formed small gel units are probably continuously transform into larger-scale networks by local reorganization (White, Provis et al. 2013)

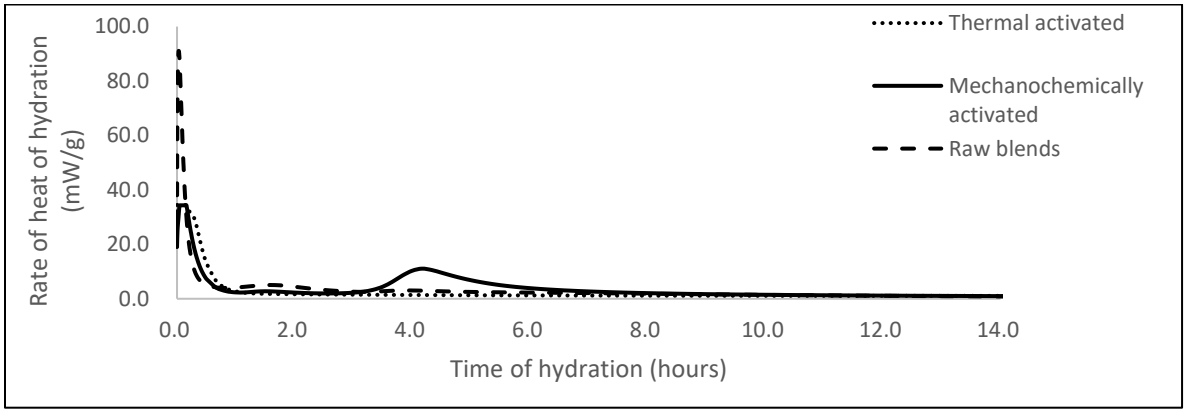

Figure 92. Effect of the activation methods of volcanic tuff on heat released.

7.4 Conclusion

These geopolymer precursors polymerize upon the addition of water, forming geopolymers with acceptable compressive strength development rates and final strengths. These geopolymer precursors polymerize upon the addition of water, forming geopolymers with acceptable compressive strength development rates and final strengths.

A volcanic tuff (pumice) was used together with naturally occurring sources of alkali and alkaline earth metals for production of a hydraulic cement. The volcanic tuff was activated at moderately elevated temperatures, and was transformed, together with other raw materials, into a hydraulic cement via a simple milling action. Different raw materials formulations with various sources of alkali and alkaline earth metals were evaluated. The resultant hydraulic cements were characterized through assessment of their physical, chemical and mineralogical characteristics, and strength development attributes upon hydration. The following conclusions were derived based on this experimental investigation.

1. Mechanochemical processing of the blend of pumice and other raw materials produced a hydraulic cement with modified amorphous constituents, which also exhibited some crystalline peaks corresponding to partially soluble hydroxides and carbonates.
2. The chemical bond environment of hydration products suggests that alkali aluminosilicate hydrates constitute the primary binders formed upon hydration of the hydraulic cements produced in this work.
3. The microstructure of hydration products points at the formation of a continuous structure of hydrates embodying interconnected micro-scale pores.
4. The hydration rates of the hydraulic cements produced with different sources of alkali and

alkaline earth metals vary significantly. The exothermic heat release peaks occurred at times ranging from less than 1 hour to several hours, depending upon the alkali/alkaline earth metal source.

5. Some of the hydraulic cements produced in the project exhibited desired strength development characteristics and moisture resistance upon hydration at room temperature. Viable strength development characteristics were achieved when pumice was formulated with a proper concentration of lime. Formulation of pumice with a combination of lime and soda ash also promises to produce, with further refinements, viable strength development characteristics.

The work reported herein was funded by the U.S. Army Grant No. W9132T-16-C-0003. Authors are thankful to Dr. Ghassan Alchaar, the Project Manager, for his guidance and encouragement.

REFERENCES

REFERENCES

AC130, I., Acceptance Criteria for Prefabricated Wood Shear Panels. ICC Evaluation Service, Inc., Whittier, CA, 2004.

Allahverdi, A. and J. Ghorbani, Chemical activation and set acceleration of lime-natural pozzolan cement. Ceramics Silikaty, 2006. **50**(4): p. 193.

Allen, G., Hydraulic lime mortar for stone, brick and block Masonry: a best practice guide. 2015: Routledge.

Alonso, S. and A. Palomo, Alkaline activation of metakaolin and calcium hydroxide mixtures: influence of temperature, activator concentration and solids ratio. Materials Letters, 2001. **47**(1): p. 55-62.

Al-Zboon, K.K., B.M. Al-smadi, and S. Al-Khawaldh, Natural volcanic tuff-based geopolymer for Zn removal: adsorption isotherm, kinetic, and thermodynamic study. Water, Air, & Soil Pollution, 2016. **227**(7): p. 1-22.

Andini, S., et al., Coal fly ash as raw material for the manufacture of geopolymer-based products. Waste management, 2008. **28**(2): p. 416-423.

B. Langan, K. Weng, M. Ward, Effect of silica fume and fly ash on heat of hydration of Portland cement, Cem Concr Res 32 (7) (2002) 1045–1051.

Bernal, S.A., et al., Activation of metakaolin/slag blends using alkaline solutions based on chemically modified silica fume and rice husk ash. Waste and Biomass Valorization, 2012. **3**(1): p. 99-108.

Buchwald, A., H. Hilbig, and C. Kaps, Alkali-activated metakaolin-slag blends—performance and structure in dependence of their composition. Journal of materials science, 2007. **42**(9): p. 3024-3032.

Chabiron, A., J. Pironon, and D. Massare, Characterization of water in synthetic rhyolitic glasses and natural melt inclusions by Raman spectroscopy. Contributions to Mineralogy and Petrology, 2004. **146**(4): p. 485-492.

Charoonsuk, T. and N. Vittayakorn, Soft-mechanochemical synthesis of monodispersed BaZrO 3 sub-microspheres: Phase formation and growth mechanism. Materials & Design, 2017.

Chatterji, J., D.C. Brenneis, and C.L. Keys, Geopolymer cement compositions and methods of use. 2016, Google Patents.

Chindaprasirt, P., et al., Comparative study on the characteristics of fly ash and bottom ash geopolymers. Waste Management, 2009. **29**(2): p. 539-543.

Cultrone, G., E. Sebastian, and M.O. Huertas, Forced and natural carbonation of lime-based mortars with and without additives: Mineralogical and textural changes. Cement and Concrete Research, 2005. **35**(12): p. 2278-2289.

Deb, P.S., P. Nath, and P.K. Sarker, The effects of ground granulated blast-furnace slag blending with fly ash and activator content on the workability and strength properties of geopolymer concrete cured at ambient temperature. Materials & Design (1980-2015), 2014. 62: p. 32-39.

Djobo, J.N.Y., et al., Gel Composition and Strength Properties of Alkali-Activated Oyster Shell-Volcanic Ash: Effect of Synthesis Conditions. Journal of the American Ceramic Society, 2016. **99**(9): p. 3159-3166.

Djobo, J.N.Y., et al., Mechanical activation of volcanic ash for geopolymer synthesis: effect on reaction kinetics, gel characteristics, physical and mechanical properties. RSC Advances, 2016. **6**(45): p. 39106-39117.

Djobo, J.N.Y., et al., Mechanical properties and durability of volcanic ash based geopolymer mortars. Construction and Building Materials, 2016. **124**: p. 606-614.

Djobo, J.N.Y., et al., Reactivity of volcanic ash in alkaline medium, microstructural and strength characteristics of resulting geopolymers under different synthesis conditions. Journal of Materials Science, 2016. **51**(22): p. 10301-10317.

Duxson, P., et al., Geopolymer technology: the current state of the art. Journal of Materials Science, 2007. **42**(9): p. 2917-2933.

E.N. Kani, A. Allahverdi, J.L. Provis, Calorimetric study of geopolymer binders based on natural pozzolan, J Therm Anal Calorim 127 (3) (2017) 2181–2190.

Fomina, E.V., V.V. Strokova, and N.I. Kozhukhova, Application of Natural Aluminosilicates in Autoclave Cellular Concrete. World Applied Sciences Journal, 2013. **25**(1): p. 48-54.

Gök, A., F. Göde, and B.E. Türkaslan, Synthesis and characterization of polyaniline/pumice (PAn/Pmc) composite. Materials Science and Engineering: B, 2006. **133**(1): p. 20-25.

Goldsworthy, H. and M. ZHU, Mortar studies towards the replication of Roman concrete. Archaeometry, 2009. **51**(6): p. 932-946.

Hajimohammadi, A., J.L. Provis, and J.S. van Deventer, Effect of alumina release rate on the mechanism of geopolymer gel formation. Chemistry of Materials, 2010. **22**(18): p. 5199-5208.

Hajimohammadi, A., J.L. Provis, and J.S. Van Deventer, One-part geopolymer mixes from geothermal silica and sodium aluminate. Industrial & Engineering Chemistry Research, 2008. **47**(23): p. 9396-9405.

He, J., et al., Synthesis and characterization of red mud and rice husk ash-based geopolymer composites. Cement and Concrete Composites, 2013. **37**: p. 108-118.

He, J., et al., The strength and microstructure of two geopolymers derived from metakaolin and red mud-fly ash admixture: a comparative study. Construction and Building Materials, 2012. **30**: p. 80-91.

Heah, C., et al., Study on solids-to-liquid and alkaline activator ratios on kaolin-based geopolymers. Construction and Building Materials, 2012. **35**: p. 912-922.

Hua, H.W.L.Z.W. and Z. Li, Preparation and Characterization of Cu_2O Crystals Induced by the Magnetic Field. Materials Review, 2007: p. S3.

Jha, B. and D. Singh, A review on synthesis, characterization and industrial applications of flyash zeolites. Journal of Materials Education, 2011. **33**(1): p. 65.

Kalinkina, E.V., et al., Sorption of atmospheric carbon dioxide and structural changes of Ca and Mg silicate minerals during grinding: I. Diopside. International journal of mineral processing, 2001. **61**(4): p. 273-288.

Kani, E.N. and A. Allahverdi, Effect of chemical composition on basic engineering properties of inorganic polymeric binder based on natural pozzolan. Ceramics-Silikaty, 2009. **53**(3): p. 195-204.

Kani, E.N., A. Allahverdi, and J.L. Provis, Calorimetric study of geopolymer binders based on natural pozzolan. Journal of Thermal Analysis and Calorimetry, 2017. **127**(3): p. 2181-2190.

Kong, D.L., J.G. Sanjayan, and K. Sagoe-Crentsil, Comparative performance of geopolymers made with metakaolin and fly ash after exposure to elevated temperatures. Cement and Concrete Research, 2007. **37**(12): p. 1583-1589.

Kumar, S., R. Kumar, and S. Mehrotra, Influence of granulated blast furnace slag on the reaction, structure and properties of fly ash based geopolymer. Journal of Materials Science, 2010. **45**(3): p. 607-615.

Langan, B., K. Weng, and M. Ward, Effect of silica fume and fly ash on heat of hydration of Portland cement. Cement and Concrete research, 2002. **32**(7): p. 1045-1051.

Lecomte, I., et al., Synthesis and characterization of new inorganic polymeric composites based on kaolin or white clay and on ground-granulated blast furnace slag. Journal of materials research, 2003. **18**(11): p. 2571-2579.

Lee, W. and J. Van Deventer, Structural reorganisation of class F fly ash in alkaline silicate solutions. Colloids and Surfaces A: Physicochemical and Engineering Aspects, 2002. **211**(1): p. 49-66.

Leonelli, C., et al., Volcanic ash as alternative raw materials for traditional vitrified ceramic products. Advances in applied ceramics, 2007. **106**(3): p. 135-141.

Li, X., et al., Investigation on microstructure, composition, and cytocompatibility of natural pumice for potential biomedical application. Tissue Engineering Part C: Methods, 2009. **16**(3): p. 427-434.

Li, Z. and S. Liu, Influence of slag as additive on compressive strength of fly ash-based geopolymer. Journal of Materials in civil engineering, 2007. **19**(6): p. 470-474.

Lizcano, M., et al., Effects of Water Content and Chemical Composition on Structural Properties of Alkaline Activated Metakaolin-Based Geopolymers. Journal of the American Ceramic Society, 2012. **95**(7): p. 2169-2177.

Mason, B.J., The Analysis of Taupo Pumice as an Effective Partial Cement Replacement in Concrete. 2012.

Mourhly, A., et al., The synthesis and characterization of low-cost mesoporous silica SiO2 from local pumice rock. Nanomaterials and Nanotechnology, 2015. **5**: p. 35.

Muntingh, Y., Durability and diffusive behaviour evaluation of geopolymeric material. 2006, Stellenbosch: University of Stellenbosch.

Nath, P. and P.K. Sarker, Use of OPC to improve setting and early strength properties of low calcium fly ash geopolymer concrete cured at room temperature. Cement and Concrete Composites, 2015. **55**: p. 205-214.

Nesbitt, H. and G. Young, Prediction of some weathering trends of plutonic and volcanic rocks based on thermodynamic and kinetic considerations. Geochimica et Cosmochimica Acta, 1984. **48**(7): p. 1523-1534.

Provis, J.L. and J.S.J. Van Deventer, Geopolymers: structures, processing, properties and industrial applications. 2009: Elsevier.

S. Kumar, R. Kumar, S. Mehrotra, Influence of granulated blast furnace slag on the reaction, structure and properties of fly ash based geopolymer, J Mater Sci 45 (3) (2010) 607–615.

Senna, M., How can we make solids more reactive? Basics of mechanochemistry and recent new insights. ChemTexts, 2017. **3**(2): p. 4.

Shi, C. and R.L. Day, Chemical activation of blended cements made with lime and natural pozzolans. Cement and Concrete Research, 1993. **23**(6): p. 1389-1396.

Tchakouté, H.K., et al., A comparative study of two methods to produce geopolymer composites from volcanic scoria and the role of structural water contained in the volcanic scoria on its reactivity. Ceramics International, 2015. **41**(10): p. 12568-12577.

Tekin, I., Properties of NaOH activated geopolymer with marble, travertine and volcanic tuff wastes. Construction and Building Materials, 2016. **127**: p. 607-617.

Van Deventer, J.S., J.L. Provis, and P. Duxson, Technical and commercial progress in the adoption of geopolymer cement. Minerals Engineering, 2012. **29**: p. 89-104.

Van Jaarsveld, J., J. Van Deventer, and L. Lorenzen, The potential use of geopolymeric materials to immobilise toxic metals: Part I. Theory and applications. Minerals Engineering, 1997. **10**(7): p. 659-669.

Walkley, B., et al., Effect of MgO incorporation on the structure of synthetic alkali-activated calcium aluminosilicate binders.

Wallah, S.E., Drying shrinkage of heat-cured fly ash-based geopolymer concrete. Modern Applied Science, 2009. **3**(12): p. 14.

Wang, J., et al., Mechanically activating nucleation and growth of complex perovskites. Journal of Solid State Chemistry, 2000. **154**(2): p. 321-328.

Watanabe, H., Critical rotation speed for ball-milling. Powder technology, 1999. **104**(1): p. 95-99.

Wen, B., et al., Formation mechanism of diamond nanocrystal from catalysed carbon black. Journal of Physics: Condensed Matter, 2004. **16**(39): p. 6891.

White, C.E., et al., In situ X-ray pair distribution function analysis of geopolymer gel nanostructure formation kinetics. Physical Chemistry Chemical Physics, 2013. **15**(22): p. 8573-8582.

Yip, C.K., G.C. Lukey, and J.S. Dean, Effect of blast furnace slag addition on microstructure and properties of metakaolinite geopolymeric materials. Advances in Ceramic Matrix Composites IX, Volume 153, 2004: p. 187-209.

Živica, V., S. Balkovic, and M. Drabik, Properties of metakaolin geopolymer hardened paste prepared by high-pressure compaction. Construction and Building Materials, 2011. **25**(5): p. 2206-2213.

CHAPTER 8: POTENTIAL OF USING INDUSTRIAL WASTES FOR PRODUCTION OF GEOPOLYMER BINDER AS GREEN CONSTRUCTION MATERIALS

This chapter was first published as “Almalkawi, Areej T., Anagi Balchandra, and Parviz Soroushian. "Potential of Using Industrial Wastes for Production of Geopolymer Binder as Green Construction Materials." Construction and Building Materials 220 (2019): 516-524.

8.1 Introduction

Large-volume use of industrial wastes for production of construction materials can divert large quantities of industrial byproducts from landfills for value-added use towards improving the sustainability and economics of infrastructure systems [1-3]. This practice can also mitigate the release of toxic leachates to the environment by stabilizing the hazardous constituents of some industrial byproducts.

The slate of fuels burned by power plants to generate electricity has been expanded beyond coal, to include biomass and municipal solid waste (among others). Combustion of these fuels generates solid residues (ash). Examples of these solid residues are coal fly ash, bottom ash resulting from combustion of municipal solid wastes, and biomass (e.g., rice husk) ash [4-6]. These ashes largely comprise the mineral constituents of each fuel. The combustion process also concentrates any heavy metal constituents of the fuel in ash, which should be addressed in development of applications for the ash.

The work reported herein develops an alternative binder chemistry using a blend of coal, biomass and municipal solid waste combustion ashes. The binder chemistry used here yields hydration products with desirable capabilities for stabilization of heavy metals. Brief

introductions to coal fly ash, rice husk ash, and municipal solid waste combustion ash are presented below followed by a concise introduction to the hydraulic binder chemistry considered here. A sustainable mechanochemical approach was adopted for production of hydraulic binder, which is also briefly introduced in the following.

Coal fly ash is the ash separated from the flue gas of power plants burning pulverized coal [7, 8]. It comprises fine spherical particles that precipitate from the stack gases. Coal fly ash is largely amorphous with desired reactivity; its chemical composition comprises largely of silicon, aluminum and calcium.

Rice husks (RHs) is a byproduct of paddy rice processing. It is a renewable fuel for generation of energy and weighs approximately 20% of the harvested paddy. Rice husk ash (RHA) is the solid residue resulting from combustion of rice husk for power generation [9, 10]. Its chemistry is dominated by silica (90-95 wt.%), which is largely amorphous [11] with residual carbon as the main impurity and other traces metal cations such as K and Ca. Rice husk ash assumes a porous microstructure which raises its reactivity by producing large specific surface areas. Silica can be crystalline or amorphous depending on the temperature of calcination and exposure time [12, 13]. Amorphous rice husk ash is a high-performance pozzolan was used as a supplementary binderitious material (SCM) that can partially replace ordinary Portland binder in the concrete mix proportions [9, 14]. Geopolymers have also been prepared with RHA as a source of amorphous silica; investigations in this area have addressed the effects of such factors as alkalinity, curing time and particle size distribution [15-17].

Energy-from-Waste (EFW) facilities recover energy from municipal solid waste in specially designed boilers to ensure complete combustion for efficient recovery of energy [18, 19] . The

EFW process produces an ash byproduct that comprises the bottom ash that remains after the combustion process and the residue that remains from emission control systems. A main aim for using beneficiary of incineration residues is in production of construction materials. Bottom ashes have been investigated as road subbase material, and as an alternative to sand and gravel [20]. Replacing primary resources by secondary raw materials compacts material cycles and lower natural resource depletion, therefore contributing to the recognition of a circular economy. Moreover, the embodied energy relevant to first manufacturing of recycled materials is usually less than that of primary materials. In addition to the consumption of sourced materials, the consequences of resource mining must be taken into consideration [21]. Utilizing of residual ashes and municipal solid waste (MSW) ash in building materials can be viewed as a practicable alternative to landfilling, considering the past success in recycling of different waste sources (e.g. , blast-furnace slag ,coal fly ash, bauxite fines, phospho-gypsum) [22,70-71].

Geopolymerization process is based on the natural stoichiometry reaction that arises between amorphous silica- and alumina-rich solids in high alkaline activator solutions at nearly elevated temperatures. This reaction yields a geopolymer material with high-order in terms of stability , its microstructure consist of an amorphous polymeric network with interconnected Si–O–Al–O– Si bonds [23-28, 68-70] . The advantage of RHA as a source of reactive silica for geopolymerizaiton relate to its highly amorphous nature and also its high specific surface area. Adequate sources of alumina should be used together with RHA in order to achieve viable Si/Al ratios [30-32].

Mechanochemistry concerns chemical and physio-chemical changes of materials at all states of aggregation via input of mechanical energy. The intensity of mechanical energy required

to render Mechanochemical effects can be realized in various mills, including the ball mills that are currently used in binder production facilities [44]. Mechanochemistry is often viewed as a "green" approach to chemical processing because it avoids the use of solvents and elevated temperatures, and attempts to induce favorable physio-chemical phenomena using non-hydrostatic mechanical stresses that are generally applied at high rates [33-37]. At the atomic scale, the mechanical deformation of crystalline structural arrangements under stress can be considered as a distortion or modification of the coordination shells of individual atoms. In turn, atomistic processes can be generically described as local structural excitations [33-37]. These excitations pull the system away from thermodynamic equilibrium, which usually promotes a significant enhanbinder of chemical reactivity [38, 39].

A technical feasibility of incorporation industrial waste materials employed in the current work as a supplementary binderitious material in concrete mix design has been reported in [61-63]. A ternary blend of Portland binder, industrial residual ashes and limestone powder were formulated to improve the properties of self-compacted concrete [64], and the use of a mixture of these ashes in addition to limestone and wood fibers led to improve the properties of lightweight concrete blocks [64-67]

The main sight of this investigation was on development of a new sustainable class of hydraulic binder that relies upon the robust nature of alkali aluminosilicate binder chemistry to make value-added and large-volume use of rice husk ash, MSW ash and coal fly ash as primary raw materials. In an effort to produce a hydraulic binder that requires only the addition of water (in lieu of alkaline solutions in traditional geopolymerization), the blend of raw materials was forced to undergo Mechanochemical processing.

8.2 Material and Methods

8.2.1 Materials

Class C coal fly ash was supplied as dry powder by the Lansing Board of Water & Light (LBWL) in Lansing, Michigan. RHA with more than 90% amorphous SiO_2 content was obtained by controlled calcination of rice husk at 600°C for two hours, followed by ball milling for 30 minutes, resulting in an average particle size of 22.84 µm. Commercially available potassium hydroxide flakes (caustic potash), sodium carbonate were used as alkaline materials. (ASTM C778) graded standard silica sand was selected as fine aggregate to prepare mortar mixes.

8.2.2 Particle Size Distribution

The particle-size distribution (PSD) (generated through laser granulometry) of the milled municipal solid water (MSW) incineration ash used in this work is presented in **Figure 93**.

. The median particle size was 5.4 µm, and its specific surface area was 60942 (cm^2/cm^3)

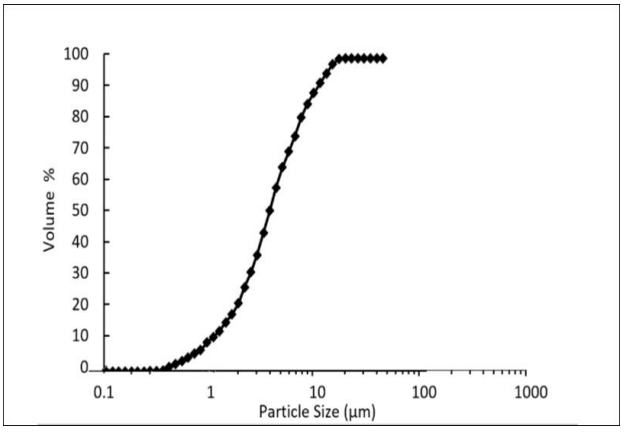

Figure 93. Particle size distribution of the milled municipal solid waste (MSW) incineration ash.

8.2.3 Chemical Composition

Table 18. introduced the chemical compositions of the ashes considered in this investigation, that were obtained via XRF spectroscopy. The MSW ash is observed to be rich in calcium and incorporate chloride and sulfur. Its loss-on-ignition is also relatively high. The mere presence of chloride and sulfur in MSW ash does not means that they would be necessarily available for deleterious reactions. They will not adversely influence the qualities offered by the resultant hydraulic binder if they get chemically bound in insoluble compounds. One should also evaluate the reason for the high LOI of MSW ash, considering that carbonates with no deleterious effects could also raise the LOI value. The high LOI values of MSW fly ash [41] and MSWI bottom ash [42] have been reported in the literature. The alkali content of MSW ash was more than those of other ashes considered in this investigation. The coal fly ash had relatively high silicon and aluminum oxide constitute that mainly comprised about 65% of the total mass, and the weight ratio of silicon to aluminum oxide was about 2. The relatively high (14.5%) CaO content of this coal fly ash qualifies it as Class C (high calcium) per ASTM C618. Rice husk ash comprises largely of silica; its LOI value was moderate at 5.1%. The amorphous nature of rice husk ash makes it a valuable source of silica for synthesis of alkali aluminosilicate hydraulic binders.

Table 18. Chemical composition of coal fly ash, wt.%.

Material	SiO_2	CaO	Al_2O_3	K_2O	Na_2O	TiO_2	Cl	SO_3	LOI
Rice husk	90.0	0.60	0.01	2.30	--	---	--	--	5.10
Coal fly ash	43.05	14.30	23.33	1.72	0.90	0.03	--	--	1.82
MSW Ash	3.48	48.16	1.00	4.8	0.90	0.72	21.81	8.44	16.1%

8.3 Methods

8.3.1 Processing of Raw Materials

The blend of coal ash, MSW ash and RHA was proportioned to produce a viable SiO_2/Al_2O_3 molar ratio of 2 to 4 which yields desired engineering properties. These formulations as well as those of alkaline materials considered in this investigation are summarized in **Table 19**. The blend of raw materials was undergoing mechanochemical processing to produce hydraulic binder as explained in previous investigations [40].

Table 19. The formulations (by weight) of raw materials considered for synthesis of hydraulic binders with different sources of alkalis.

Mix	RHA	Coal Fly Ash	MSW Ash	Alkaline Material	Water/Binder Ratio
1	0.3	0.2	0.1	Potassium hydroxide (0.4)	0.5
2	0.3	0.2	0.1	Sodium carbonate (0.4)	0.5

The effects of the relative proportions of rice husk ash and the municipal solid waste ash on the compressive strength development attributes of the resulting hydraulic binder were also investigated. The raw materials formulations considered in this series of tests are introduced in **Table 20**.

Table 20. The formulations of hydraulic binders considered for evaluation of the effects of the relative proportions of rice husk ash and the municipal solid waste ash on the compressive.

Mix	RHA	Coal Fly Ash	MSW Ash	Alkaline Material	Water/Binder Ratio	Sand
1	0	0.2	0.4	Potassium hydroxide (0.4)	0.5	2.75
2	0.1	0.2	0.3	Potassium hydroxide (0.4)	0.5	2.75
3	0.2	0.2	0.2	Potassium hydroxide (0.4)	0.5	2.75
4	0.3	0.2	0.1	Potassium hydroxide (0.4)	0.5	2.75
5	0.4	0.2	0	Potassium hydroxide (0.4)	0.5	2.75

8.3.2 Characterization Methods

The mortar mixtures had a silica sand-to-binder ratio of 2.5, and water-to-binder ratio of 0.5 to reach a desired fresh mix workability. They were prepared in a planetary mixer, cast into 50 cube molds, and consolidated under external vibration. The samples were kept in sealed condition at 90-97% relative humidity and at room temperature. They were demolded after 24 hours and continued sealing at 90-97% relative humidity and room temperature (23 C°) for compression testing at 7 days age. Compression tests were performed in universal test machine with speed of 0.1 mm/min. Ten reproduced samples were casted and tested for each mix design, and the average values of compressive strength were determined.

The chemical and elemental analysis of raw materials was inspected using X-ray fluorescence (XRF) spectroscopy. Their phase identifications were examined using X-ray diffraction (XRD) spectroscopy. FTIR spectroscopy was also performed on the raw materials and the hydraulic binder in the 4000–400 cm^{-1} range to observe their chemical properties (bond nature). The raw materials and the ruptured surfaces of hydrated binder pastes (at 28 days of age) were also evaluated via scanning electron microscopy to gain better understanding into their microstructural traits. SEM observations were made on a JCM-5000 NeoScope™ at an accelerating voltage of 10-15 kV using a secondary electron (SE) detector. Samples were sputtered with gold prior to SEM observations.

The Toxicity Characteristic Leaching Procedure (TCLP) is a test method used to determine whether a waste is hazardous due to its characteristics. TCLP tests were carried out to determine the potential for geopolymerization to reduce the leachability of specific elements in the IFA. The

20 heavy metals (Be, Al, V, Cr, Mn, Co, Ni, Cu, Zn, As, Se, Mo, Ag, Cd, Sb, Ba, Hg, Tl, Pb, and Th) were tested before and after mechanochemical processing.

8.4 Test Results and Discussion

8.4.1 Chemical Bond Environment

Figure 93a. presents the FTIR spectra of the raw materials for the coal fly ash, rice husk ash and MSW incineration ash. The FTIR data for the hydrated mechanochemically processed binder is presented in **Figure 93b.** The distinct peak centered around 500-560 cm^{-1} (band A) can be assigned to the O–Si–O vibrational bending mode of the SiO_4 tetrahedra. This band provides an indication of the degree of "amorphization", as the intensity is not associated with the degree of crystallization [43]. Peaks at infrared spectrum ranges of 1200–900 cm^{-1} (bands c, d) can be ascribed to the asymmetric stretching vibration mode of Si–O/Al–O peak at of 850–777 cm^{-1} (band f), that may be associated with asymmetric stretching vibration of Si–O–Si. The Si–O–Si stretching vibration mode is more influential than the O–Si–O bending mode. Therefore, one may use the Si–O–Si stretching vibration as an indication of the degree of geopolymerization [44-47] . The major differences between the as-received materials and the mechanochemically processed hydraulic binder relate to the shifts in the band around 1100- 1200 cm^{-1} to around 1050 cm^{-1} (band g), and around 900 cm^{-1} (band c) to 870cm^{-1} (band f), both of which decreased slightly in intensity.

Moreover, the Si–O–Si peak shifted to a frequency that is lower than that in original residual ashes, indicating that a chemical change has been created in the binder phase. These shifts suggest that new binder/phases were created as a result of the mechanochemically induced reactions between ashes and alkaline materials (band c) [48]. This drop in intensity denoted that the amorphous phase in the residual ashes already have depolymerized to Si–O and Al–O bonds, and the shifts point at the polycondensation of these chemical bonds in the presence of alkaline medium [49].

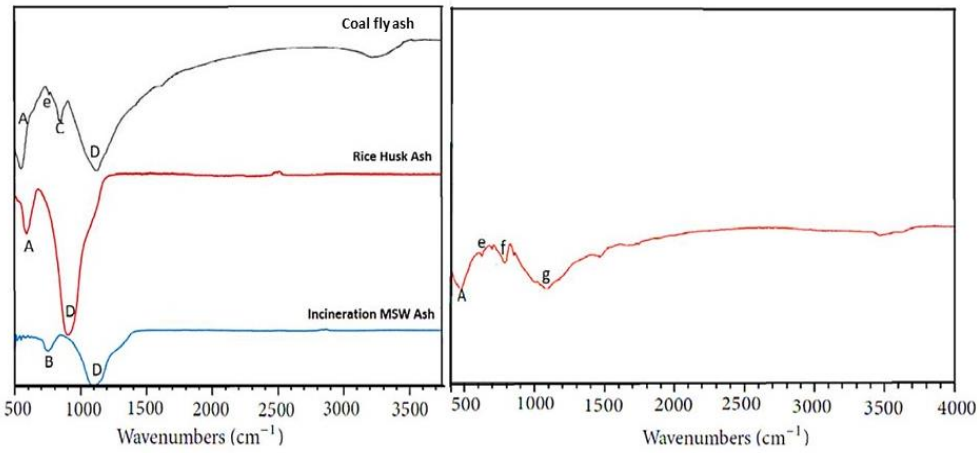

Figure 94. FTIR spectra of: (a) raw ash materials; and (b) the mechanochemically processed hydrated binder.

8.4.2 SEM Observations

The scanning electron microscope images of different ashes presented in **Figure 95**. indicate that: (i) the ground municipal solid waste incineration ash particles assume a random geometry with micrometer-scale dimensions, and appear to be dense; (ii) the coal fly ash particles exhibit characteristic spherical morphologies with micrometer-scale dimensions, and larger spherical particles seem to be coated with smaller particles; and (iii) ground rice husk ash exhibits a porous structure that increases its directly accessible surface area, and benefits its reactivity.

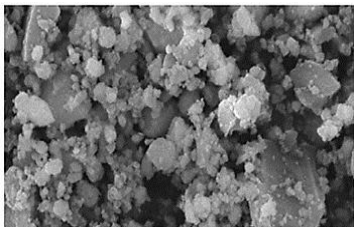

Coal fly ash

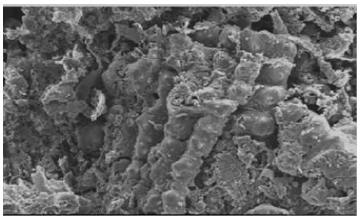

Rice husk

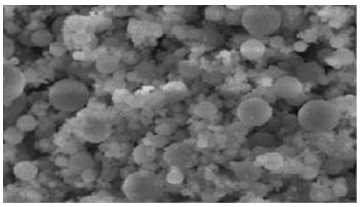

Municipal solid waste

Figure 95. SEM micrographs of the ground municipal solid waste (MSW) ash, coal fly ash, and ground rice husk used in this investigation.

8.4.3 Mineralogy

The XRD patterns of these ashes shown in **Figure 95.** suggest that: (i) the municipal solid waste incineration ash is semi-crystalline, exhibiting XRD peaks corresponding to quartz and calcite, and it has a relatively low content of glassy phase when compared with other ashes; (ii) coal fly ash is also semi-crystalline with XRD peaks corresponding to mullite and quartz; and (iii) rice husk ash appears to be largely amorphous with a broad hump within around the region of 20-30° 2Theta that could point at the presence of an amorphized cristobalite [50]. The shift of FTIR spectra was observed in mechanochemically hydrated binder and it refereed to the formation of the new phases of binder (both Muscovite and Calcite , main elemental composition Ca and . This confirmed by X-ray powder diffraction analysis of the hydrated.

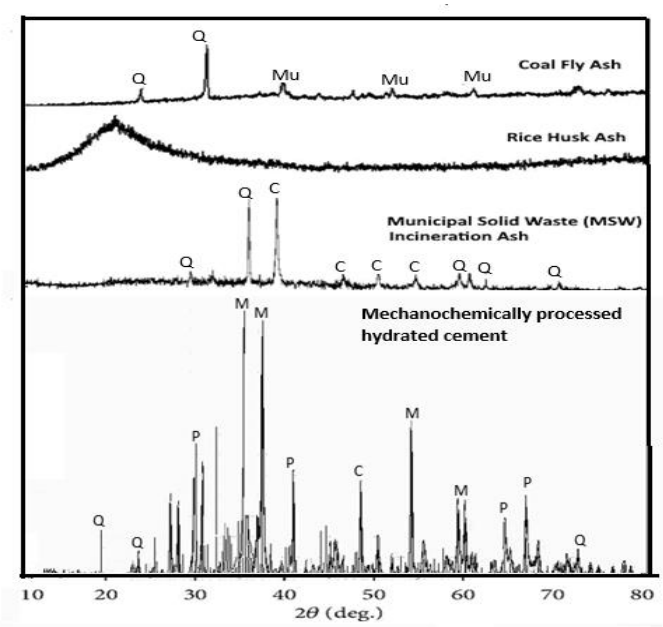

Figure 96. XRD patterns of the three ashes used in this investigation (C=calcite, Q=quartz, Mu=mullite, and patterns of the mechanochemically processed hydrated binder ; (Q: Quartz, M:Muscovite , P : Portlandite, C : Calcite.

8.4.4 Compressive Strength

8.4.4.1 Effect of Alkali Source

The compressive strength test results obtained after 7 days of curing at room temperature in sealed condition are presented in **Figure 97**. for geopolymer binders pre pared with two different alkali sources (potassium hydroxide and sodium carbonate). Potassium hydroxide is observed to produce to produce a significantly higher 7-day compressive strength when compared with sodium carbonate. It should be noted that ASTM C1157 requires a 7-day compressive strength of 18.5 MPa for the 'General Use' class of hydraulic binder. The formulation and processing conditions considered in this experimental program yields a 7-day compressive strength exceeding 50 MPa, that is more than twice the standard requirement, when potassium hydroxide is used as the source of alkali. Sodium carbonate would be a successful activator as far as the

formulation can readily release calcium cations to the solution in order to produce sodium hydroxide through reactions with sodium carbonate. In spite of the relatively high calcium content of the binder formulation considered here, its availability in solution could be why sodium carbonate could not act as a viable source of alkalis. The compressive strength obtained via geopolymerization reactions is influenced strongly by both the alumina-silicate precursors and the alkaline compound used in the formulation. The molecular structure and the concentration of alkalis are key factors influencing the geopolymerization process [51, 52] . The OH ions supplied by alkalis (e.g., potassium hydroxide) attack the sialate-siloxo bonds to liberate aluminate and silicate to the solution that react to form rearranged gels, which finally condensate by releasing water to produce a hardened solid [53, 54]. Strong alkalis tend to act more swiftly when the soluble silica is available, and play a crucial role in dissolving the silica and alumina constituents of the aluminosilicate precursors that enables their participation in the polycondensation stage of the geopolymerization process [53] .

Scanning electron microscope images of the hydration products (**Figure 98**.) indicated that the non-reacted raw materials (e.g., spherical fly ash particles) are more notable in the case of binder prepared with sodium carbonate than that formulated with potassium hydroxide. This observation suggests that sodium carbonate could not, in the formulation considered here, could not produce the level of alkalinity required for effective dissolution of the aluminosilicate precursors.

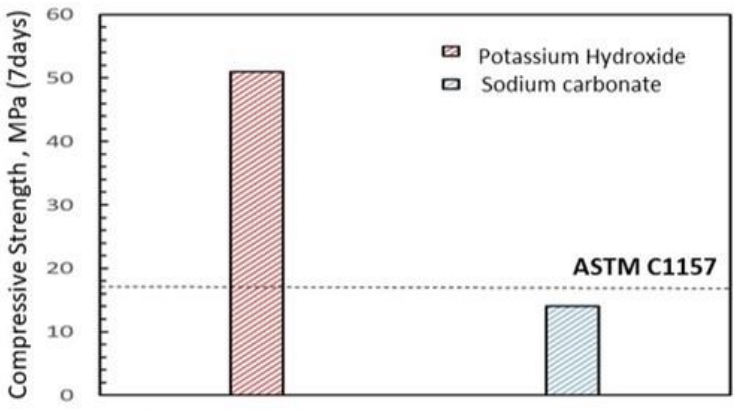

Figure 97. Seven-day compressive strengths obtained with different sources of alkalis.

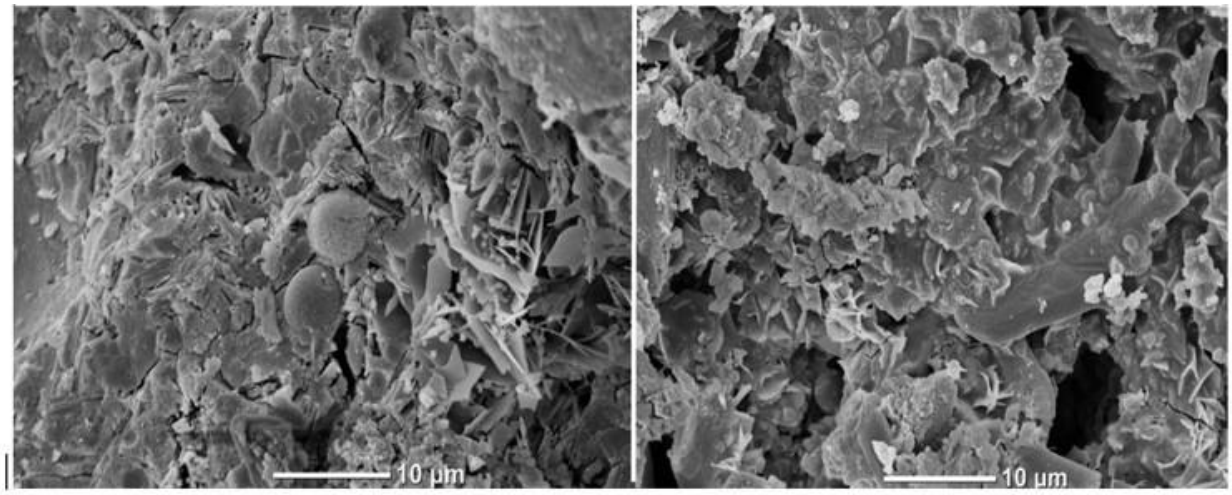

(a) Sodium carbonate (b) Potassium hydroxide

Figure 98. Microstructures of hardened geopolymer binder pastes with either sodium carbonate or potassium hydroxide used as the sources of alkalis.

8.4.5 Effects of the Relative Quantities of Rice Husk Ash and Municipal Solid Waste Ash on the Resulting Hydraulic Geopolymer Binder Performance

Rice husk ash is a source of reactive silica; the municipal solid waste ash, on the other hand, is rich in calcium oxide and incorporates some potassium oxide. They can feasibly make synergistic contributions to the chemistry of the hydraulic binder. An experimental investigation was undertaken in order to evaluate the effects of their proportions in the hydraulic binder formulation on the end product performance.

Figure 99. shows the compressive strength test data generated for the hydraulic binder prepared with different RHA and MSW ash contents. The compressive strength of all binder formulations is observed to increase with increasing RHA content (that is accompanied with decreasing MSW ash content). Rice husk ash (RHA) is a source of active silica; a rise in RHA content would thus raise the prevalence of Si-O-Si bonds which are stronger than either Si-O-Al and Al-O-Al bonds [23, 28]. The reactivity of silica in RHA could also benefit the extent of reactions after similar curing conditions. A rise in RHA content is thus expected to raise the degree of condensation and the prevalence of relatively strong Si-O-Si bonds in the condensed tetrahedral aluminosilicate network, thus increasing the compressive strengths obtained with the hydraulic binder. Compressive strength, however, decreased when the rice husk ash content was raised beyond 30% (with 10% MSW content). This reversion of the trend in compressive strength with increasing RHA content could be attributed to: (i) hindrance of the reorganization of dissolved silica and alumina due to the excess concentration of soluble silica, which reduces the skeletal density of the geopolymer binder (reportedly occurs at Si/Al molar ratios exceeding 2) [55], which weakens the resulting gel; and (ii) reduced dissolution of rice husk ash particles, with the remaining unreacted or partially reacted rice husk ash particles (detected in the SEM images reviewed in the following) acting as porous fillers with adverse effects on strength [17]. For the raw materials types and formulations considered in this investigation, an RHA content of 30% (with an MSW ash content of 10%) seems to yield a satisfactory chemical stability in solution, inducing polycondensation effects with favorable strength development characteristics.

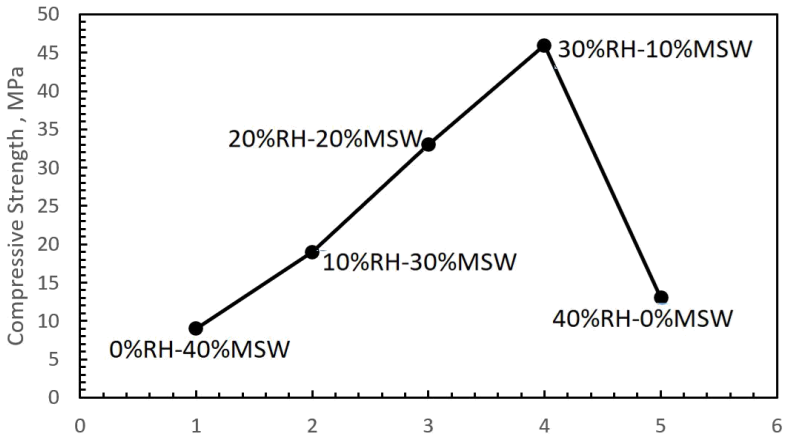

Figure 99. Compressive strength development attributes of hydraulic binders formulated with different RHA and MSW ash contents.

hydration products of binder's formulations with different RHA and MSW ash contents only – No coal fly ash content in this test-. Unreacted or partially reacted binder particles can be detected in all these images, which is a characteristic feature of some geopolymers [19]. A relatively dense structure with low amount of unreacted or partially reacted binder particles is noted for the binder formulation with 30% RHA and 10% MSW ash (**Figure 100**.)

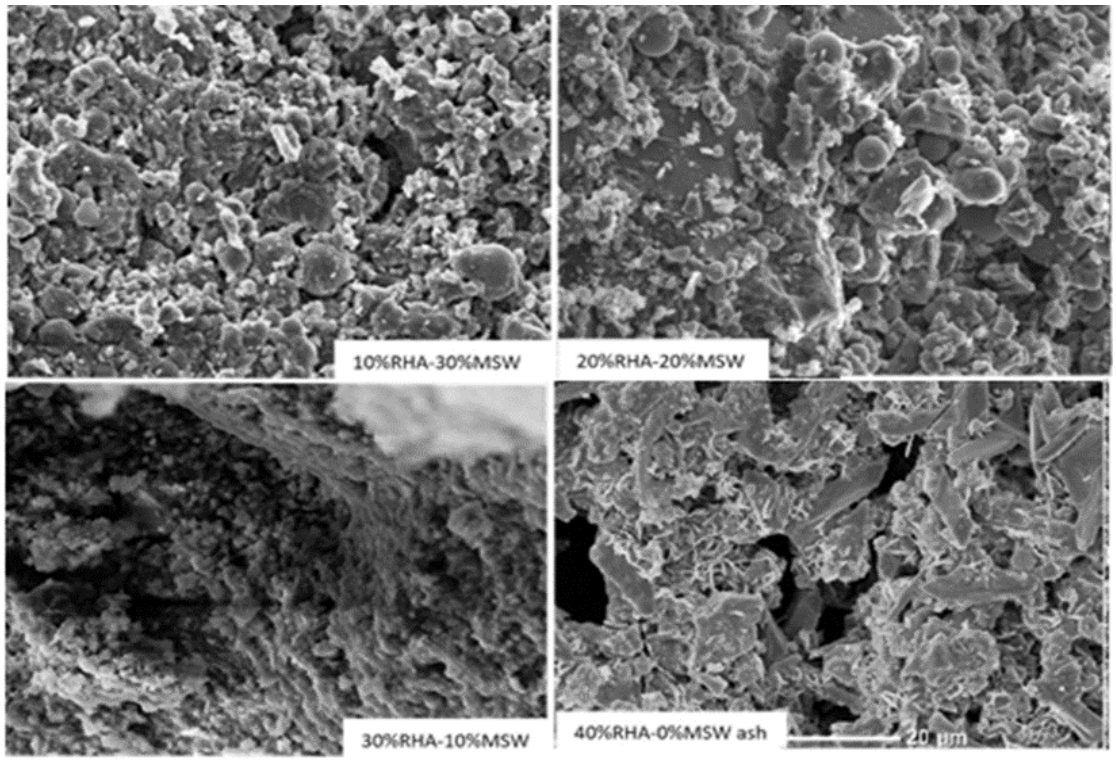

Figure 100. Representative SEM micrographs of the hydration products of hydraulic binders formulated with different rice husk ash (RHA) and municipal solid waste (MSW) ash contents.

8.4.6 Toxicity tests

TCLP tests were carried out to determine the potential of the mechanochemical processing and the subsequent hydration reactions to reduce leaching of heavy metals to the environment. Release of the RCRA heavy metals (Pb, Cd, Sr, Ba, Mo, Zn, Co) was evaluated for the blend of raw materials, the mechanochemically processed hydraulic binder, and the hydrated binder paste. The results for Formulation 4 (comprising 30% rice husk ash, 10% MSW ash, 20% coal fly ash and 40% KOH) are presented in **Figure 101**. Mechanochemical processing produced significant reduction in the concentration of hazardous metal cations in leachates. This finding points at the immobilization capabilities of the physico-chemical phenomena that occur during

mechanochemical processing of raw materials. Further drops in release of heavy metals are noted after hydration of the binder. This can be attributed to the release of Al and Si species in the alkaline solution, followed by geopolymerization reactions that yield structures with high heavy metals immobilization qualities [56, 57]. The notable immobilization of Pb observed in **Figure 101**. can be attributed to the formation of monomeric and/or oligomeric aluminate and silicate species, which then polycondense to form insoluble products that effectively encapsulate Pb. The immobilization of Pb within alkali activated matrices may be viewed as an encapsulation effect of the precipitates and gels, with limited contribution of the adsorption effects [58-60].

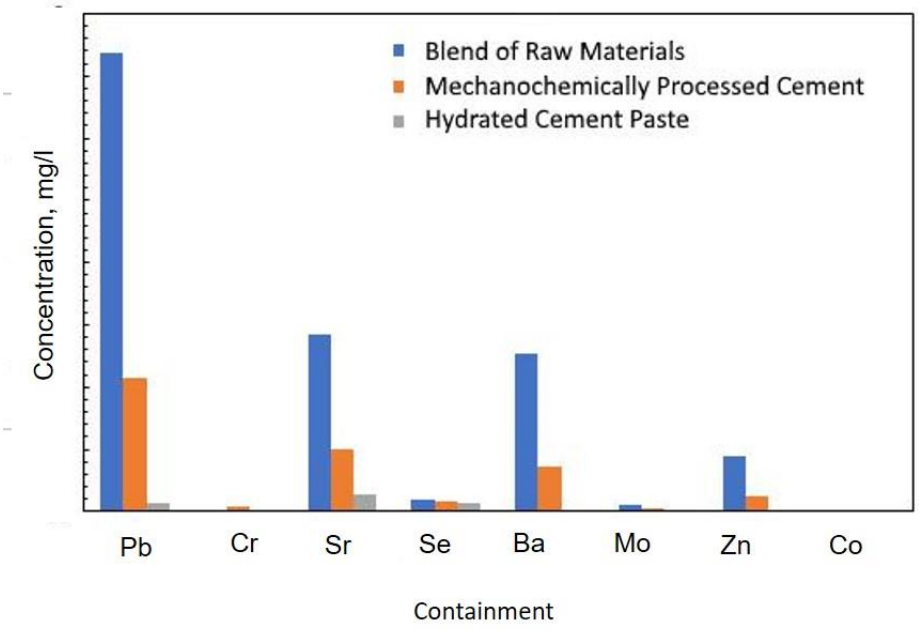

Figure 101. Toxicity characteristic leaching procedure (TCLP) analysis of hydraulic binder prior to and after mechanochemical processing and subsequent hydration of binder.

.

8.5 Conclusions

1. Combustion ashes of rice husk, municipal solid waste and coal can be formulated to yield desired SiO_2/Al_2O_3 ratios and calcium contents for production of hydraulic binders with alkali aluminosilicate (geopolymer) chemistries. When blended with either potassium hydroxide or a blend of sodium carbonate and potassium hydroxide flakes, and subjected to mechanochemical synthesis, hydraulic binders with desired strength development characteristics can be obtained with this ternary blend of combustion ashes.

2. There is an optimum silica content which maximizes the strength development attribute of the hydraulic binder. This silica content can be achieved by adjusting the rice husk ash content in the raw materials formulation. While higher contents of reactive silica (from rice husk ash) benefit the skeletal structure of alkali aluminosilicate hydrates, excess silica contents can disturb the polycondensation process and the resultant hydrates.

3. The composition of alkali activator influenced the strength development characteristics of the mechanochemically processed hydraulic binder. The highest compressive strength was achieved when potassium hydroxide (in lieu of a blend of potassium hydroxide and sodium carbonate) was used as alkaline medium.

4. Microstructural investigations of hydrated binder pastes confirmed that the density of hydrates and the extent of reactions of binder particles correlated with the compressive strength development characteristics of the hydraulic binders considered in this investigation.

5. Mechanochemical processing of the blend of raw materials into a hydraulic binder reduces the presence of heavy metals among the leachates. Hydration of the resultant binder further reduces the leaching of heavy metals.

8.6 Acknowledgements

The authors would like to acknowledge the financial support of the U.S. Environmental Protection Agency (EPA) Contract No. EPD-D-15-036 – United States.

REFERENCES

REFERENCES

Ahmari, S. and L. Zhang, Utilization of binder kiln dust (CKD) to enhance mine tailings-based geopolymer bricks. Construction and Building Materials, 2013. **40**: p. 1002-1011.

Al-Kutti, W., et al., An overview and experimental study on hybrid binders containing date palm ash, fly ash, OPC and activator composites. Construction and Building Materials, 2018. **159**: p. 567-577.

Almalkawi, A.T., S. Hamadna, and P. Soroushian, One-part alkali activated binder based volcanic pumice. Construction and Building Materials, 2017. 152: p. 367-374.

Aprianti, E., A huge number of artificial waste material can be supplementary binderitious material (SCM) for concrete production–a review part II. Journal of Cleaner Production, 2017. 142: p. 4178-4194.

Aprianti, E., et al., Supplementary binderitious materials origin from agricultural wastes–A review. Construction and Building Materials, 2015. 74: p. 176-187.

Arulrajah, A., Kua, T.A., Horpibulsuk, S., Phetchuay, C., Suksiripattanapong, C. and Du, Y.J. (2016), "Strength and microstructure evaluation of recycled glass-fly ash geopolymer as low-carbon masonry units", Construction and Building Materials, Vol.114, pp.400-406.

Arulrajahet al. (2017). "Recycled glass as a supplementary filler material in spent coffee grounds geopolymers", Construction & Building Materials, Vol. 151, pp. 18-27

Asavapisit, S. and N. Ruengrit, The role of RHA-blended binder in stabilizing metal-containing wastes. Binder and Concrete Composites, 2005. 27(7-8): p. 782-787.

Bogush, A.A., et al., Element speciation in UK biomass power plant residues based on composition, mineralogy, microstructure and leaching. Fuel, 2018. 211: p. 712-725.

Butyagin, P.Y., Active states in mechanochemical reactions. Vol. 14. 1989: CRC Press.

Chang, J.I. and Y. Chen, Effects of bulking agents on food waste composting. Bioresource technology, 2010. 101(15): p. 5917-5924.

Chindaprasirt, P., et al., Comparative study on the characteristics of fly ash and bottom ash geopolymers. Waste Management, 2009. 29(2): p. 539-543.

Chindaprasirt, P., S. Jenjirapanya, and U. Rattanasak, Characterizations of FBC/PCC fly ash geopolymeric composites. Construction and Building Materials, 2014. 66: p. 72-78.

Chindaprasirt, P., U. Rattanasak, and C. Jaturapitakkul, Utilization of fly ash blends from pulverized coal and fluidized bed combustions in geopolymeric materials. Binder and Concrete Composites, 2011. 33(1): p. 55-60.

Davidovits, J., Geopolymers: inorganic polymeric new materials. Journal of Thermal Analysis and calorimetry, 1991. 37(8): p. 1633-1656.

Delogu, F. and G. Cocco, Crystallite size refinement in elemental species under mechanical processing conditions. Materials Science and Engineering: A, 2006. 422(1): p. 198-204.

Dimas, D., I. Giannopoulou, and D. Panias, Polymerization in sodium silicate solutions: a fundamental process in geopolymerization technology. Journal of materials science, 2009. 44(14): p. 3719-3730.

Duxson, P., et al., The effect of alkali and Si/Al ratio on the development of mechanical properties of metakaolin-based geopolymers. Colloids and Surfaces A: Physicochemical and Engineering Aspects, 2007. 292(1): p. 8-20.

Duxson, P., et al., Understanding the relationship between geopolymer composition, microstructure and mechanical properties. Colloids and Surfaces A: Physicochemical and Engineering Aspects, 2005. 269(1-3): p. 47-58.

Fernandes, I.J., et al., Physical, chemical and electric characterization of thermally treated rice husk ash and its potential application as ceramic raw material. Advanced Powder Technology, 2017. 28(4): p. 1228-1236.

Fernández-Jiménez, A. and A. Palomo, Characterisation of fly ashes. Potential reactivity as alkaline binders☆. Fuel, 2003. 82(18): p. 2259-2265.

Fernández-Jiménez, A. and A. Palomo, Composition and microstructure of alkali activated fly ash binder: Effect of the activator. Binder and concrete research, 2005. 35(10): p. 1984-1992.

Fernández-Jiménez, A. and A. Palomo, Mid-infrared spectroscopic studies of alkali-activated fly ash structure. Microporous and Mesoporous Materials, 2005. 86(1-3): p. 207-214.

Freidin, C., Binderless pressed blocks from waste products of coal-firing power station. Construction and Building Materials, 2007. 21(1): p. 12-18.

G. Giaccio, G. Rodríguez de Sensale, R. Zerbino, Failure mechanism of normal and high strength concrete with rice-husk ash, Cem. Concr. Compos. 29 (2007) 566–574.

G. Rodríguez de Sensale, Effect of rice-husk ash on durability of binderitious materials, Cem. Concr. Compos. 32 (2010) 718–725

G. Rodríguez de Sensale, Strength development of concrete with rice-husk ash, Cem. Concr. Compos. 28 (2006) 158–216.

Garg, A., et al., An integrated appraisal of energy recovery options in the United Kingdom using solid recovered fuel derived from municipal solid waste. Waste Management, 2009. 29(8): p. 2289-2297.

Geraldo, R.H., L.F. Fernandes, and G. Camarini, Water treatment sludge and rice husk ash to sustainable geopolymer production. Journal of cleaner production, 2017. 149: p. 146-155.

Gutman, E.M., Mechanochemistry of materials. 1998: Cambridge Int Science Publishing.

He, J., et al., Synthesis and characterization of red mud and rice husk ash-based geopolymer composites. Binder and Concrete Composites, 2013. 37: p. 108-118.

Heinicke, C.M., Impact of prebirth parent personality and marital functioning on family development: A framework and suggestions for further study. Developmental Psychology, 1984. 20(6): p. 1044.

Huynh, T.P., C.L. Hwang, and K.L. Lin, Performance and microstructure characteristics of the fly ash and residual rice husk ash-based geopolymers prepared at various solid-to-liquid ratios and curing temperatures. Environmental Progress & Sustainable Energy, 2017. 36(1): p. 83-92.industry. Minerals engineering, 2007. 20(14): p. 1261-1277.

J. Torkaman, A. Ashori, A. Sadr Momtazi, Using wood fiber waste, rice husk ash, and limestone powder waste as binder replabinder materials for lightweight concrete blocks, Constr. Build. Mater. 50 (2014) 432–436.

Jang, J. and H. Lee, Effect of fly ash characteristics on delayed high-strength development of geopolymers. Construction and Building Materials, 2016. 102: p. 260-269.

Joseph, A.M., et al., The Use of Municipal Solid Waste Incineration Ash in Various Building Materials: A Belgian Point of View. Materials, 2018. 11(1): p. 141.

Kamseu, E., et al., Substitution of sodium silicate with rice husk ash-NaOH solution in metakaolin based geopolymer binder concerning reduction in global warming. Journal of cleaner production, 2017. 142: p. 3050-3060.

Kang, S., et al., Estimation of optimal biomass fraction measuring cycle for municipal solid waste incineration facilities in Korea. Waste Management, 2018. 71: p. 176-180.

Khale, D. and R. Chaudhary, Mechanism of geopolymerization and factors influencing its development: a review. Journal of materials science, 2007. 42(3): p. 729-746.

Komnitsas, K. and D. Zaharaki, Geopolymerisation: A review and prospects for the minerals

Koplík, J., M. Smolková, and J. Tkacz. The Leachability of Heavy Metals from Alkali-Activated Fly Ash and Blast Furnace Slag Matrices. in Materials Science Forum. 2016. Trans Tech Publications Ltd.

Kua et al (2017). "Stiffness and deformation properties of spent coffee grounds based geopolymers", Construction & Building Materials, Vol. 138, pp. 79-87.

Kumar, A. and S. Kumar, Development of paving blocks from synergistic use of red mud and fly ash using geopolymerization. Construction and building Materials, 2013. 38: p. 865-871.

Lee, S., et al., Impact of activator type on the immobilisation of lead in fly ash-based geopolymer. Journal of hazardous materials, 2016. 305: p. 59-66.

Levitas, V.I. and O.M. Zarechnyy, Kinetics of strain-induced structural changes under high pressure. The Journal of Physical Chemistry B, 2006. 110(32): p. 16035-16046.

Levitas, V.I., High-pressure mechanochemistry: conceptual multiscale theory and interpretation of experiments. Physical Review B, 2004. 70(18): p. 184118.

Lo, K.-W., et al., Effect of alkali activation thin film transistor-liquid crystal display waste glass on the mechanical behavior of geopolymers. Construction and Building Materials, 2018. 162: p. 724-731.

Part, W.K., M. Ramli, and C.B. Cheah, An overview on the influence of various factors on the properties of geopolymer concrete derived from industrial by-products. Construction and Building Materials, 2015. 77: p. 370-395.

Phetchuay, C., Horpibulsuk. S., Arulrajah, A., Suksiripattanapong, C., and Udomchai, A. (2016), "Strength development in soft marine clay stabilized by fly ash and calcium carbide residue based geopolymer", Applied Clay Science, Vol.127-128, pp.134-142.

Phummiphan, I., Horpibulsuk, S., Sukmak, P., Chinkulkijniwat, A., Arulrajah, A., and Shen S.L. (2015), "Stabilisation of marginal lateritic soil using high calcium fly ash based geopolymer", Road Materials and Pavement Design, doi: 10.1080/14680629.2015.1132632

Pode, R., Potential applications of rice husk ash waste from rice husk biomass power plant. Renewable and Sustainable Energy Reviews, 2016. 53: p. 1468-1485.

Pour, N., P.A. Webley, and P.J. Cook, Potential for using municipal solid waste as a resource for bioenergy with carbon capture and storage (BECCS). International Journal of Greenhouse Gas Control, 2018. 68: p. 1-15.

Rattanasak, U. and P. Chindaprasirt, Influence of NaOH solution on the synthesis of fly ash geopolymer. Minerals Engineering, 2009. 22(12): p. 1073-1078.

Speight, J.G., Asphalt Materials Science and Technology. 2015: Butterworth-Heinemann.

Sukmak, P., Silva, P.D., Horpibulsuk, S. and Chindaprasirt, P. (2015), "Sulfate resistance of clay-Portland cement and clay-high calcium fly ash geopolymer", Journal of Materials in Civil Engineering, ASCE, Vol.27, No.5, pp.04014158(1-11).

Suksiripattanapong et al (2017). "Strength and microstructure properties of spent coffee grounds stabilized with rice husk ash and slag geopolymers", Construction & Building Materials, Vol. 146, pp. 312-320.

Suryanarayana, C., Mechanical alloying and milling. 2004: CRC Press.

Thuadaij, N. and A. Nuntiya, Synthesis and characterization of nanosilica from rice husk ash prepared by precipitation method. J. Nat. Sci. Special Issue on Nanotechnology, 2008. 7(1): p. 59-65.

Tiwari, H., A. Das, and U. Singh, Novel technique for assessing the burnout potential of pulverized coals/coal blends for blast furnace injection. Applied Thermal Engineering, 2018. 130: p. 1279-1289.

Van Beers, D., A. Bossilkov, and C. Lund, Development of large scale reuses of inorganic by-products in Australia: The case study of Kwinana, Western Australia. Resources, Conservation and Recycling, 2009. 53(7): p. 365-378.

Van Jaarsveld, J., J. Van Deventer, and L. Lorenzen, Factors affecting the immobilization of metals in geopolymerized flyash. Metallurgical and materials transactions B, 1998. 29(1): p. 283-291.

Venkatanarayanan, H.K. and P.R. Rangaraju, Effect of grinding of low-carbon rice husk ash on the microstructure and performance properties of blended binder concrete. Binder and Concrete Composites, 2015. 55: p. 348-363.

Wardhono, A., et al., Comparison of long term performance between alkali activated slag and fly ash geopolymer concretes. Construction and Building materials, 2017. 143: p. 272-279.

Weng, L. and K. Sagoe-Crentsil, Dissolution processes, hydrolysis and condensation reactions during geopolymer synthesis: Part I—Low Si/Al ratio systems. Journal of Materials Science, 2007. 42(9): p. 2997-3006.

Wongsa, A., et al., Use of municipal solid waste incinerator (MSWI) bottom ash in high calcium fly ash geopolymer matrix. Journal of cleaner production, 2017. 148: p. 49-59.

Xie, R., et al., Assessment of municipal solid waste incineration bottom ash as a potential road material. Road Materials and Pavement Design, 2017. 18(4): p. 992-998.

Yao, Z., et al., A comprehensive review on the applications of coal fly ash. Earth-Science Reviews, 2015. 141: p. 105-121.

Yap, H. and J. Nixon, A multi-criteria analysis of options for energy recovery from municipal solid waste in India and the UK. Waste management, 2015. 46: p. 265-277.

Zhang, Z. and Q. Zhang, Matrix tailoring of Engineered Binderitious Composites (ECC) with non-oil-coated, low tensile strength PVA fiber. Construction and Building Materials, 2018. 161: p. 420-431.

Zheng, L., W. Wang, and X. Gao, Solidification and immobilization of MSWI fly ash through aluminate geopolymerization: Based on partial charge model analysis. Waste management, 2016. 58: p. 270-279.

Zheng, L., W. Wang, and Y. Shi, The effects of alkaline dosage and Si/Al ratio on the immobilization of heavy metals in municipal solid waste incineration fly ash-based geopolymer. Chemosphere, 2010. 79(6): p. 665-671.

CHAPTER 9: CONCLUDING DISCUSSION

This dissertation explores several methods for creating sustainable, lightweight structures using locally available materials. A key contribution of this research was to identify the behavior of aerated slurry-infiltrated chicken mesh. The tensile behavior of aerated slurry-infiltrated chicken mesh relies upon the support provided by chicken mesh against realignment of the chicken mesh wires. This interaction depends on the quality (bearing capacity, elastic modulus and compressive strength) of the aerated slurry, and the concentration of chicken mesh as well as the specific surface area and the spacing of chicken mesh wires. Slurry-infiltrated chicken mesh sheets exhibit a ductile behavior in tension. The transition from normal-density (non-aerated) slurry to aerated slurries of lower densities produces some drop in peak tensile load, but not in their ductile tensile load-deflection behavior. The aerated slurry-infiltrated chicken mesh frame exhibited a ductile failure mode with a stable hysteretic behavior that provided significant energy absorption capacity.

This work also evaluated the energy efficiency of buildings constructed with aerated slurry-infiltrated mesh and biomass-based insulation. The desired seismic performance of the aerated slurry-infiltrated chicken mesh frame can be attributed to the high specific surface area of chicken mesh and its desired mechanical interlocking within the cementitious matrix. Treatment of wood chips/particles and shredded straw with aerated slurry effectively mitigates fungal growth in diverse moisture and fungal growth conditions.

Together, these studies of slurry-infiltrated mesh and biomass-based insulation offer important lessons for the construction of lightweight, energy-efficient structures that utilize local

materials. Such buildings can be constructed locally with readily available materials, which reduces costs. Local laborers can also be trained to safely implement the mechanochemical process for creating the slurry, which makes this construction approach affordable and feasible for both residential and business purposes in a variety of locations.